UNIVERSITA' DEGLI STUDI DI NAPOLI

"FEDERICO II"

FACOLTÀ DI SCIENZE MATEMATICHE, FISICHE E NATURALI

Ph.D. IN CHEMICAL SCIENCES

XXIV CICLO

Anna Balsamo

STRUCTURE AND FUNCTION OF TETRAMERIC HEMOGLOBINS AND THEIR MUTANTS AT A MOLECULAR AND CELLULAR LEVEL

TUTORS

PROF. LELIO MAZZARELLA

DR. ALESSANDRO VERGARA

SUPERVISOR

PROF. POMPEA DEL VECCHIO

COORDINATOR of the Ph.D. School (XXIV CICLO)
Prof. Lucio Previtera

Contents

ABSTRACT

The present Ph.D. thesis has focused on tetrameric hemoglobins (Hbs), both recombinant and natural, both from human origin and Antarctic fish, using a multidisciplinary approach based on spectroscopic, crystallographic and computational techniques. In particular the main scope of the research has been the elucidation of two still unsolved problems in the chemistry of tetrameric Hbs: **1)** the role of the bis-histidyl heme coordination in the Hb function and oxidation process and **2)** the role of the tertiary and quaternary structure in the modulation of the Root effect (namely drop of oxygen affinity with loss of cooperativity at low physiological pH). The first topic has been mainly approached through a comparative experimental (spectroscopic and crystallographic) / computational study of the β-subunits of human hemoglobin (β-HbA) and of the recombinant β-subunits Hb from Antarctic fish *Trematomus bernacchii* (β-HbTb), whose heterotetramer, in the ferric state, forms a mixture of aquo-met at the α-subunits and bis-histidyl adduct at the β-subunits. Similarly to the human β-chains, β-HbTb self-assembles to form the homotetramer (β_4-HbTb); however, the latter quantitatively forms reversible ferric and ferrous bis-histidyl adducts, which are only partially present in the human tetramer (β_4-HbA). The molecular dynamics study of the isolated β-subunit of the two Hbs indicates that the ability to form hemichrome is an intrinsic feature of the chain; moreover, the greater propensity of β-HbTb to form the bis-histidyl adduct is probably linked to the higher flexibility of the CD loop region. These findings are in perfect agreement with the X-ray structure of β_4-HbA in the ferric (solved in this thesis) that hosts only aquo-met coordination. The mechanism of hemichrome formation was also investigated by determining the x-ray crystal structure of the fully oxidized Hb from Antarctic fish *Trematomus newnesi* and by performing a Resonance Raman microscopy study on the Hb crystals from a sub-Antarctic fish (*Eleginops maclovinus*). The second topic has been investigated through a combined spectroscopic (resonance Raman (RR) /Vis microspectroscopy) and X-ray crystallographic study of oxygen (O_2) and nitric oxide (NO) binding to the T-state HbTb (Root-effect Hb) crystals at two different pHs, 6.0 and 8.4. The choice of these pH values is justified by the known tertiary structural differences of their X-ray structure in deoxygenated forms at different pH values. Oxygen binding curves have shown that the low -to- high pH transition induces 2-3 fold increase in oxygen affinity and that about half of the cooperativity present in solution is retained in the crystal. The simultaneous X-ray data collection, on the T-state nitrosyl-HbTb crystals assisted by online Raman acquisition, at the synchrotron Swiss Light Source (PXII beamline), clearly indicates an X-ray induced NO-photodissociation, providing a general physical explanation of the low content of nitrosyl-hemoglobin structures deposited in the Protein Data Bank. RR microscopy supported crystallography in choosing the X-ray dose feasible to collect a fully nitrosylated hemoglobin. The comparison between fully NO ligated and photolized crystal refined structures provides an elegant evidence of

heme-heme communication mediated *via* the CDα region, that involves those interactions that were suggested to be contributor to the Root effect in HbTb.
In addition this Ph.D. thesis also focused on a study at **cellular** level (*via* Raman imaging and Optical Tweezers) of healthy and C / S anemic erythrocytes [containing HbS (β6Glu → Val) and HbC (β6Glu → Lys)]. The different photo-sensibility and rigidity of healthy, C and S erythrocytes showed that the Raman micro-spectroscopy analysis combined with the use of Optical Tweezers offers enormous potential in the diagnosis of normal and diseased cells.

The structure of the thesis can be summarized as follow:
Chapter 1 introduces the topics analyzed in this Ph.D. work and describes the current state of the art.
Chapter 2 reports a brief explanation of the techniques adopted during this thesis work. Each dissertation about the theory behind the methods adopted is followed by the experimental conditions and procedures that have been utilized.
Chapter 3 describes the results of a) a comparative structural, spectroscopic and computational study of β-chain from HbA and of recombinant β-chain from HbTb and of b) a combined resonance Raman (RR) microRaman / X-ray crystallography study of ferric Hb of *Eleginops maclovinus* and *Trematomus newnesi*.
Chapter 4 reports the results of a combined spectroscopic (resonance Raman (RR) /Vis microspectroscopy) and X-ray crystallographic study of oxygen (O_2), carbon monoxide (CO) and nitric oxide (NO) binding to the T-state HbTb (Root-effect Hb) crystals at two different pHs, 6.0 and 8.4
Chapter 5 describes the theory, the experimental setup of Raman imaging and Optical Tweezers and reports the results of the characterization of healthy and C / S anemic human erythrocytes.
Chapter 6 contains the conclusions based on the performed experiments.
Finally, the thesis includes an Appendix and the list of the publications related to the work here described.

Chapter 1

Introduction

The correlation between protein structure and function is among the most important problems in biochemistry. Of special interest in this respect are the proteins that, on the one hand, are widely spread in living nature and, on the other hand, display a great diversity in their structural organization and functions in living organisms. One of the protein groups matching this definition to a full degree is hemoglobin (Hb). Traditionally Hb is defined as the respiratory protein which reversibly binds oxygen in the lungs and delivers it to the tissues. Hb has been termed the "honorary enzyme", since the detailed knowledge of its structure and functions has rendered it a valuable model for studying allosteric interactions in other proteins [1]. Functional and structural homologues of Hb are found in many species of vertebrates and invertebrates. Recently the definition of Hb has been expanded to include other functions and the number of Hbs identified has increased rapidly. Over 600 primary structures of Hbs have been determined and Hbs have been reported for organisms of all kingdoms [2].
All Hbs share a common tertiary structure, known as the "globin fold".
They exist as monomers, dimers, tetramers or even higher molecular weight assemblies. Our understanding of variations of this fold, as well as the broad diversity of function and widespread nature, has been increasing in recent years with the discovery of truncated hemoglobins [3], hexacoordinate hemoglobins [4], and even the discovery of two new human hemoglobins, neuroglobin and cytoglobin [5, 6].

1.1 Tetrameric hemoglobins

Tetrameric hemoglobins of the higher vertebrates are intracellular protein found in millimolar concentrations within erythrocytes [7]. Tetramers are composed of identical heterodimers, each containing an α-chain and β-chain. Each chain consists of seven or eight helices, conventionally labeled A–H (in according to a notation by Watson and Kendrew of 1961), linked by non-helical segments (termed as AB, BC etc.), and of N-terminal and C-terminal extensions referred to NA and HC. Residues within each segment are numbered from the amino end (A1, A2, and so on). The four chains are arranged tetrahedrally around a two-fold symmetry axis that runs along a water-filled cavity, creating a roughly spherical molecule 6.4 x 5.5 x 5.0 nm.

Each of the four subunits form a cavity, between the E and F helices, that contains the heme group. The heme of Hb, known as protoporphyrin IX, is a prosthetic group that consists of four pyrrole rings linked by methene bridges to form a tetrapyrrole ring, and a central iron atom (Fe^{2+}), bound to the four pyrrole-nitrogen atoms.
Protoporphyrin IX has two vinyl groups, four methyl groups and two propionate groups. The main helices within the globin fold are organised into a two layer structure recognised as a "three-over-three" α-helical sandwich.
Evolution has conserved this fold of the chain despite great divergence of the sequence: the only residues common to all hemoglobins are the HisF8, that anchors the heme to the protein moiety at the proximal side of the heme (thus known as the proximal His) and PheCD1, that wedges the heme into its pocket. On the distal side of the heme, where in the normal ferrous state this site can reversibly bind oxygen (its primary role), in most, but not in all hemoglobins, a histidine, HisE7, is highly conserved (Figure 1.1)

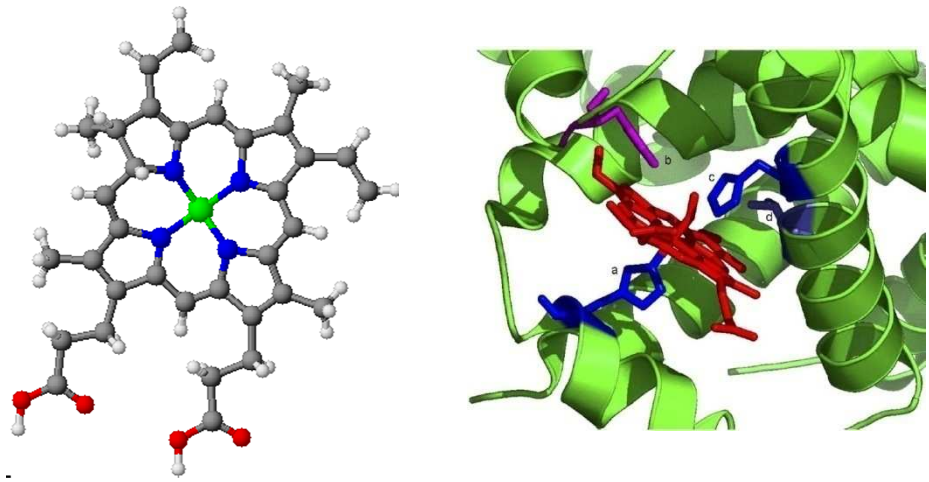

A **B**

Figure 1.1: A) Protoporphyrin IX; **B)** The major structural elements of the α globin heme binding site are shown. (a) HisF8 (blue), (b) PheCD1 (cyan), (c) HisE7 (blue), (d) ValE11 (dark grey), O_2 (red)[8].

The hemoglobin can be in a deoxygenated state [9]. In this state, the iron ion is high-spin ferrous (HS) five-coordinated (5c) and out of the porphyrin plane toward the proximal side, with a square base pyramidal geometry: the four pyrrole nitrogen atoms form the basis while the fifth coordination site is the N^{ε} atom belonging imidazole ring of HisF8. Upon oxygenation, the iron becomes low-spin ferrous (LS) six-coordinated (6c). O_2 binds Fe^{2+} at the sixth coordination site (distal side) by dragging the iron ion towards the porphyrin plane and in turn transmitting this movement to the other subunits through interactions αβ [10].

Oxygen binding to hemoglobin exhibits a cooperative behavior. The first important observation of the Hb allostery is attributed to C. Bohr who reported in 1903 that its oxygen-binding process was sigmoidal or cooperative [11]. In other words, the binding of ligand at one subunit of the hemoglobin molecule activates the binding of subsequent molecules of oxygen at other subunits within the hemoglobin molecule. It is this activation process which then confers the sigmoidal, cooperative oxygen binding curve on hemoglobin and is known as the "homotropic effect" [8].
Cooperativity is quantitatively expressed by the Hill equation [12]:

$$\log\left(\frac{Y}{1-Y}\right) = n\log\left(\frac{pO_2}{p_{50}}\right)$$

where pO_2 is the partial pressure of oxygen, p_{50} is the oxygen concentration necessary to achieve half saturation of the heme sites (as such is related to the equilibrium constant for the overall four step process) and Y is the fractional oxygen saturation.
The slope of the central portion of the curve is referred to as the "Hill coefficient", n50, an index of the cooperativity (sigmoidicity) of the hemoglobin oxygen-binding curve and a measure of the interaction between the subunits of the protein. This coefficient varies from a value of 1 when the subunits do not interact up to a value of 4 if the subunit interaction is infinite. In human hemoglobin, under physiological conditions, n50 is typically close to 2.8.
The specific mechanism whereby inter-subunit interactions lead to a sigmoidal oxygen binding curve has long been the subject of scientific debate. The pioneering crystallographic studies by Perutz and his co-workers have shown that in the fully oxygenated and the fully deoxygenated states, Hb assumes two distinct quaternary structures, R and T, respectively, characterized by the absence and presence of salt bridges, and by a different pattern of $\alpha_1\beta_2$ and $\alpha_2\beta_1$ interactions [13, 14]. Binding of ligands triggers a series of tertiary conformational changes that break salt bridges, destabilizing the T state and leading to the liganded R state [15].
In particular the quaternary R→T transition consists in a rotation and a traslation of the $\alpha_1\beta_1$ dimer relative to the $\alpha_2\beta_2$ dimer by 12-15° and ~1 Å, respectively (Figure 1.2)[13].

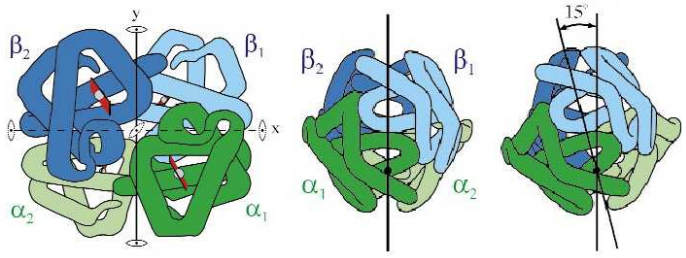

Figure 1.2 Schematic structure of hemoglobin (low resolution)showing the difference in quaternary structures (image from [16]).

According to his mechanism, oxygen binding to the T conformation moves the iron from a position out of the porphyrin plane to one that is more co-planar.
The T state has low affinity for O_2 but high affinity for protons, chloride, organic phosphate and CO_2. In the R state these relative affinities are reversed. This allosteric factors stabilise the T state by forming salt bridges between subunits. These salt bridges are absent in the R state [17].
The assumption that Hb exists as two end states without any intermediate states has been challenged over the years. Several studies have now shown that the allosteric transition between the tense and relaxed states is mediated by multiliganded Hb states, with each form exhibiting variable oxygen affinities [18-23]. This observation has been correlated with conformational variations of the liganded states, which were found to be dependent on changes in allosteric effectors [18, 19]. The functional observations that liganded Hb exists as multiple states each with a distinct conformation seems to be consistent with the recent discoveries of several liganded Hb structures with different relaxed conformations, including the R2, RR2 and R3 states [24-28].

1.2 Antarctic fish hemoglobins

The important role of Hb in carrying oxygen to tissues is probably the origin of its adaptation to different environmental conditions [29]. Much of our knowledge of the effect of the environment on vertebrate physiology and evolution has arisen from the study of fishes, which share most physiological mechanisms with humans [30]. The aquatic habitats, indeed, are such that fish may experience temporal and spatial variations in oxygen availability, salinity, ionic composition, pH and temperature. Fish Hbs evolved structural and functional diversity to adapt and modify their features under all types of selective pressure, but both the predominantly helical structure and a large number of amino-acid residues are well conserved. In this context the study of Antarctic fish Hbs (AfHbs) is particularly interesting. The Antarctica extends for 14˙000˙000 Kmq and for about 98% is covered by ice; the Antarctic seas are characterized by particularly low and constant temperatures (-1.6°C to -2.1°C) and high oxygen contents of more than 95% saturation, from 1.3 mM at 25 °C to 2.3 mM at -1.9 °C (NIST source). Only one group of teleost fish, the suborder *Notothenioidei*, succeeded in adapting to this challenging environmental conditions. This suborder includes 8 families: five Antarctic families (*Nototheniidae, Batidraconidae, Artedidraconidae, Arpagiferidae and Cannictidae*) and three non-Antarctic (*Bovictidae, Pseudafriditae and Eleginopidae).*
In the evolutionary process of cold adaptation Antarctic fish has produced unique hematological characteristics in comparison with temperate and tropical species [31-34]. The blood of Antarctic fish contains antifreeze glycoproteins (AfGPs), a family of discretely sized polymers composed of a simple glycotripeptide monomeric repeat, which lower the freezing point of their blood by a non colligative mechanism to -2.2°C to -2.7°C, depending on the species [35-37]. Furthermore, their blood contains

fewer erythrocytes and less Hb. This decrease in erythrocyte number and Hb content counteracts the increase in viscosity that would otherwise occur with decreased temperature. the oxygen affinity of the Hbs of many Antarctic species is quite low, as indicated by the values of p50 [31-34]. This feature is probably linked to the high concentration of oxygen in the cold Antarctic waters and hence to water temperature. At the same time low temperatures reduced the overall metabolic demand for oxygen, while increasing its solubility in the plasma, so that more oxygen can be carried in physical solution, and less needs to be bound to Hb [38]. Multiplicity of Hbs in fish is usually linked to the need to respond to variable environmental conditions specifically associated with a given habitat [39, 40]. Instead as constancy characterizes the conditions of the Antarctic marine environment, the blood of these fish is endowed with a markedly reduced Hb multiplicity.
Most of the species of the family *Nototheniidae* have a single major Hb (Hb 1), accompanied by the minor or "embryonic" components Hb C (in traces) and Hb 2 (approx. 5% of the total), both having one of the globins in common with Hb 1 [41].
AfHbs, although structurally and functionally analogous to mammalian Hbs, display two peculiar properties:

- the Root effect (as found in other fish Hbs), namely low oxygen affinity with loss of cooperativity at low physiological pH, in the ferrous state [8, 42];
- formation of hexacoordinated bis-histidyl adducts (hemichromes), upon oxidation, in the ferric state [43-45].

1.3 Root effect

The pH is certainly one of the most effective modulators of protein function, studies aimed at unveiling the relationship between the protonation state of specific residues and local or global protein structure may provide valuable information [46-49]. The dependence of Hb affinity and cooperativity on the pH has been discovered nearly a century ago. In particular the reduced oxygen affinity of mammalian Hbs at acidic pH, known as Bohr effect, represents a fundamental property of this protein that allows an efficient transport of the oxygen from the lung to the tissues. The simplest expression of this effect can be written as:

$$[\text{Hb-H } n_{H+}]^{nH+} + O_2 \leftrightarrows \text{Hb-}O_2 + n_{H+}H^+$$

in which the protons released as a consequence of oxygen binding are known as the "Bohr protons". For human hemoglobin approximately 2 Bohr protons are released at physiological pH during oxygenation.
Several Hbs from teleost fishes, besides having affinity for O_2 highly sensitive to pH, also become non cooperative at acidic pH. The complete loss of cooperativity (indicated by a Hill coefficient equal to one), thus the inability to saturate the ligand sites at low pH even at high oxygen pressure, is a distinctive property with respect to the Bohr effect, and is referred to as the "Root effect", first described in 1931 [16, 50]. The Root effect is responsible for a physiologically important response to lactic

acidosis, which may induce complete oxygen unloading. The physiological significance of Root-effect Hbs has been linked to the presence, in the fishes, of at least one of the two anatomical structures which require high oxygen pressure:
-the *rete mirabile*, which supplies the gland that inflates with oxygen the swimbladder, a structure consisting of a gas containing sac within the fish, which is variously inflated and deflated to alter the natural buoyancy of the fish and to optimize energy use during swimming at various depths [51];
- the *choroid rete*, a vascular structure which supplies oxygen to the poorly vascularized retina [51].
Antarctic fish lack the swimbladder, and it is worth mentioning that only the few species possessing Hbs without a Root effect, as well as those of the family Channichthyidae, whose blood lacks Hb, are devoid of the *choroid rete* [52].

1.3.1 The structural interpretation of the Root effect

Despite more than three decades of studies, it is yet virtually impossible to ascribe the presence or absence of the Root effect to substitutions of a few amino-acid residues, or to a single explanation [46, 53, 54]. Indeed, the situation is highly complex, and is probably linked to the combination and interplay of a number of factors in the architecture of the globin tetramer. In order to clarify the molecular origins of the Root effect it will be important to integrate structural information, through high-resolution crystallographic structures at high and low pH values [46, 54-58], with functional studies of site-directed mutants [59, 60] and with molecular dynamic approaches, on the subunits [61] and on the tetramers [62].
Thermodynamics of oxygen binding and its pH dependence are based on the Wyman function, and the plot of log (p50) *vs* pH provides an estimate of the number of protons (n_{H+}) released per tetramer upon oxygenation, according to the following equation [63, 64]:

$$n_{H^+} \cong -4 \frac{\partial \log(p_{50})}{\partial pH}$$

where n_{H+} provides a quantitative measurement of the Root effect and usually falls in the range between 8 and 2 protons per tetramer. It has also been used to quantify the Bohr effect. There is a clear correlation between n_{H+} and the strength of Root effect, and it appears that an n_{H+} increase of one proton roughly corresponds to an increase of 10% [65].
The easiest thermodynamic approach to interpret the Bohr and Root effect is the concerted Monod–Wyman–Changeux (MWC) two-state allosteric model [1]. This approach has often been extended to include a distinct association constant for the α (K_α) and β (K_β) chains, defined by a heterogeneity factor (K_α/K_β) [66]. According to this classic models, the drastic drop in cooperativity at low pH values, typical of the Root effect, may have three mechanisms:

(a) drastic overstabilisation of the T state (or destabilisation of the R state), that shifts the allosteric constant upwards, L; both enthalpic changes [55, 57] and entropic order-disorder effects [58] can account for such a pH-modulation.

(b) at fixed L, strong heterogeneity in the oxygen association constants of the α and β chains, that produces a heterogeneity factor significantly different from one;

(c) combination of (a) and (b).

It should be stressed that in Hbs with a Hill coefficient lower than one the introduction of a heterogeneity factor in the interpretation is mandatory.

According to (a), a structural model must satisfy two major requirements: (i) the number of protons released upon oxygenation must correspond to nH^+; (ii)the upload of these protons must account for the increase of the allosteric constant.

In contrast, according to (b), a structural analysis must identify the location of protons that affect the heterogeneity factor involving the ligand association constants of the α- and β-chains. Ultimately, both approaches require identification of the residues whose pKa values are expected to shift upon oxygenation, which would affect the allosteric constant and/or the heterogeneity factor.

In recent years, X-ray crystallography succeeded in overtaking one of the classical views which attempts to correlate all major changes in Hb function with a few residue substitutions. The extensive structural analysis of the Root effect by X-ray crystallography of Antarctic fish Hbs was stimulated by the good capacity to crystallise, together with the high sequence identity. So far, the crystallographic studies of fish Hbs refer to three temperate [trout, [54] tuna [46] and *Leiostomus xanthurus* [56] and two Antarctic species (*Trematomus newnesi* [55] and *Trematomus bernacchii* [57]).

A good interpretation of the Root effect of a given Hb would require the knowledge of the T and R states, each at acidic and alkaline pH (tetrad of four structures -the "holy grail"-) [8]. Considering that the R structure at acidic pH is virtually a *contradictio in terminis* for a Root effect Hb, the remaining triad has been achieved for both temperate tuna [46] and Antarctic *T. bernacchii* (HbTb) Root-effect Hbs [57].

Although the physiology and the structural basis of the Root effect have been addressed in a large number of studies [8, 42, 46, 59, 65, 67, 68], it remains a mystery in many aspects. Over the years, several hypotheses on the structural determinants of the Root effect have been suggested. A variety of possible mechanisms involving the replacement of Cys93β (F9) in HbA by Ser [69] in Root effect Hbs, the formation of a strong hydrogen bond between the side chains of aspartic residues in the deoxy T state [63], and the presence of a cluster of charged residues located at the $\beta_1\beta_2$ interface of the liganded R state [56], have been proposed.

The current theory is based on overstabilisation of the T state at acidic pH, accompanied by some structural evidence on the possible source of heterogeneity between the α and β chains in fish Hbs.

The crystal structure of the cathodic Hb of *T. newnesi* (HbCTn) in the T state has been a valuable case of study, since it refers to a Hb with very low His content [70]. The structure of the deoxy form of HbCTn indicates that none of the histidyl residues of

this Hb is involved in binding a proton that could be released upon oxygenation [71]. Indeed, the only protons trapped in the T state are those at the $\alpha_1\beta_2$ ($\alpha_2\beta_1$); interface stabilised by the hydrogen bond between Asp95α and Asp101β. This unusual interaction, first noticed in the deoxy form of HbTb [63], is disrupted upon oxygenation and contributes two Root protons per tetramer.

For HbCTn, this motif is sufficient to justify the strength of the Root effect ($nH^+ = 2$) and has been suggested to represent a minimal structural determinant for such effect. Indeed, the aspartyl triad (Asp95α, Asp 101β and Asp99β) is present in the primary structure of all fish Hbs, but not in mammalian Hbs, as for human hemoglobin (HbA), where Asp101β is replaced by Glu.

This structural motif *per se* is sufficient to generate the Root effect, and it can be considered as the minimal structural requirement needed for designing Root effect Hbs. Indeed, the Asp-Asp interaction has been found in the deoxy structure of HbTb and tuna Hb, but not in the deoxy form of the non-Root-effect HbI from trout, where the interaction between the two aspartyl residues is mediated by a water molecule [54] and in the deoxy form of HbA (probably due to the substitution of residue Asp101β by Glu).

However the recent crystal structure, non-Root-effect Hb, of the principal Hb component isolated from the Antarctic fish *T. newnesi*, in deoxygenated state (deoxyHbITn), showing the presence of the inter-Asp H-bond at $\alpha_1\beta_2$ interface, has undermined this paradigm or, at least, consider this system an exception [58].

The remaining Root protons of tuna Hb and HbTb have been associated to the histidyl residues involved in salt bridges in the T state and disrupted in the R state [55], highlighting a role for His in helix E of the β chain and in the CD region of the α chain (Figure 1.8) [46, 57]. Both Hbs are solved at two different pH values, 5.0 and 7.5 [46], and 6.2 and 8.4 [57], respectively. In particular the crystal structure of tuna Hb at pH 5.0, which displays a Hill coefficient lower than one, revealed a strong effect of structural heterogeneity between α and β-chains: the distal His swings out of the heme pocket in one of the two α chains, but stays in the standard internal position in the β chains [46]. In crystal structure of T-state HbTb, at acidic pH, a stabilizing interaction occurs between the side chains of His55α and Trp46α, at the CDα corner (the switch region in the allosteric transition of mammalian Hbs [13, 72]. Specifically, a parallel orientation of the two aromatic side chains (π-stacking) is observed (Figure 1.8). At pH 8.4 the deprotonation of His55α causes the break of the salt bridge with Asp48α and the re-orientation of the imidazole ring which loses the π-stacking interaction with Trp46α, leading to a more stable T-shaped configuration of the two aromatic rings [73](Figure 1.3).

Further evidence of heterogeneity has been reported for the ferric form and of AfHbs.

The recent observation of i) a third R/T intermediate quaternary structure of ferric [44, 45] and partially ferrous Hbs [74, 75] and ii) the tertiary-structure pH-induced changes within a well conserved quaternary structure (as first described), suggest that,

for a complete description of the structural determinants of the Root effect and to fully understand its molecular bases, a more complex interpretative model is needed , inclusive either i) a quaternary three-state model [76] or ii) a global allostery model [20].

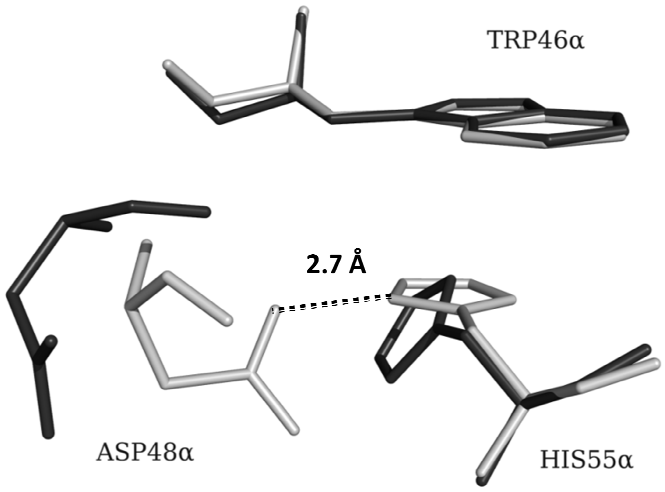

Figure 1.3: Models of residues Asp48α, His55α and Trp46α of the Root-effect Hb from *T. bernacchii* in T state, at pH 6.2 (black) and pH 8.4 (grey), re-oriented to afford the best superimposition of the CDα region of the two models.

In the present Ph.D. research activity, O_2, CO and NO binding to Root effect Hbs have been investigated using their structural and spectroscopic/microspectroscopic features.

1.4 Exogenous ligands of hemoglobin

The gaseous molecules CO, NO and O_2 bind avidly to heme, in the ferrous state, thanks to effective backdonation of Fe(II) dπ electrons to their π* orbitals. Nature has harnessed this property to regulate essential biochemical processes in response to the presence of these molecules [77].

The binding of these diatomic ligands to heme has been studied in biochemistry for over hundred years [78].

Investigations of the reactions of these ligands with heme proteins have shown that NO has very high affinity for heme of 100,000-fold greater than that of oxygen and 1,000-fold greater than that of CO, [79, 80]. The second-order rate combination rate constant (k_{on}) of ~ 10^7 $M^{-1}s^{-1}$ is very similar for CO, NO, and O_2 and the process is essentially diffusion-controlled (Figure 1.4). The much higher affinity of NO is due to

differences in the rate of ligand dissociation (k_{off}) which is of the order of ~ 15 s^{-1} for O_2, 0.01 s^{-1} for CO and ~ 0.00002 s^{-1} for NO, exhibiting the slowest dissociation rate of any heme ligand this far characterized. The rate of NO dissociation from $Hb(NO)_4$ increases at the reaction progresses, indicating that partially nytrosilated, T state, has a lower NO affinity than fully liganded, R state, Hb [80].

Compound	O_2 on rate (M^{-1} s^{-1})	O_2 off rate (s^{-1})	O_2 dissociation constant (M)	NO on rate (M^{-1} s^{-1})	NO off rate (s^{-1})	NO dissociation constant (M)	CO on rate (M^{-1} s^{-1})	CO off rate (M^{-1} s^{-1})	CO dissociation constant (M)
Haemoglobin (R-state)	5×10^{7}	15	3×10^{-7}	2×10^{7}	1.8×10^{-5}	0.9×10^{-12}	6.0×10^{6}	0.01	1.7×10^{-9}
Haemoglobin (T-state)	4.5×10^{6}	1900	4.2×10^{-4}	2×10^{7}	3×10^{-3}	1.5×10^{-10}	8.3×10^{4}	0.09	1.1×10^{-6}

Figure 1.4: Comparison of the kinetic and thermodynamic constants for O_2, NO and CO binding the ferrous iron in model systems [79, 80].

The oxygen binding with respect to carbon monoxide is much favored in hemoglobin and myoglobin: it is well establish from model studies that the preference for binding of CO over O_2 of simple porphyrin systems was 25 000, while in myoglobin it was only about 25 [81]. Possible mechanisms of the discrimination between NO, CO and O_2, favoring O_2, moreover of vital importance, in myoglobin [82-84] and in hemoglobin [85], seem to be hydrogen bonding and electrostatic interactions.

1.4.1 Structure and function of tetrameric nitrosyl-hemoglobin

Nitric oxide (NO) is a signaling molecule involved in a large number of important physiological and pathophysiological processes [86] (Figure 1.5). NO is produced endogenously by the metabolism of L-arginin, catalyzed by the enzyme NO-synthase isoforms (with heme as a co-enzyme)[87].

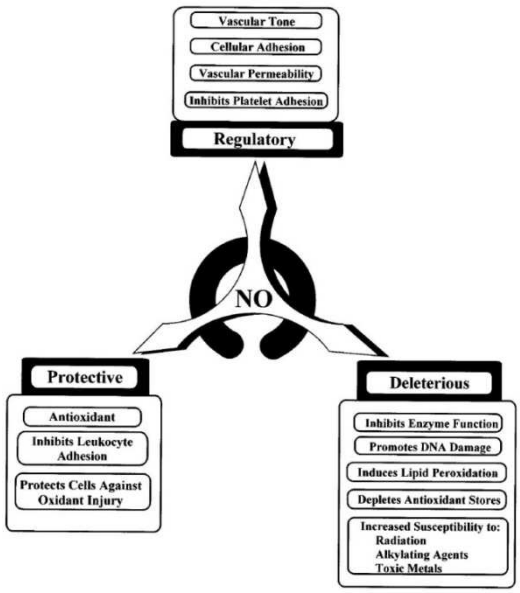

Figure 1.5: Some of processes in which nitric oxide is involved.

The discovery, in the late 80s, that NO is the elusive endothelium-derived relaxing factor (EDRF) that binds to the hemoproteins guanylate cyclase and stimulates the dilation of blood vessels [88] posed some immediate questions about the dependence of the regulation of blood flow by nitric oxide, particularly in light of the fact that hemoglobin is present in high concentrations (~ 2.5 mM) in erythrocytes and has higher affinity for NO than for other heme ligands [89].
NO entering the blood is subject to rapid inactivation *via* its reactions with oxyHb to form methemoglobin (metHb) and nitrate [90]:

$$\left[Hb^{II}-O_2\right]+NO\longrightarrow\left[Hb^{III}-ONOO^-\right]\longrightarrow Hb^{III}+NO_3^- \quad (1)$$

and *via* its tight binding to deoxy-Hb to form nitrosylhemoglobin (HbNO) by nitrite reductase activity (equation 3).

$$Hb^{II}+NO_2^-+H^+\longrightarrow Hb^{III}+NO+OH^- \quad (2)$$

$$Hb^{II}+NO\longrightarrow\left[Hb^{II}-NO\right] \quad (3)$$

This latter reaction, first fully characterized by Brooks in 1937 [91] and by Doyle et al. in 1981 [92], recently has attracted particular interest, because may supply a mechanism in which Hb is involved in vasodilatation (Figure 1.6) [93, 94].

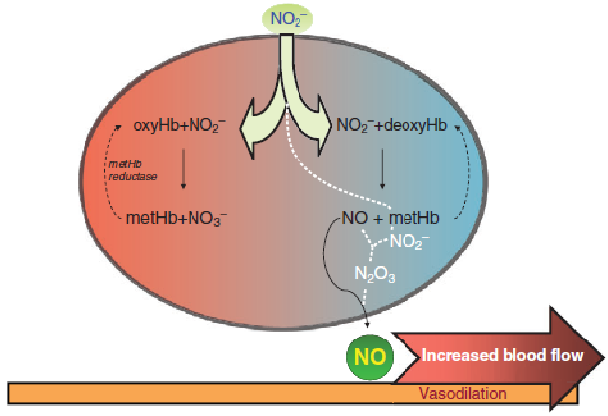

Figure 1.6: Red blood cell (RBC) generation of NO by deoxyHb-mediated nitrite reduction. Nitrite entering RBCs reacts with both oxyHb (forming nitrate and metHb) and deoxyHb (forming NO and metHb), but the last reaction is favored at low O_2 saturations. The produced NO binds to deoxygenated heme groups, forming HbNO (or reacts with oxyHb, forming metHb and nitrate), but some NO may escape the RBCs and induce vasodilation [95].

The study of the physiological consequences of the interaction between NO and Hb also meets many complications because of technical difficulties associated with accurate detection of the low levels of nitric oxide and its derivatives, both *in vivo* and *in vitro*. In addition, the chemistry of NO is very complex because of the multiple possible oxidation states available to nitrogen in NOx.

Reactivity of NO with Hbs is at the heme as well as heme at cysteine residues. In 1996, it was discovered that a small fraction of Hb in the blood carries NO bound to the thiol groups of CysF9β (Cys93β) as S-nitroso adduct (SNO-Hb). Since reactivity of CysF9β in human Hb is controlled by the quaternary state of the protein, it was proposed that the nitrosylated form of this residue is sensitive to the O_2-linked allosteric changes of Hb. Indeed, SNO-Hb concentration was originally found to be lower in venous than in arterial blood, suggesting that SNO-Hb in mammals may release NO when the O_2 tension decreases, thus increasing vasodilation and blood flow when tissues become hypoxic [96]. The functional relevance of Cys F9β is supported by the fact that this residue is highly conserved in mammals and birds [97]. It has, however, also been noted that this particular cysteine is absent in fish Hb, which would preclude a similar function in fish [98]. It does, however, not exclude the finding of SNO groups in these Hbs, as reactive cysteines may be present at other positions in the Hb.

Both crystal structure of S-nitrosylated at Cys93β [99] and NO bound at the heme [100] are available for human hemoglobin. The crystal structure of human nitrosyl-hemoglobin, in the T state, shows a different coordination at the α and β subunits. The nitrosylation of the heme groups breaks the Fe-N^{ε}-His87(F8) α bond (distance

Fe-N$^{\varepsilon}$(His87) becomes ~ 4 Å) but not the Fe-N$^{\varepsilon}$-His92(F8)β bond (Figure 1.7). Consequently, in HbA the α-heme groups are five-coordinate while, the β-heme groups are in a canonical six-coordinate.

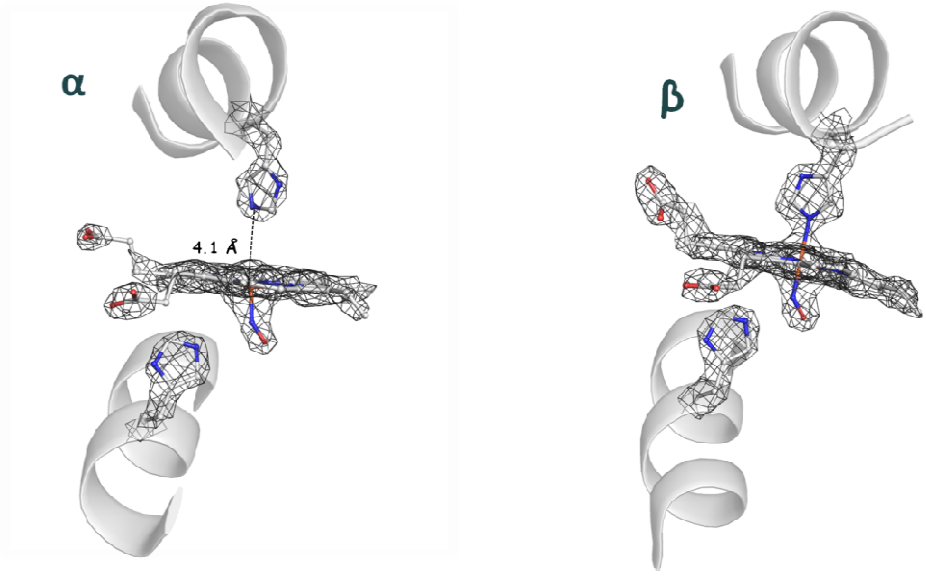

Figure 1.7: Fo - Fc electron density maps of heme groups for the (*left*) α-subunit, (*right*) and β-subunit of quaternary-T state human nitrosyl-hemoglobin (PDB code: 1RPS [100]).

The mixture of penta- and hexa-coordinate forms in the T state NO-human hemoglobin is also been detected spectroscopically by electron spin resonance [101, 102], infrared [103] and resonance Raman ([101, 104] studies. Perutz has attributed breakage to a combination of the tension exerted by the movement of the iron and an NO trans influence which weakens the Fe-N$^{\varepsilon}$(HisF8) bond. A similar rupture of the α Fe-proximal histidine bond, is also been observed in the crystal structure of the fully liganded T-state cyanide complex of human hemoglobin [105], but not observed when heme is bound with CO or O_2 [72, 103].
Despite the high physiological interest, the above structure of the T-state nitrosyl-HbA and of human Hb mutant (βW37E, PDB code: 1RQA) are the only crystal structure of NO-bound hemoglobins deposited in the Protein Data Bank (less than 1 % of the ligated Hbs crystal structures). Indeed, the study of such nitrosylated species is complicated by the high reactivity of heme-NO complexes that undergoes to a fast oxidative denitrosilation in aerobic conditions.

1.5 Oxidation of Hbs and bis-histidyl adducts

The reversible and stable binding of molecular oxygen to the heme iron(II) is the basis of hemoglobin function. Like all known dioxygen carriers *via* transition metals, the oxygenated forms of myoglobin (Mb) and Hbs (Hbs) are oxidized easily to their met

ferric forms, which cannot be re-oxygenated [106]. Although autoxidation is inevitable in nature for all oxygen-binding heme proteins, the met-Hb content of freshly drawn blood is usually maintained within 1–2% by virtue of a strongly reducing environment [107].
The product of heme oxidation is dependent on many factors including globin matrix, pH, temperature, oxygen pressure, denaturant agents.
In the Hb superfamily, and in particular in the vertebrate $\alpha_2\beta_2$ tetrameric Hbs, the ferric hexacoordinate (6c) aquo form, in equilibrium with the hydroxy form, is by far the most common one formed during the autoxidation process. However, a variety of ferric coordination states have also been detected and characterized, namely a pentacoordinate (5c) state and an endogenous hexacoordinate (6c) state or "hemichrome" (for the endogenous 6cLS, depending on the oxidation state of the iron, these forms are called hemichrome [Fe(III)] or hemochrome [Fe(II)]). Hemichromes are low-spin complexes, in heme proteins, where the sixth coordination of the heme iron (III) is occupied by an endogenous side chain of a residue distal. The relative amounts of these states are highly variable, thus suggesting that the functional roles of these oxidation states are multiple, possibly being a tool for modulating ligand binding or redox properties [108].
In general, in all ferric Hbs, the 5c state is quite rare. It has been detected in some myoglobin distal mutants [109, 110], the monomeric flavoHb [111], and the dimeric *Scapharca inaequivalvis* Hb [112]. More recently, the 5c species have been discovered in Hbs with higher structural complexity, such as tetrameric Hbs from polar fish [45, 67, 113] and giant Hbs [114]. As compared to the 5c state, the occurrence of hemichrome is more widespread at least among invertebrates, plants, and bacteria. The residue that can occupy the sixth axial coordination site under native conditions depends on the nature of the distal residues. Although in the majority of cases, the sixth ligand is a His (distal) residue, recently, in 2/2 bacterial Hbs [115-118] or in naturally occurring mutants of HbA [119], a Tyr has been found to be the sixth ligand.
In the present Ph.D. research activity only the bis-His (hemichrome) derivatives of tetrameric Hbs will be described, focusing on their structural and spectroscopic features, and their structural determinants *via* experimental and computational analysis.
The initial findings of hemichromes, in tetrameric Hbs, were strictly associated with a partial unfolding of the native structure [120]. Indeed, hemichrome formation, which is rather slow in human Hb, is accelerated by denaturing agents. Under denaturing conditions, the formation of the bis-His complex can be favored by the altered structure of the globin, which allows the binding of the distal His to the iron.
However, it was soon recognized that the hemichrome (and hemochrome) state was an accessible structural sub-state of the native-like Hb population. These states can be distinguished from those associated with denatured conditions by reversibility and the absence of precipitation and heme release [121, 122]. In tetrameric HbA in solution, the endogenous hexacoordination is favored when the chains are separated, suggesting

a possible role of the quaternary structure in the destabilization of the hemichrome species [121].
The fact that hemichromes are so common in nature suggest a conserved function and a putative physiological role of the in vivo formation of this form that remains to be elucidated. The hypothesis that reversible bis-histidyl complexes, such as hemichrome, could populate the landscape of native Hbs in solution is particularly attractive as it suggests a functional role of this form in tetrameric Hbs. The relevance of hemichrome spans from biomedical to physiological aspects [121], some of which have been reviewed recently [123]. Indeed, many hypotheses on the role of bis-histidyl coordination in organism physiology have been postulated. The bis-histidyl complex can be involved in ligand binding [124, 125], in facilitating the in vivo reduction of met-Hb [126], in Heinz body formation *via* copolymerization with the cytoplasmatic domain of band 3 [121] and in nitrogen monoxide scavenging [127]. Hemichrome detection has been suggested as a valuable tool for tumor diagnosis [128]; the reaction of acetylphenylhydrazine with erythrocytes leads to hemichrome formation in healthy people but not in breast-cancer patients. Recently, hemichrome in human HbC was observed to interact in vivo with erythrocytes, modifying their membrane rigidity [129] and affecting its ability to release oxygen.
Finally, it has also been suggested that hemichrome can be involved in the protection of the Hb molecule from peroxidation attack [130].

1.5.1 Structural features of bis-histidyl adducts

The oxidation of tetrameric Hbs in different species can lead, as mentioned above, to the formation of different products. The auto-oxidation rate in temperate fish Hbs is higher than in mammals [131], and in Antarctic fish Hbs it is even higher than in temperate fish [44]. Spectroscopic analysis revealed that AfHbs share a common oxidation pathway, which shows striking differences from the oxidation processes of hemoglobins from other vertebrates. The elucidation of the crystal structure of Hbs in a bis-histidyl state has provided an important guide for the interpretation of the spectroscopic features observed in solution. So far, only about a dozen Hb 3D structures with bis-histidyl endogenous coordination have been deposited in the PDB (see Table 1.1).
A first picture of a tetrameric Hb in partial hemichrome state (only in β chains) was obtained investigating air-oxidized crystals of HbITn, [43], then followed by the study on the HbTb [44, 45].

Table 1.1: Crystal structures of monomeric, dimeric and tetrameric Hbs in bis-His forms

Hemoprotein	PDB code	Res. (Å)	pH	Ref.
Tetrameric Hbs				
T. bernacchii (β chain)	2PEG	1.4	7.6	[45]
T. newnesi (HbITn β chain)	1LA6	2	7.6	[43]
Equus caballus (Hb α chain)	1NS6	2.1	5.4	[132]
H. sapiens [(AHSP)HbA α chain]	1Z8U	2.4	6.5	[130]
Dimeric globins				
Oryza sativa (Non symbiotic plant Hb)	1D8U	2.3	7.8	[133]
Homo sapiens cytoglobin	1URV	2	5	[125]
Monomeric globins				
Homo sapiens neuroglobin	1OJ6	1.9	6.5	[134]
Synechocystis s.	1RTX	1.8	6.5	[135]
Caudina arenicola	1HLB	2.5	6	[136]
Mus musculus neuroglobin	1Q1F	1.5	4.6	[137]
D. melanogaster	2BK9	1.2	10	[138]

The combination of these high-resolution crystallographic studies and spectroscopic techniques have shown that upon oxidation, under physiological conditions, mammalian and temperate fish Hbs are mostly converted into the aquo-met form, both at the α and β subunits, whereas AfHbs are converted into the hybrid α(aquo-met)/β(hemichrome) form (Figure 1.8).

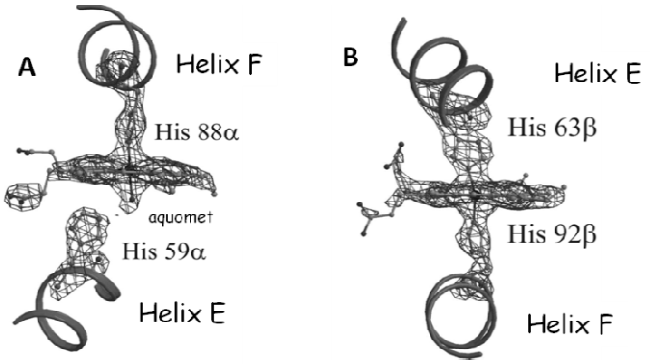

Figure 1.8: Electron density maps corresponding to the heme regions of HbTb oxidized with ferricyanide: (A) α-heme in the aquo-met form and (B) β-heme in the hemichrome form [44].

In HbTb and HbITn the reason for this endogenous coordination is related to the ability of the β chains to host a scissor-like motion of helices E and F accompanied by sliding of the β heme out of its pocket, toward the solvent [43-45]. This scissor-like movement is favoured by the replacement of Phe85β in mammalian Hbs with Tyr in most fish Hbs. The hydroxyl group of Tyr85β causes a kink in the facing helix E by forming two H-bonds [43] with the oxygen carbonyl atom of Gly70 and the N atom of Gly74, thus facilitating the movement of the distal His positioned almost at the other end of the same helix E (Figure 1.9).

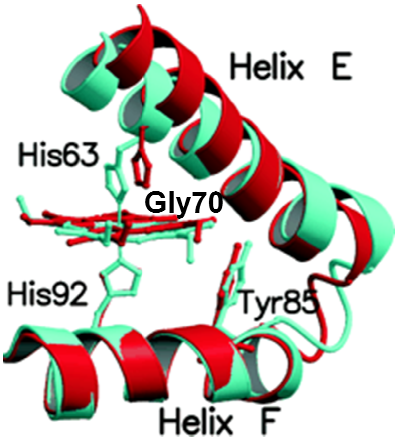

Figure 1.9: The scissors-like motion of the β chain EF corner occurring upon hemichrome formation. The EF regions of HbTn[α(CO)β(hemi)]$_2$ (cyan) and HbTnCO (red) are shown after superimposition of the F helix. For clarity the propionate groups of heme have been omitted [44].

This closure can be assessed by measuring the Cα- Cα distance between distal and proximal His that decreases from 14.5 Å, in the α and β chains of Hb from different organisms and in a variety of ligated states [74, 108, 123], to 11.5–12.5 Å in bis-histidyl hemes (Figure 1.9).
In addition, the sliding motion of the heme group, which is also important for the coordination of distal His to the iron, is facilitated by Gly70β in fish Hbs; in human HbA, the methyl group of Ala70β is positioned above the heme plane in a border cavity, in a way to hinder the sliding off of the heme.
In HbTb and HbITn, the structural data indicate that the scissoring-like motion of the EF pocket may initiate a cascade of events that favor the switch from the R to the T state. Indeed this closure movement propagates to other structural elements of the tertiary structure of the β subunit, directly involved in the quaternary assembly of the molecule. In particular, the FG corner assumes a conformation that is more similar to that found in the T state than the R state.
This means that AfHbs adopt a quaternary assembly, denoted H state, that is intermediate between the classic R and T states. Traditionally, the R/T quaternary transition is monitored by the amount of rotation which has to be applied to the $\alpha_2\beta_2$ dimer of the R state to optimally superimpose this dimer on the same dimer of the T state, after the superimposition of the corresponding $\alpha_1\beta_1$dimers. Indeed, on superimposition of the $\alpha_1\beta_1$ dimer of ferric HbTb with the deoxy (T) structure [45], a further rotation of 6.78° is required to superimpose the $\alpha_2\beta_2$ dimers. Similar values (about 4.78°), but with a rotation in the opposite direction, have been obtained superimposing ferric HbTb with its carbonmonoxy (R) structure [71], indicating that the H state has a quaternary structure that is intermediate between those of the high affinity R and low affinity T states. Furthermore, in the Root-effect hemoglobin HbTb acidification induces, also in the ferric state, a transition to the T state that is associated with the transition from hemichrome to pentacoordinate coordination of the β iron, suggesting an incompatibility of the ferric bis-His adduct within the T quaternary state [67]. Hemichrome formation has also been shown to occur in the α chains of horse Hb in the crystals of metHb by decreasing the pH of the crystallization mixture [132]. Since the quaternary assembly of horse Hb and AfHbs is very similar, this suggests a change in the relative flexibility of the two chains. In fact, horse Hb and AfHbs differ markedly. In the former, the hemichrome state was obtained as a result of a pH induced transition starting from a met-Hb single crystal. The solid-state transformation is coupled with extensive modifications of the packaging contacts and tertiary structure.
In common with other cases, the largest modifications are observed in the CDα region that converts from an extended loop at pH 7.1 to a F2 helix at pH 5.4, and packs against helix C of the β chain of a symmetry related molecule.
In particular, Phe46α moves more than 6 Å away from its position in the hydrophobic distal cavity to the surface, forming a p-stacking interaction with the side chain of symmetry related Arg40β, and the α-heme propionate groups of two adjacent

tetramers form an inter-tetramer hydrogen bond. Thus, the conformational change at the CD corner is intimately linked to the packing
interactions, and favors the transition to the hemichrome state. Despite this remarkable change, which affects a region directly involved in the $\alpha_1\beta_2$ ($\alpha_2\beta_1$) interface, the quaternary-structure modifications are negligible. The molecule fully maintains the standard R state organization of the original met-Hb form [132].

1.6 Scope of this thesis

The main scope of the present research work is the elucidation of the molecular mechanism undergoing un-known physiological functions of tetrameric Hbs, both recombinant and natural, both from human origin and Antarctic fish.
To analyze these systems a twofold methodological approach was adopted:

- **molecular** one, based on a combined crystallographic (microspectroscopy UV / VIS and Raman spectroscopy, X-ray diffraction), spectroscopic (UV / VIS, and Raman) and computational (MD) study, both on single crystals and solutions;
- **cellular** one, *ex vivo*, based on Raman imaging and optical tweezers study of human erythrocytes.

In particular, in the context of the **molecular** approach, my Ph.D. work was focused on the elucidation of two still unsolved problems in the chemistry of tetrameric Hbs:

1) the role of the bis-histidyl heme coordination in the Hb function and oxidation process;
2) the role of the tertiary and quaternary structure in the modulation of the Root effect.

The strategy undertaken for the execution of the research has been:
1a) a comparative experimental (spectroscopic and crystallographic) / computational study of the β-subunits of human hemoglobin (β-HbA) and of Hb from Antarctic fish *Trematomus bernacchii* (β-HbTb). Particularly the present workpackage has been carried out *via* two activities: a) the structural characterization of β-chain homotetramer of human Hb (β_4-HbA) in the ferric state (whose crystal structure is currently available only for carbomonoxy [139] and deoxygenated state [140]); b) the recombinant production, spectroscopic and computational characterization of the β subunit of Hb of *Trematomus bernacchii* (β-HbTb), compared the experimental data to those obtained for the β chain of HbA;
1b) a X-ray crystallographic /spectroscopic (micro-Resonance Raman)study of hemichrome formation in ferric Hbs from *Trematomus newnesi* (HbITn) and from sub-Antarctic fish *Eleginops maclovinus*. Particularly, the X-ray structure of HbITn, in the ferric state [oxidized by $K_3Fe(CN)_6$] has been compared with HbITn crystal structures available at different steps of oxidation (air-exposure).
The second objective, addressed to the identification of those tertiary and quaternary structure motives that influence the exogenous binding in Root-effect Hbs, has been approached through:

2a) equilibrium and crystallographic studies of oxygen (O_2) and carbon monoxide (CO) binding to the T-state HbTb crystals at pH 6.2 and 8.4 [57].
2b) combined crystallographic (X-ray diffraction)/ Resonance Raman (RR) microspectroscopic study on the mechanism of nitric oxide (NO) binding and release to the T-state HbTb crystals at two different pHs [57].
In addition, as mentioned above, my Ph.D. thesis also focused on a study at **cellular** level (*via* Raman imaging and Optical Tweezers) of healthy and C / S anemic erythrocytes [containing mutant hemoglobins HbS (β6Glu → Val) and HbC (β6Glu → Lys)], in order to define diagnostic protocols of these anemia.

Chapter 2

Methods

In this chapter a brief explanation of the techniques adopted during this Ph.D. thesis work is provided. Each dissertation about the theory behind the methods adopted is followed by the experimental conditions and procedures that have been utilized during this thesis work.

2.1 X-Ray Crystallography

The best technique currently available for visualizing the structures of macromolecules at atomic scale is X-ray diffraction analysis of single crystals. X-ray crystallography has transformed our understanding of biological processes.
The resolution of 3D structure of a biological macromolecule by X-ray crystallography is divided into several phases: *obtaining single crystals* of the macromolecule in question, the *collection of X-ray diffraction data*, *resolution of the phase problem* and *validation of the structure*.

2.1.1 Crystallization

Crystallization is the process of formations of solid crystals through the precipitation from a solution brought to oversaturation, meaning for crystal a solid whose constituents (for example protein molecules) are arranged in an orderly repeating pattern extending in all three spatial dimensions. In order to achieve successful protein crystallization, precipitation process must be quite slow to grant an ordered assembly of crystalline structures and a great number of variables have to be set up, since they directly influence the final results: sample purity, temperature, pH and appropriate buffers, precipitants and protein concentrations.
Below, the experimental procedures for the crystallization of hemoglobins investigated in this thesis are reported.

ferric-β_4-HbA

Oxyhemoglobin preparation

Oxyhemoglobin A was purified from hemolysate by a two-column method. Red cell debris were removed by centrifuging for 30 min at 10.000 x g. The supernatant was passed first through a Sephadex G-25 column equilibrated with 10 mM Hepes buffer at pH 6.9 and 1 mM EDTA and then through a CM-cellulose column equilibrated with the same buffer. HbO_2 was finally eluted with 10 mM Hepes buffer at pH 8.6. The purified HbO_2 solution was adjusted to pH 6.0 (for treatment with organic

mercurials) by filtration through a Sephadex G-25 equilibrated with in 30 mM phosphate buffer (pH 6.0), and in the presence of 0.1 M NaCl.

Isolation of Mercuribenzoated α and β chains

All separations were carried out with HbO_2 at low temperature (0-4 °C) by a two-column method. The procedure was essentially the same as described by Geraci et al. [141] and by Tsuruga et al. [142]. p-hydroxymercuribenzoate (PMB)(10 mg) was dissolved in 2 ml of 0.1 M NaOH and neutralized with 1 M CH_3COOH. This solution of PMB (100 μL) was reacted with 1 ml of HbO_2 solution (0.5 mM in heme) in 30 mM phosphate buffer, pH 6.0, and in the presence of 0.1 M NaCl. The solution was left overnight at 4°C, and the flocculent precipitate was removed by centrifugation. To obtain α-PMB chains, the mercurated HbO_2 solution was adjusted to pH 8.2 by filtration through a Sephadex G-25 column equilibrated with 15 mM Hepes buffer pH 8.2. The resultant solution was then passed through a DEAE-cellulose column equilibrated with the same buffer. Under these chromatographic conditions, the α-PMB chains were readily eluted out, whereas the β chains and unsplit HbO_2 were retained on the top of the column. To obtain β-PMB chains, on the other hand, the mercurated HbO_2 solution was adjusted to pH 6.7 by filtration through Sephadex G-25 in 10 mM phosphate buffer, pH 6.7. The resultant solution was then applied to a CM-cellulose column equilibrated with the same buffer. The unreacted HbO_2 and the mercurated a chains were retained on the top of the column at this pH, and only the β-PMB chains were eluted out completely.

Removal of Mercuribenzoate from α and β chains

PMB was removed from the α chains by incubating with 15 mM 2-mercaptoethanol in 10 mM Pipes buffer pH 6.5 for 10 min at 0 °C. The mixture was then applied to a CM-cellulose column, which had been equilibrated with 10 mM Pipes buffer, pH 6.5. The column was washed first with the same buffer containing 15 mM 2-mercaptoethanol. The mercaptoethanol was then removed by washing with the buffer alone for another 1 h, and the regenerated α chains were finally eluted in the oxy form with 30 mM Hepes buffer at pH 8.2, and stored in the oxy form to -20°C. For β-PMB, the chains were incubated with 20 mM 2-mercaptoethanol in 5 mM phosphate buffer pH 8.8 for 10 min at 0 °C. The solution was then placed on a DEAE-cellulose column equilibrated with 5 mM phosphate buffer, pH 8.8. The column was washed with 300 mL of the same buffer containing 20 mM 2-mercaptoethanol. The mercaptoethanol was then removed by washing with 10 mM Hepes buffer pH 8.2 (another 300 mL), and the regenerated β chains were finally obtained by changing the buffer concentration to 50 mM at the same pH.

Crystallization

Initial crystallization trials of β_4-HbA and β-PMB chain in the ferric state (by treatment with ferricyanide), were performed at 20°C through a screening of the crystallization

conditions found for carbomonoxy- β_4 and deoxy- β_4 [139, 140]. For β-PMB chain none of these trial was successful. Ferric β_4-HbA crystals were grown at pH 7.0 using the vapor diffusion technique (hanging drop). The drops were prepared by mixing equal volumes of protein solution (8 mg/ml) in 50 mM sodium phosphate buffer at pH 7.0, 20% glycerol (a stabilizing agent [142]) and reservoir solution containing 2.5M ammonium sulphate and 0.26 M sodium phosphate buffer at pH 7.0.

HbTb deoxy at acid and basic pHs

HbTb was purified from the hemolysate by ion-exchange chromatography as described earlier [71]. Crystallization trials taking into account the results reported by Mazzarella et al. [57]. The deoxy form of the protein at ~20 mg/mL (~$3x10^{-4}$ M) was prepared *in situ* from its carbomonoxy (HbTb-CO) derivative by decreasing the pH down to 6.2, exploiting its low affinity in acidic conditions (Root effect). To this end, for crystals at acid pH, at the protein solution in 100 mM Tris-HCl pH 7.6 buffer a volume 100 mM phosphate pH 5.5 is added, in order to bring the pH from 7.6 to 6.0, and to reduce to a final protein concentration of ~ 8 mg/ml (~$1x10^{-4}$ M). Since HbTb is endowed with the Root effect the acidification process rapidly leads to the transition from the R to the T-state and to the CO release. Deoxy-HbTb crystals were grown at pH 6.2 using the vapor diffusion technique (hanging drop) by mixing a 1 μL drop containing deoxy-HbTb at 8 mg/mL in 100 mM phosphate buffer, with a 1μL reservoir drop containing 12% w/v PEG 6000.
Similarly to the previous case, in order to obtain a solution of HbTb in T-state from which can grow crystals at basic pH, at the protein solution in 100 mM Tris-HCl pH 7.6, is added 60 mM phosphate buffer at pH 5.5, in a volume equivalent to that of protein solution. The pH of the solution is lowered to about 6, and the concentration is halved to ~10 mg/ml (~ 1.5 $x10^{-4}$ M).

Deoxy-HbTb crystals were grown at pH 8.4, in hanging drop, by mixing a 1 μL drop containing deoxy-HbTb at 10 mg/mL in phosphate buffer, with a 1μL reservoir drop containing 10% w/v PEG 6000, Tris-HCl 200 mM pH 8.4 and KCl 0.3 M. All crystallization experiments were carried at room temperature in an inert nitrogen atmosphere provided by a glove box ($[O_2]$ < 1 ppm). To prevent protein oxidation, 17 mM iron (II) citrate [143] and sodium dithionite were added to all crystallization trials at basic and acid pHs, respectively.

Preparation of nitrosyl-HbTb crystals

Nitrosylatd-HbTb crystals in the T-state were obtained through soaking of nitric oxide (NO) solution, prepared *in situ*, on crystals in the deoxy form. The crystals are treated with a solution of sodium nitrite and sodium dithionite at a relatively high concentration (in the molar ratio 1:2, see Table 2.1), which generates NO *in situ* according to the following reaction:

$$2NO_2^- + S_2O_4^{2-} \rightarrow 2NO + 2SO_3^{2-}$$

The dissolved NO diffuses into the crystal and binds the heme iron.
To prevent oxidative denitrosilation sodium ascorbate (10 mM) and bovine catalase (4000 units/ml) have have been added to the nitrosylant solution. Catalase removes traces of peroxides, which greatly accelerates the oxidation of hemoglobin. In Table 2.1 the composition of the stabilizing solution used for nitrosylation experiments is reported. The soaking time and concentration of precursors have been defined by Resonance Raman microscopy.

Table 2.1: Composition of the stabilizing solution for NO soaking experiments

Stabilizing solution used in NO soaking experiments		
	pH 6.2	**pH 8.4**
PEG 6000 w/v	15%	15%
KCl	-	300 mM
Tris/HCl pH 8.4	-	200 mM
$H_2PO_4^-/HPO_4^{2-}$	100 mM	-
sodium nitrite	15-30 mM	15-30 mM
sodium dithionite	30-60 mM	30-60 mM
sodium ascorbate	5-10 mM	5-10 mM
liver bovine catalase	4000 u/ml	4000 u/ml

Crystals of Hb from *Eleginops maclovinus*

Purification of major component Hb from *E. maclovinus* (Hb1Em) and the amino-acid sequencing of globins were carried out by Dr. Cinzia Verde and co-workers at CNR of Naples, as described previously [144].
Hb1Em stock solutions were kept in the carbomonoxy form. The formation of the carbomonoxy form was monitored by optical spectroscopy. Crystallization trials were performed at 277 K in a CO atmosphere provided by flushing the gas in the flask containing the crystallization reactors. Crystals were obtained using the dialysis technique with microdialysis buttons: 10 ml protein solution at 20 mg/ml in 100 mM Tris–HCl buffer pH 8.0 and 2 mM sodium dithionite was dialyzed against a 25 ml reservoir containing 2 M ammonium sulfate, 100 mM Tris–HCl pH 8.0 and 2 mM sodium dithionite. The quality of the crystals was then improved by fine-tuning the sulfate concentration. The best crystals were obtained in a week using 20 mg/ml Hb1Em and 1.8 M ammonium sulfate. In buttons in which crystallization had occurred, crystals with different crystal habits were observed. Crystals of the ferric form were prepared for resonance Raman experiments starting from carbomonoxy crystals by soaking a stabilizing solution containing 10 mM potassium ferricyanide into the crystals and then washing the excess off with stabilizing solution. The deoxy Hb crystals were obtained by treating crystals of the ferric form with degassed stabilizing solutions containing 10 mM sodium dithionite.

In Table 2.2 the best crystallization conditions of Hbs investigated are reported.

Table 2.2: Crystallization conditions of Hbs investigated.

ferric-β_4-HbA	deo-HbTb pH 8	deo-HbTb pH 6	Hb1Em
1.8 M ammonium sulphate 0.26 M sodium phosphate buffer pH 7.0 -hanging drop	10% PEG 6K, Tris-HCl 200 mM pH 8.4 0.3 M KCl 17mM iron (II) citrate - hanging drop	12% PEG 6K 100 mM phosphate buffer pH 6.2 2 mM sodium dithionite - hanging drop	1.8 M ammonium sulphate 0.1 M Tris/HCl pH 8 2 mM sodium dithionite -microdialysis

2.1.2 X-ray diffraction data collection

Diffraction data of Hbs crystals investigated in this thesis were collected from three different sources of X-ray: a conventional X-ray rotating anode, and two synchrotron lights:

- in-house on a Saturn944 CCD detector. The X-ray radiation used was CuKα radiation from a Rigaku Micromax 007 HF generator (wavelength 1.5418 Å);
- at the XRD1 beam line of ELETTRA, Trieste.
- at the PXII beam line of the Swiss Light Source (Paul Scherrer Institute, Villigen, Switzerland).

All crystals were flash-cooled at 100K in supercooled N_2 gas produced by an Oxford Cryosystem and maintained at 100K during the data collection, after the addition of 20% glycerol (v/v) (used as cryo-protective agent) to the stabilizing solution (solution with a concentration of precipitating agent higher, necessary to prevent crystal dissolution).

All the data were indexed, processed and scaled with HKL2000 [145]. This procedure is needed to associate the Bragg intensities and indices (hkl) for each reflection (indexing). Intensities of each reflection hkl were subsequently averaged from spots collected in several diffraction frames or form reflection related by symmetry. The internal consistency of the data collection is often measured by the following indicator:

$$R_{merge} = \frac{\sum_{hkl}\sum_{i}\left|I_i(hkl) - \overline{I(hkl)}\right|}{\sum_{hkl}\sum_{i} I_i(hkl)}$$

where I_i(hkl) is ith intensity measurement of the reflection hkl, including symmetry related reflections, and $\overline{I(hkl)}$ is its average. R_{merge} is a measure of the goodness of the diffraction data collection (the lower the better). In general, data with R_{merge} less than 10% are considered of good quality.

Detailed statistics on data collection, for each crystal, are reported in Chapters 3 and 4.

2.1.3 Structure determination and refinement

All the structures, solved by molecular replacement, were refined with SHELX program [146]: each refinement run performed with the program was followed by manual interventions using the program O [147] to correct minor errors in the positions of some side chains. Visual inspections were also performed to identify water molecule sites and to locate the ligand molecules.
At the end of the refinement the geometry of all the refined protein structures were monitored using PROCHECK [148] and WHATCHECK [149] programs.
All the figures were generated using Pymol (http://pymol.org).
Details of refinements are reported in Chapters 3 and 4.

2.1.4 Synchrotron light source

During this thesis X-ray and Raman data were also collected at the SLS synchrotron. A synchrotron light source provides the production of high intensity, collimate coherent and polarized electromagnetic radiations, that are artificially produced for scientific and technical purposes by specialized particle accelerators, typically accelerating electrons. A strong magnetic fields perpendicular to the beam, produced by ondulator magnets, is used to convert the high energy content of accelerated electrons into light or some other form of EM radiation simply inducing radial accelerations to the circulating particles.
This radiation is delivered at a tangential direction to electron storage ring, and thus it becomes available to users at beamlines.
Along beamlines, different instruments take place to control flux, wavelength selector, filters, light collimation control devices, focus device etc, depending on experimental targets. PXII beamline at SLS is supplied by X-ray radiation used for macromolecular crystallography. At the end of the PXII beamline, experimental core stations are located, where samples are in the line of radiation, and detectors are positioned to measure the resulting diffraction. An extremely high photon flux (2 x 1012 photons /sec /400 mA) in a small area (50 μm x 10 μm) is the most relevant feature of a synchrotron beamline.
Third generation synchrotron light sources, thanks to their capacity to grant high intensity and collimated coherent electromagnetic beams, are useful in a wide range of application including X-ray crystallography of proteins and other macromolecules and scattering analysis.

Elettra

SLS

Radiation dose determination
The X-ray total dose was evaluated according to the following formula:

$$D = \frac{E_t}{m} = \frac{I_0 E_{fc}[1 - e^{(\mu_{pe} t)}]}{m}$$

Where dose (D), is directly proportional to total energy (E_t) received by the crystal, and inversely proportional to crystal's mass (m).
Energy depends on the beam intensity (I_0), energy absorbed for photoelectric mechanism E_{fc} (Compton effect is minor in our data collection so omitted), and exposure factor related to the photoelectric effect [1-$e^{(\mu pe\ t)}$], where *t* is the exposure time; regarding the mass (m) of the crystal, it is obviously related to the volume (V) and the density of the crystal (ϱ); this latter can be drawn from the Matthew coefficient [150].

2.2 Spectroscopy and Microspectroscopy

2.2.1 UV-Vis Spectroscopy of hemoproteins

Ultraviolet (190-380 nm) and visible (380-750 nm) radiation interacts with matter which causes electronic transitions (promotion of electrons from the ground state to a high energy state). The electronic structure of hemoproteins, including hemoglobins, has dominated from protoporphyrin. The optical properties of the iron-protoporphyrin IX complex have been studied since many years [151] and are considered deriving from the highly conjugated π electron system. Two electronic transitions (giving rise to B and Q bands) dominate the visible region of the abr98sorption spectrum of iron-porphyrin complex, that corresponds to the porphyrin $\pi \rightarrow \pi^*$ singlet transitions. The B band corresponds to the $a_1u \rightarrow eg$ transition and the Q band to the $a_2u \rightarrow eg$ transition. There is a strong interaction between these two transitions, so that the transition dipoles are summed for the intense B band (also called Soret, about 400 nm) and nearly cancelled for the Q band (between 500nm to

600nm). Some intensity is regained by the Q transition *via* vibronic mixing [151], giving rise to the Q_0 (α) band and its vibronic envelope, Q_v (β) band.
Information about the oxidation, the spin and the coordination states of the heme iron can be obtained by the wavelength of the Soret, β and α bands of the UV-Vis spectra.
Furthermore, an extra band at longer wavelength (in the 600-700 nm region) is observed only for high-spin (HS) Fe^{3+} heme proteins, assigned to a charge-trasfer transition (CT1) from the porphyrin to the iron orbitals [$a_2u(\pi) \rightarrow eg(d\pi)$]. The intensity and the wavelength of the CT1 band are related to the energy difference between the d orbitals of the metal and the π orbitals of the porphyrins, which in turn, depend on the nature of the axial ligands [152].
Electronic absorption spectra of this thesis were measured with a double-beam Jasco spectrophotometer 530V. A 0.1 cm path-length cell with a 300 μl capacity was used.
Details of the single measures are reported in Chapter 3.

Peroxidase assays of β4-HbTb
Peroxidase activity was measured for β_4-HbTb at 20°C and pH 7 (phosphate buffer), according to a published procedure [67], using dopamine as substrate. Dopamine is a hydroxyquinone that can be oxidized to form the corresponding quinone and which eventually forms insoluble melanin. The samples were previously oxidized by addition of ferricyanide. A 0.9-ml sample of 50 mM sodium phosphate buffer at pH 7, containing hemoglobin and 4 mM of dopamine. The reaction was started by addition of 0.1 ml of 176 mM hydrogen peroxide solution, and monitored by the change in absorbance at 475 nm. The change in A_{475} was due to hemoglobin catalyzed oxidation of the substrate by H_2O_2. The peroxidase activity of HbA (only at 0.3 mg/ml) and HbTb was measured at and pH 7 for comparison.

2.2.2 VIS Microscopy

In this thesis in order to determine Oxygen Binding Curves (OBCs) of Hb crystals in the T-state a microspectrophotometer UV-Vis was used. This microspectrophotometer allows the determination of OBCs on sample of the order of a few micrometers in diameter. These measurements by myself were performed at University of Parma in collaboration with Prof. Andrea Mozzarelli.

Oxygen binding measurements to T-state HbTb crystals

Deoxy HbTb crystals, at pH 6.2 and 8.4, were washed with a stabilizing solution containing 30% (w/v) anaerobic PEG 6000 (within a deoxygenated glove box to prevents crystal damage caused by air-exposure), in presence of 2.5mM sodium ascorbate and 4000 units/ml catalase bovine. A drop of solution of the crystals was placed on the glass bottom of a Dvorak-Stotler flow cell [153] (see Figure 2.1) and

covered with a silicone membrane (MEM General Electric 213). This membrane is gas permeable and does not depolarize the linearly polarized light.

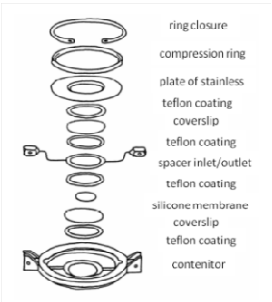

Figure 2.1: Dvorak-Stotler flow cell gas

The cell is placed on the thermostated stage of a polarized absorption microspectrophotometer (Zeiss MPM03), that consists of a UV-visible spectrophotometer single beam combined with an optical microscope equipped with 10x objectives ultrafluar-type and a polarizer Glan-Thompson to produce linearly polarized light and interfaced with a Calculator. The component parts, are summarized in Figure 2.2.

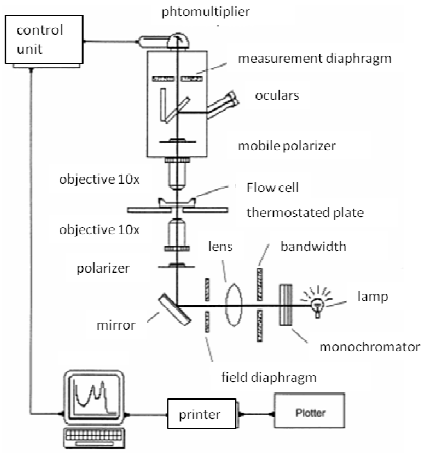

Figure 2.2: Scheme of the UV-VIS microscope.

The mixture was humidified by bubbling in two sealed cylinders containing approximately 120 ml of the same solution in which the crystals were suspended. The cell was sealed off above and below with Armaflex material (Armstrong). The temperatures were measured with a thermistor in contact with the plate of the microscope and corrected for the thermal gradient (<4° C). Oxygen pressures between 0 and 760 torr were prepared by mixing oxygen and helium with a gas mixture generator (Environics, series 200). The oxygen electrode was calibrated with

three certified oxygen gas mixtures—1%, 5%, and 21%—and pure oxygen. Experiments were performed by first exposing hemoglobin crystal to helium and then to a controlled oxygen pressure. Polarized absorption spectra, recorded as a function of oxygen pressure, were collected between 7.4 and ~742 torr. The spectra were collected in two directions of extinction, defined as maximum (// M) and minimum (//m) absorption. To obtain stable fractional saturations, polarized absorption spectra were recorded over a period of several hours at constant oxygen pressure. The estimation of the fraction of saturation was determined from reference spectra [154] obtained on other crystals at the same pH. The range of wavelengths analyzed for the deconvolution of the spectra was 470-600 nm.
Results of the single measures are reported in Chapter 4.

2.2.3 Basic principles of Raman spectroscopy

When the light is scattered from a molecule, most photons are elastically scattered (Rayleigh scattering). The scattered photons have the same energy (frequency) and wavelength of the incident photons. However, a small fraction of the light (approximately 1 in 10^7 photons) is scattered at optical frequencies usually lower then the frequency of the incident photons. The process leading to this inelastic scatter is termed *Raman effect*.
Elastic scattering, also known as *Rayleigh scattering* is the elastic scattering of light or other electromagnetic radiations by particles much smaller than the wavelength of light itself. Scattered photons present the same wavelength and frequency than incident photons resulting in no energy losses.
A small fraction of the scattered light is scattered following *Raman Effect* mechanism (inelastic scattering), with the scattered photons having a frequency different from the frequency of incident photons.
Describing this phenomenon in terms of energy exchanges, a photon at fixed frequency (ν_0) with an energy content described by $h\nu_0$,from a laser source, interacting with a molecule brings this latter from its fundamental state (ground state in image) to an excited *virtual energy level*. In case of elastic scattering, decay brings to the emission of a photon with $\nu_e = \nu_0$ and the molecule returns to its fundamental state; in *Raman Stokes* scattering cases, instead, decay brings not the molecule to its ground level but to a different vibrational energy state: emitted photon will have a *stokes* frequency defined as:

$$\nu_0 - \nu_e = \nu_{st}$$

If the starting condition of sample molecule is an energized state and, after excitation, decay brings it to ground level, we talk about *Raman anti-stokes* scattering .
In anti-stokes energy content is defined as:

$$\nu_0 + \nu_e = \nu_{ast}$$

In this thesis we consider only Raman Stokes lines. These differences between incident and emitted frequencies are referred to as Raman shift which, in spectroscopic and microscopic Raman applications, is usually expressed in terms of wavenumber (cm^{-1}):

$$\Delta\omega_{cm\text{-}1} = (\nu_0 - \nu_{st})/c$$

Where c represents the speed of light.

2.2.4 Resonance Raman (RR) spectroscopy of hemoproteins

The Raman scattering cross section considerably increases if the laser frequency matches a transition frequency of the molecule (Resonance Raman effect) [155, 156]. If the wavelength of the exciting laser is within the electronic spectrum of a molecule, the intensity of some Raman-active vibrations increases by a factor of 10^2-10^4. RR spectroscopy represents an important investigative tool to characterize hemoproteins [123, 157] and can occur either by exciting in the Soret band or in the α, β bands. The resulting RR spectrum provides information only on the heme group, becoming effectively invisible bands of the protein matrix.

Upon Soret excitation, the RR spectrum in the high frequency region from about 1300 to 1700 cm^{-1} consists of in-plane porphyrin vibrations. This region contains the oxidation marker band ν_4, which provides information about the oxidation state of the metal atom, the *core size* marker bands, ν_2, ν_3, ν_{10} which provide information about the coordination and the spin state of the metal, and the vinyl ν(C=C) stretches between 1600-1640 cm^{-1}.

2.2.5 Raman micro-spectroscopy

Raman microspectroscopy offers several advantages for microscopic analysis since it is a scattering technique, samples do not need to be fixed or sectioned. Moreover, data can be collected from a very small volume and water does not generally interfere with Raman spectral analysis. Thus, Raman spectroscopy is suitable for the microscopic examination of commonly water rich samples, such as biological systems.

Data from two different Raman microscopes were analyzed during this thesis. Raman data were collected in house using a commercial JASCO NRS-3100 Raman microscope system at the University of Naples (scheme in Figure 2.3), with excitation wavelength 514.5 and 647.4 nm (assembled during this thesis, see appendix), and a home-built Raman microscope integrated at the PXII beam line of the Swiss Light Source (SLS, Paul Scherrer Institute, Villigen, Switzerland), with excitation wavelength, 405 nm.

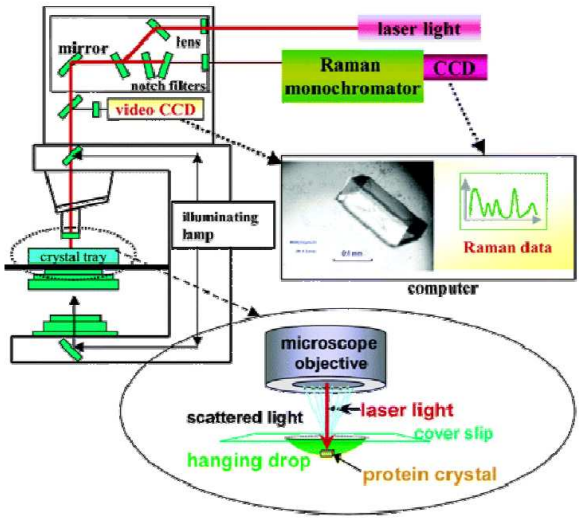

***Figure 2.3**: Raman microscope system sample scheme.*

Raman microscope (in-house) apparatus consisting of a confocal Raman instrument (Jasco NRS - 3100) equipped with an Olympus microscope (5X, 20X, 100X). Resonance Raman (RR) spectra were obtained at room temperature focusing an air-cooled Ar^+ laser (Melles Griot, 35 LAP 431-220 with 488, 458, 514.5 and 647.4 nm line, 125 mW maximum power) to a spot size of approximately 4 μm by a 20 X objective. A holographic notch filter was used to reject the excitation laser line from the scattered light. Raman scattering was dispersed through a monochromator (1200 grooves mm^{-1} grating) and collected, using a Peltier-cooled, through a 1024x128 pixel CCD photon detector (Andor DU401BVI). Typically, several 2 min spectra (7 cm^{-1} resolution) were recorded and averaged using a standard software routine. The RR spectra were calibrated using CCl_4 and indene as a standard.
Experiments were performed keeping the crystals in a 1 ml drop of mother liquor. Crystals were transferred from plates to a single hanging-drop reactor and then analyzed.
Details of singles Raman measures in Chapter 3 and 4 are reported.

2.2.6 Basic principles of Circular Dichroism (CD)

CD is widely adopted to obtain structural informations about biological macromolecules in solution [158], in particular: i) to verify protein correct folding; ii) to estimate secondary structure percentage [158]; iii) to perform protein stability study in function of chemical-physical parameters variation (e.g. pH, temperature [159], denaturant concentration [160]; iv) to follow possible conformational variations because of protein-ligand interaction; v) to study kinetics of folding study [161].

Absorption spectrum of a protein in the near-UV region (250-300 nm) is dominated by π→π* transitions of the aromatic side-chains (e.g. Trp, Tyr and Phe). The electronic transitions, n→π* and π→π* of peptide bond are instead responsible for the much more intense bands in the far-UV region (180-250 nm). The particular arrangement of peptide chain in disymmetric secondary structures (e.g. α-helix, β-sheet, random coil) produces different CD spectra profiles. In particular CD spectrum of an α-helix presents a negative peak corresponding to n→π* transition at 222 nm, and two other peaks the former negative (208nm) and the latter positive (191nm), corresponding to π→π* transition. CD spectrum of a β-sheet presents a negative peak at about 217 nm and a positive one at 195 nm, each one corresponding to n→π* transition. Random coil spectrum shows an intense negative peak around 200 nm, very often accompanied by a less intense peak either positive or negative at higher wavelengths. CD spectrum of a native protein is function of the percentage of α-helix, β-sheet and random coil composing the molecule. The protein spectrum can be deconvoluted into the single structural contributions.
Circular dichroism (CD) spectra of this thesis were recorded at 10°C with a Jasco J-715 spectropolarimeter equipped with a Peltier-type temperature control system (model PTC-348WI). A 0.1 cm path-length cell with a 300 µl capacity and a protein concentration 0.1 mg mL^{-1} were used.

2.3 Recombinant production and purification of β-HbTb

E. coli strain BL21 (DE3) [supE44 F- ompT hsdsB (rB-mB-) gal dcm (DE3)] was routinely used for cloning and expressing recombinant protein. Plasmid pET-22b(+) (Novagen) was used for cloning and expression. Restriction and modifying enzymes were obtained from Promega. The gene Δ1HbTbβ was custom synthesized from GENEART through the optimization of codon usage [162]. The synthetic gene Δ1HbTbβ was inserted between the NdeI and BamHI sites in the plasmid pET-22b(+) (Figure 2.4).

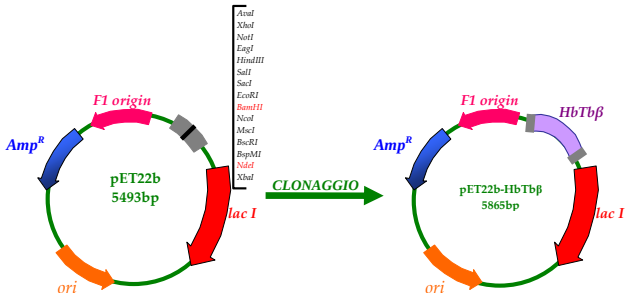

Figure 2.4: Vector pET22b-HbTbβ.

Cell were grown in Luria-Bertani (LB) medium at 25°C. When required, ampicillin was added at 100 mg/mL. For the over-expression of β-HbTb protein, a proper preinoculum of recombinant E. coli BL21 (DE3) (pET-22b(+)-Δ1HbTbβ) cells (overnight grown at 25°C) was inoculated in 2.5 L of LB medium in presence of

ampicillin in a 7.5-L Techfors S (Infors HT Switzerland) automatic fermenter. During the whole production process pH was controlled at 7.00, temperature was kept at 25°C, air flow was fixed at 5 L/h while stirring was changed in the range 200-500 rpm to maintain dissolved oxygen tension (DOT) always above 70% saturation. Cell were grown till the culture density reached the value of 0.6 O.D. Induction was then performed by 1 mM isopropyl-β-D-thiogalactopyranoside (IPTG), in the presence of 0.6 mM of D-aminolevulinic acid and 30 μM FeCl3 and production process prolonged for further 16-18 h. Average final cell density resulted to be 15 OD 600nm/mL. Biomass was then harvested by centrifugation, and the wet bacterial pellet was re-suspended in 10 mM Tris/HCl, pH 8.6, in the presence of 1mM phenylmethylsulfonyl fluoride (PMSF) and 1mg/mL lysozyme. Samples were kept on ice and disrupted by sonication using an Branson sonicator (Model B-15), using a program consisting of 30 cycles (30" ON, 30" OFF, intensity 4.5). After disruption of the cells, samples were centrifuged at 7000 rpm for 15 min at a constant temperature of 4°C. The supernatant was discarded, and the inclusion bodies fraction was washed twice with chilled water, divided in several aliquots and incubated overnight for the solubilisation at 4°C in 40 mM Tris/HCl, pH 8.0 buffer containing 0.2% N-lauroylsarcosine. After the incubation, the mixture was centrifugated at 10000 rpm for 15 minutes at 4°C. The supernatant containing the protein of interest was re-saturated to CO gas. The supernatant was passed through a Sephadex G-75 column (16/60 HiLoad GE Healthcare) equilibrated with degassed and CO-saturated buffer 40 mM Tris/HCl pH 8, 80 mM NaCl, 0,06% N-lauroylsarcosine. β-HbTb was eluted for 60 mL at a flow rate of 700 μL/min, following the heme absorbance at 410 nm and protein absorbance at 280 nm. The fractions were pooled, gently bubbled with CO, concentrated through Amicon membranes (MWCO 5000 Da) and stored to -80°C. The hemoglobin was reconstituted from the purified apo-protein by reaction with hemin. A stock solution of 50 mM hemin was prepared as follows: 32.5 mg bovine hemin was dissolved in 0.1 mL of 0.1N NaOH and 0.9 mL of deionized water. The reaction to apo-globin to hemin was conducted at 4°C in 40 mM Tris/HCl, pH 8.0 buffer containing 0.2% N-lauroylsarcosine, respecting stoichiometry 2:1 between the prostetic group and apo-protein. The fraction of hemin in excess was removed from the supernatant by centrifugation of the sample. Confirmation of reconstituted protein was evaluated by UV-visible spectroscopy.
Results of the single experiments in Chapter 3 are reported.

2.4 Molecular dynamics simulations of β-HbTb and β-HbA

The coordinates of the β-chain of *T. bernacchii* Hb were obtained from the X-ray structure of the HbTb hemichrome state (PDB code 1S5X) [163]. The missing residues were modeled using the structure of the β-chain of HbTb from the CO form of the same protein (PDB code 1PBX) [71]. In particular, the PDB entry 1S5X has residues 45–52 disordered, whereas the same residues are ordered in the PDB entry 1PBX. Thus, the use of both these structures allowed us to build a model of the

complete form using available crystal structure data. The Z-score value of the combined statistical potential energy of the model was −6.47, analogous to that calculated for other monomeric globin chains, and of that of the starting template which is equal to -5.94. These values are in the range of scores typically found in proteins of similar sequence length. The *Z*-score indicates overall model quality and measures the deviation of the total energy of the structure with respect to an energy distribution derived from random conformations [164, 165]. The model was then used to obtain the structure of the bis-His form of the β chain of HbA (β-HbA).

Molecular dynamics (MD) simulations for β-HbTb and β-HbA were done using GROMACS software (Groningen Machine for Chemical simulations), version 4.0.5, and all-atom ff03 force field [166]. The heme parameters were calculated using Density Functional Theory adopting the B3LYP functional [167] in conjunction with the following basis set: Hay and Wadt Effective Core Potential (ECP) [168] for iron and double-zeta basis set for core and valence electrons, respectively; 6-311++G(d,p) basis set for the atoms directly connected to iron and, finally, 6-31G for the remaining atoms. The calculations have been done using Gaussian98 [169] and GamessUS packages [170].

The parameters used in this paper are in very good agreement with those calculated by other authors [171].

Before the regular MD production runs, the systems were minimized using a procedure previously reported in other works [172-174]. The starting models were immersed in a box containing about 7500 simple-point-charge [175] water molecules. The ionisation state was set to mimic a neutral pH environment. The overall charge of the systems was neutralized by adding the appropriate number of ions more than 7 Å away from the protein surface. In the first step of the equilibration process, the solvent was relaxed by energy minimization followed by a 50 ps MD at 300K. The overall systems were then minimized without restraints, before the productive run. 35 ns MD simulations have been collected. The simulations show extensive sampling of the conformational space around the folded state and allow us to address issues related to the stability of the bis-histidyl ferric form of β-HbTb and β-HbA. All bond lengths were constrained by LINCS [176]; Newton's equations of motion were integrated with a time step of 2 fs and atomic coordinates were saved for analyses every 0.5 ps. A relative dielectric constant of 1 was used. The Part Mesh Ewald method (PME) [177] was used for the treatment of electrostatic interactions for atoms at a distance greater than 9 Å. All systems were simulated in the NVT ensemble at 300K using periodic boundary conditions in the three coordinate directions and constraining the molecule in the centre of the simulation box. The temperature was kept constant using the Berendsen thermostat with a coupling constant $\tau p=1$ fs [178]. Only for comparative purpose, in the case of β-HbTb, an additional simulation of 35ns was performed using different initial velocity. The similarity of the results achieved in the two simulations indicates that they are virtually identical. Therefore, the analysis reported will be limited to only one simulation. In the text (Chapter 3), the

six major and the two short α-helices that make up the structures of β-HbTb and β-HbA are labelled A through H, according to the traditional naming scheme of globins. Details of the simalutaions in Chapter 3 are reported.

Chapter 3

Role of bis-histidyl adducts in tetrameric hemoglobins

In recent years, there has been an increasing interest in Hbs isolated from fish living in the unusual environment of the Antarctic Ocean (AfHbs). Not only these studies have provided clues on the mechanism of Hb adaptation to these extreme conditions, but they have also been important for the elucidation of general properties of fish Hbs [65, 75]. Although the R and T canonical structures of high-Antarctic fish ferrous Hbs have been shown to be very close to those of temperate fish, but remarkable differences have emerged from the investigation of their ferric forms.

In contrast to mammalian and temperate fish Hbs, that essentially oxidize in their folded state to aquo/hydroxyl metHb forms, AfHbs oxidation leads to the formation at the β subunits of bis-histidyl adducts [43-45] and pentacoordinated ferric states [44, 45, 74, 113], that are typically associated with Hbs with lower structural complexity (monomeric and dimeric) [125, 179].

Furthermore, crystallographic studies of ferric AfHbs, have demonstrated that the closure movement of the EF fragment associated with hemichrome formation propagates to other structural elements of the tertiary structure of the β subunit, directly involved in the quaternary assembly of the molecule. Indeed AfHbs adopt a quaternary assembly (denoted H state) that is intermediate between the classic R and T states [45]. These findings have recently re-opened the questions on i) the role of heterogeneity arising from different behaviour of the α and β chains [43, 75], and (ii) the landscape of accessible quaternary structures [45, 75] potentially relevant in the interpretation of the role of physiological effectors and of the Root effect in regulating the function of Hb.

With the aim to characterize both the structural determinants and details on the mechanism of hemichrome formation in tetrameric Hbs, the work strategy was divided into two fields of investigation:

1) A comparative experimental (spectroscopic and crystallographic) / computational study of the β subunits from human hemoglobin (HbA) and from *T. bernacchii* Hb (HbTb).

2) A crystallographic /spectroscopic study of hemichrome formation in Hb from Antarctic and sub-Antarctic fish.

3.1 Comparative experimental (spectroscopic and crystallographic) /computational study of the β subunits of HbA and HbTb

Crystal structure of β_4-HbA in the ferric state (whose crystal structure is currently available only for carbomonoxy [139] and deoxy state [140]) is obtained starting from separated β chains. The separated oxy β-globin chains from HbA ($\alpha_2\beta_2$) carried out with according to the method of Geraci et al. [141] and Tsuruga et al. [142] using p-hydroxymercuribenzoate (PMB) (see Methods for further details). In solutions β chains readily associate into tightly assembled β_4 homo-tetramers [180].
The recombinant β subunit of Hb from *Trematomus bernacchii* (β-HbTb) was expressed (see Methods for furher details) in collaboration with Prof. M. L. Tutino, University of Naples "Federico II". The recombinant production was accompanied by a spectroscopic characterization and a molecular dynamics study. The experimental and computational data have been compared with those obtained for the β chain of HbA.
Below are discussed separately the results obtained.

3.1.1 Crystal structure of β-chain homotetramer of human Hb in the ferric state (ferric-β_4-HbA)

After a screening of the crystallization conditions found in literature for carbomonoxy-β_4 (CO-β_4)[139] and deoxygenated-β_4-HbA (deoxy-β_4)[140] good quality crystals of ferric-β_4-HbA, from the solution oxidized by potassium ferricyanide and containing a mixture of hemichrome /aquo-met state (see par. 3.1.3.1) have obtained (Figure 3.1). These crystals belong to the space group $P2_1$ and diffract up to a resolution of 2.1 Å.

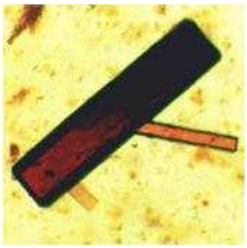

Figure 3.1: Best crystals of ferric β_4-HbA.

Ferric-β_4-HbA crystals were prepared for data collection by fast transfer into cryo-protectant solution containing 2.7 M ammonium sulphate with 20% glycerol (as cryo-protective agent).
Diffraction data were collected in-house at 100K. All the data were indexed, processed and scaled with HKL2000 [145]. Detailed statistics on data collection are reported in Table 3.1. Matthews coefficient [150] calculation suggested the presence of one tetramer in the asymmetric unit (Figure 3.2).

Table 3.1: X-ray data collection statistics for ferric-β_4-HbA

Crystal data	
Space group	$P2_1$
Unit-cell parameters	
a (Å)	62.48
b (Å)	82.02
c (Å)	52.71
α (°)	90.00
β (°)	91.32
γ (°)	90.00
Data processing	
Resolution limits (Å)	50.00-2.1
No. of observations	368306
No. of unique reflections	85626
Completeness (%)	96.1 (94.1)
I/σ (I)	20.6 (4.9)
Average multiplicity	2.9 (2.8)
Rmerge (%)	0.091 (0.40)

*R*merge = $\Sigma hkl \Sigma_i |I_i(hkl) - \langle I_i(hkl) \rangle| / \Sigma hkl \Sigma_i I_i(hkl)$, where $I_i(hkl)$ is i_{th} intensity measurement of the reflection hkl, including symmetry related reflections, and $\langle I_i(hkl) \rangle$ is its average. Values in brackets are for the highest resolution shell.

Structure of ferric-β_4-HbA were solved by molecular replacement using the program AMoRE [181] and the structure of CO-β_4 (PDB code 1CBM) [139] as a starting model. The refinement was performed using the program SHELX [146]. The refinement runs were followed by manual intervention using the molecular graphic program O [147], to correct minor errors in the position of the side chains. Water molecules were identified by evaluating the shape of the electron density and the distance of potential hydrogen bond donors and acceptors. The structure of ferric-β_4-HbA has been partially refined to a R_{factor} of 0.225 (R_{free} 0.309) by using diffraction data (368306 reflections) in the resolution range 50.0–2.2 Å. The electron density is well defined for both the main chain and the side chains of most of the residues. A summary of the refinement statistics is presented in Table 3.2. The stereochemical parameters of the refined structure (Table 3.2) are in close agreement with those obtained for well-refined protein structures at 2.0-Å resolution. In particular, 91.9% of the residues are located in the most favored regions of the Ramachandran plot.

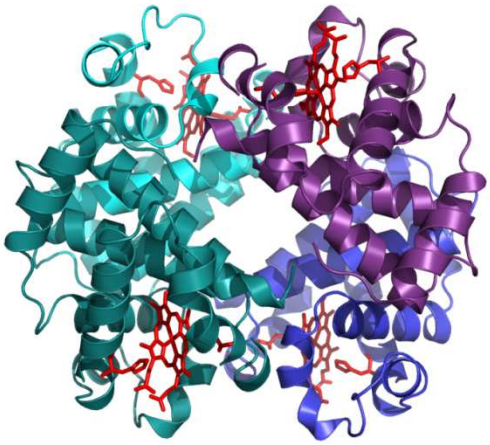

Figure 3.2: Cartoon representation of the overall structure of ferric-β_4-HbA**.** Heme goups are shown in red.

Table 3.2: Refinement statistics for ferric-β_4-HbA

Refinement Results	
R/R_{free}	22.5%/30.9%
No. of atoms	
water molecules	234
No. of residues	584
RMSD from ideal values	
Bond lengths (Å)	0.006
Bond angles (°)	1.727
Average B-factors (Å^2)	
Protein, overall	24.79
Main chains	26.59
Side chains	24.44
Solvent atoms	33.20
Ramachandran plot statistics	
Residues in the most favored regions (%)	91.9%
Residues in the additionally allowed regions (%)	8.1%

The correspondence between the subunits of the β_4 homo-tetramer and those of the $\alpha_2\beta_2$ hetero-tetramer is following:

$\alpha_2\beta_2$-HbA	β_4-HbA
α_1	β_4
β_1	β_1
α_2	β_3
β_2	β_2

|Fo-Fc| electron density maps show that in all four crystallographically independent chains the heme iron (III) hosts 6c high spin (HS) aquo-met coordination, with no trace of bis-histidyl adduct (Figure 3.3). Indeed, the heme pockets are not compatible with an endogenous coordination, that would require a Cα(HisF8)-Cα(HisE7) distance lower that 13 Å (Table 3.3) [108, 123]. Therefore, the crystal structure represent only the aquomet fraction of the sample present in solution, whereas the bis-His adduct does not co-crystallize.
In Table 3.3 the distance of water molecule from heme iron in the four subunits are also reported.

Table 3.3 Heme Stereochemistry of β subunits of ferric-β_4-HbA. Distances in Å.

	H_2O---Fe(III)	H_2O ---$N^{\varepsilon 2}$ (HisE7)	Fe(III)--- $N^{\varepsilon 2}$ (HisF8)	Cα(HisF8)---Cα(HisE7)
β_1	1.76	2.50	2.02	14.0
β_2	2.03	2.67	2.02	14.1
β_3	1.77	2.60	1.97	13.9
β_4	2.13	2.57	2.00	14.0

The location of the water molecule and its interaction with the iron in β_1 and β_3 is slightly smaller than those observed in mammalian Hb aquomet states, which are characterized by Fe-water distance of ~2.1 Å [74].

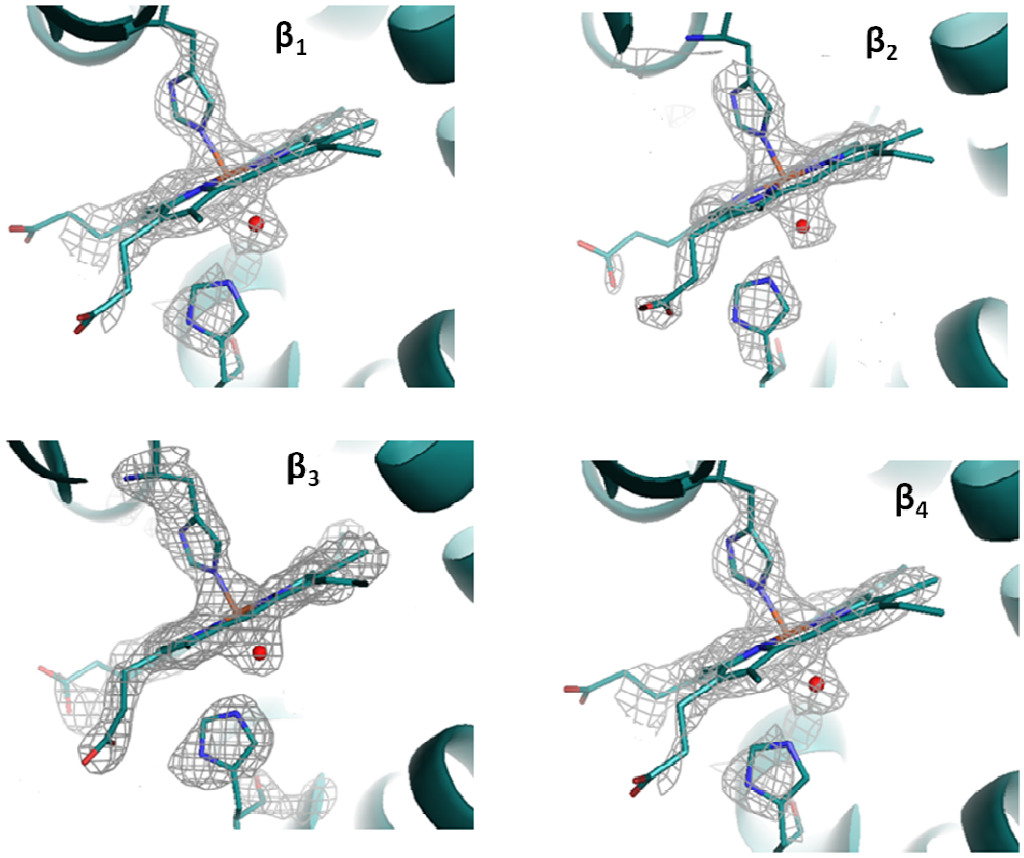

Figure 3.3: Omit |Fo-Fc| electron density maps (contoured at 3.0 σ) of hemes group of the four crystallographically independent chains of ferric β_4-HbA.

Particularly interesting is the region of the interfaces $\beta_1\beta_4$ ($\beta_2\beta_3$). Examination of the electron density maps clearly shows the presence of two disulfide bridges between Cys112(G14) residues at the $\beta_1\beta_4$ ($\beta_2\beta_3$) interfaces (in Figure 3.4 the disulfide bridge at the $\beta_1\beta_4$ inteface is reported).
These bonds seem not to influence the heme coordination in ferric-β_4-HbA. Although the Cys residues are located at the right distance (Cα-Cα and thiol groups distances are about 4.6 Å and 2 Å respectively), the conformation of disulfide bridges is out of the canonical values reported [182], indicating the existence of some costrains (Table 3.4).

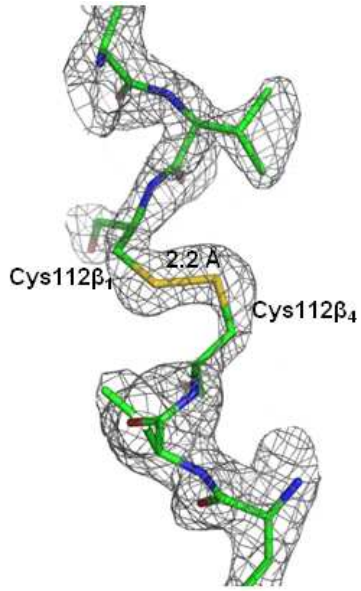

Figure 3.4: |2*Fo* - *Fc*| electron density maps (contoured at 2.4σ) for Val111(G13) and Cys112(G14) residues at the $\beta_1\beta_4$ interface.

Table 3.4 Stereochemistry of disulfide bonds at the $\beta_1\beta_4$ ($\beta_2\beta_3$) interfaces of ferric-β_4-HbA.

	φ (°)	ψ (°)	ω (°)	χ_1 (°)	χ_2 (°)	χ_3 (°)
Cys112β_1	-60.1	-42.2	-144	-96	31	-114
Cys112β_4	-72.3	-24.3	174	-69.8	-18	-144
Cys112β_2	-70.0	-30.0	177	-80	-12	-127
Cys112β_3	-67.4	-33.	178	-108	38	-127

These findings confirm previous indirect indications[183, 184]. It is known that the recombinant production of human β-globin in *E. coli*, produces a mixture containing monomeric and dimeric forms of β-globin, characterized from disulfide bond between cysteine residues (probably due to oxidation either in bacteria or during purification)[183].

In crystal structures of CO-β_4 and deoxy-β_4 [139, 140] disulfide bridges are absent, confirming that they are produced by the oxidation *via* ferricyanide. The Cys112 residues adopt dual conformations: the authors conclude that when both sulfhydryl are oriented toward the $\beta_1\beta_4$ ($\beta_2\beta_3$) dyad, the two Cys112 residues must alternate conformation in unison, "like the motion of a car's windshield wipers" [139]. In addition it has been previously observed that Cys112β(G14) is a critical amino acid in formation of stable β_4 tetramers, as well as αβ dimers in $\alpha_2\beta_2$ hetero-tetramer [185]. Indeed, mutagenic studies have reported that β_4 formation *in vitro* can be inhibited (Cys→ Asp) or enhanced (Cys→ Val) by the amino acid at β112 [184]**.** In $\alpha_2\beta_2$ hetero-tetramer substitution of Cys112β with Val inhibits tetramer dissociation, stabilizing αβ

dimers, whereas substitution of Cys112β with Ser or Asp promotes dissociation, destabilizing αβ hydrophobic interactions[185].
It is noteworthy that in fish Hb two cysteine residues highly conserved, Cys31β and Cys109β, although very close in the quaternary structure, have never been involved in disulfide bond.
The β_4 tetramer, unlike the $\alpha_2\beta_2$ tetramer, has high oxygen affinity and does not bind oxygen cooperatively [78]. X-ray structures of the CO and deoxygenated form have confirmed that β_4 tetramer has a R-like quaternary structure [139, 140].
The overall structure of ferric-β_4-HbA, as expected, is very similar to those of CO-β_4 and deoxy-β_4 (Figure 3.5). Indeed, the overall root mean square deviation (RMSD) based on the Cα atoms between CO-β_4 and deoxy-β_4 were 0.45 Å and 0.62 Å, respectively.

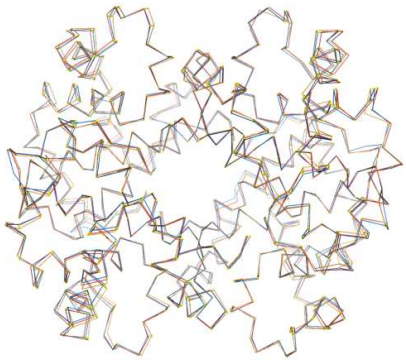

Figure 3.5: Superimposition of the Cα atoms of ferric-β_4-HbA (in marine blue) of CO-β_4-HbA (in orange, PDB code: 1CBM) and of deoxy-β_4-HbA (red, PDB code: 1CBL).

These findings are also corroborated by the analysis of difference distance matrices (DDM). The DDM is indeed a sensitive probe for investigating structural differences between two models [186]. In this procedure, distances between pairs of Cα atoms are measured in each model. The differences in the corresponding Cα distances between the two models are then evaluated and used as elements of the matrix. In each map the white regions show no structural change, blue regions represent residues that move closer in the second structure, whereas the converse happens in the red regions. The DDM of the structures of ferric-β_4-HbA, CO-β_4 and deoxy-β_4 were computed by using the program DDMP (http://www.csb.yale.edu/userguides/datamanip/ddmp/ddmp_descrip.html) (Figures 3.6 and 3.7 A and B).

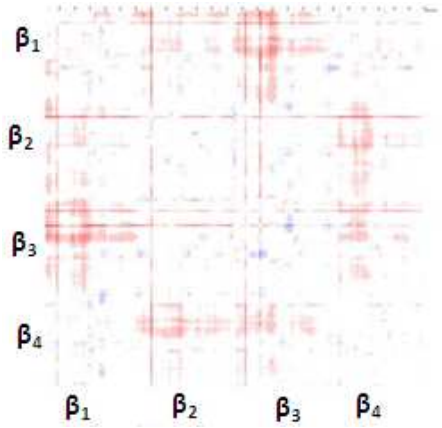

Figure 3.6: Difference distance matrices of deoxy-β_4 *vs* CO-β_4, as reference. The color range extends from -2 Å (dark red) to 2 Å (dark blue).

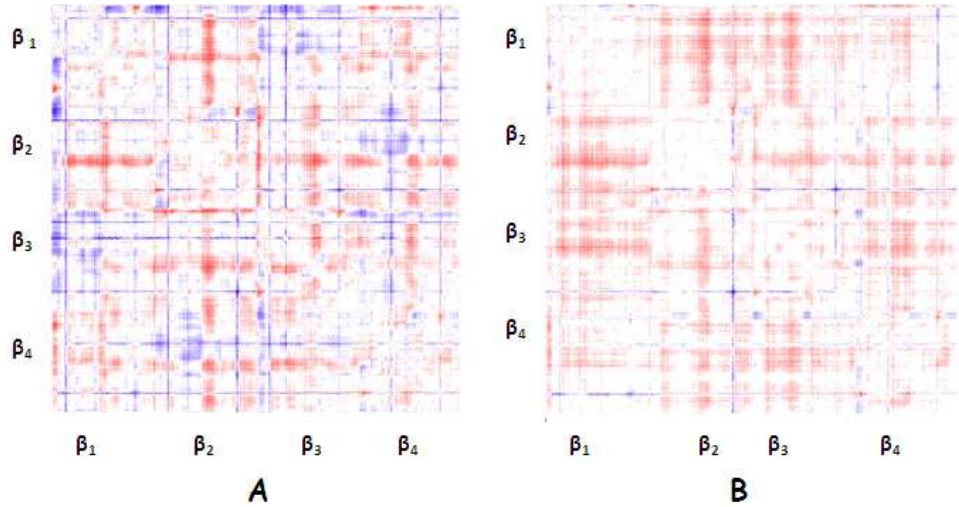

Figure 3.7: Difference distance matrices of A) ferric-β_4 *vs* deoxy-β_4 and B) ferric-β_4 *vs* CO-β_4. The color range extends from -2 Å (dark red) to 2 Å (dark blue).

A comparative analysis of the diagrams, reported in Figures 3.6 and 3.7 (A and B), clearly shows that the three structures examinated are very similar and indicates that no quaternary structure modification occurs in the ferric state.
In particular slight changes were found in DDM of ferric-β_4 and deoxy-β_4 corresponding at the interfaces region (Figure 3.7A).

3.1.2 Expression and purification of the β subunit of Hb from *Trematomus bernacchii* (β-HbTb)

The amino terminal sequence of the β subunit of *T. bernacchii* is Met-Val. In eukaryotic cells the N-formil-methionine is always cleaved, leaving valine as the amino terminal residue of mature protein. On the contrary, prokaryotes are quite inefficient in removing the initial methionine. Since the length of amino terminal portion of Hb chains plays crucial roles in modulating the oxygen affinity, we have carried out the recombinant production of β1Val→Met mutant, hereafter referred to as β-HbTb, in *E. coli* using the Δ1HbTbβ synthetic gene [187]. This gene was designed to optimize the codon usage for the recombinant production in *E. coli* cells. The gene was cloned into pET22b, thus generating the recombinant pET22b-Δ1HbTbβ plasmid. *E. coli* BL21(DE3) cells were transformed with the recombinant vector and, the production of the β-HbTb was carried out at 25°C, considering that the Hb is a protein from an Antarctic fish. The production process was carried out in an automatic fermenter and the induction was then performed by IPTG, in presence of D-aminolevulinic acid and $FeCl_3$. Then, cells coming from the production process were analyzed looking for production and soluble/insoluble distribution of the recombinant protein by cell fractionation followed by SDS-PAGE analysis (Figure 3.8 A). The production processes resulted in the total deposition of recombinant β-HbTb as inclusion bodies (IBs) (Figure 3.8 A). Treatment of IBs with different non-denaturing solvents, such as of mild detergents or polar solvents at low concentration, was applied to the recovery of the recombinant protein in solution. The best recovery in solution was obtained in 0.2% N-lauroyl sarcosine; in this condition, the corresponding solubilization yields exceeded 98% (Figure 3.8 B).

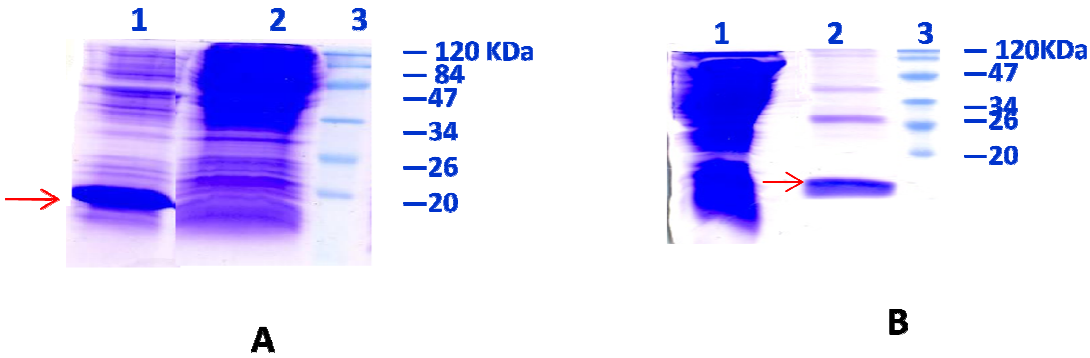

Figure 3.8: SDS–PAGE (12%) analysis. **A)** Lane 1: patterns of protein expression of the sonicates cell, insoluble fraction; lane 2: patterns of protein expression of the sonicates cell, soluble fraction; lane 3: molecular weight markers. **B)** Lane 1: patterns of protein of the inclusion bodies; lane 2: fraction resolubilized with 0.2% N-lauroyl sarcosine; lane 3: molecular weight markers. Each lanes were loaded with 5 μg of proteins. The red arrows indicate the position of β-HbTb.

Some recent reports have shown that the aggregation into IBs does not necessarily mean that the target protein is unfolded [188]. It is indeed now largely accepted that properly folded proteins are usual components of IBs [188, 189], confuting the consolidated idea that solubility of recombinant protein directly implies protein conformational quality [190, 191]. It has been observed that IBs containing a high proportion of correctly folded protein can be easily solubilized under non-denaturing conditions [192] by using mild detergents or polar solvents, widely preserving the target protein folding. Our data indicated that the designed production process allowed the production of a folded protein as indicated by Circular Dichroism analysis (CD) (Figure 3.9), but spectroscopic analysis revealed that the globin is partially present as apo-protein.

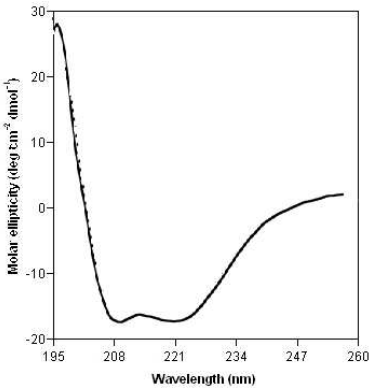

Figure 3.9: CD spectrum of apo-globin in the far-ultraviolet region, at 10°C in sodium phosphate buffer 40 mM pH 8.0 and 0.2% N-lauroyl sarcosine, with a protein concentration of 0.1 mg mL^{-1}. CD spectrum has the 2 negative maxima at 222 and 208 nm, typical for largely α-helical proteins.

The solubilized β-HbTb was purified by gel-filtration chromatography (Figure 3.10 A, B) resulting in a protein purified at homogeneity. The latter step did provide evidence for the presence of tetrameric species (β_4-HbTb) in solution, indeed β_4-HbTb was eluted in a volume range corresponding to molecular weights of human hemoglobin HbA, and significantly lower than that of myoglobin (Figure 3.10 B, right inset) used as standard for monomeric form. Once got in solution, purified apo-globin was able to react with hemin A, reconstituting the holo-protein (see below), in a homo-tetrameric state, using the protocol described in Methods section.

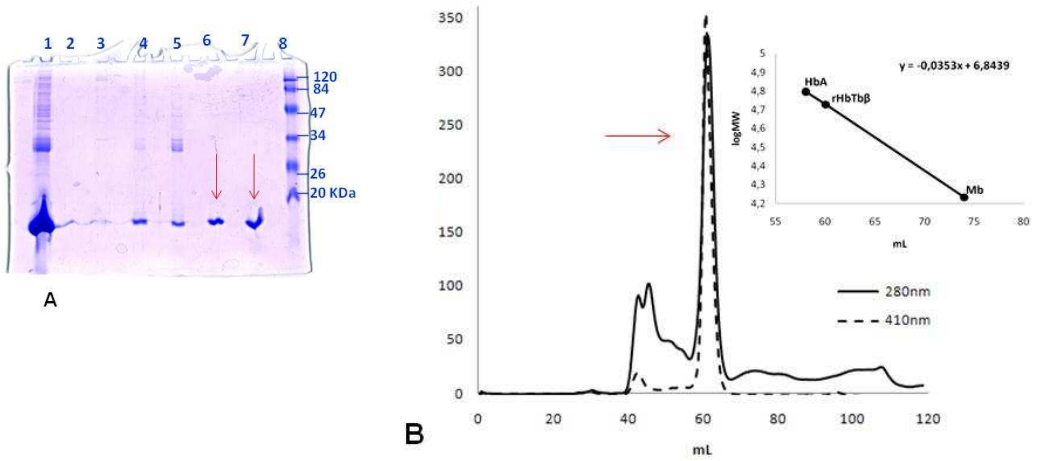

Figure 3.10: A) 12% acrylammide SDS-PAGE of β-HbTb. lane 1: fraction resolubilized with 0.2% N-lauroyl sarcosine, before of purification procedure; lane 2,3,4,5: fractions not purified; lane 6,7: fractions purified of β_4-HbTb at the end of purification procedure; lane 8: molecular weight markers. **B)** Elution profile of a β_4-HbTb sample applied to Sephadex G-75 gel filtration column. *Right inset*: Calibration curve and corresponding equation of the Sephadex G-75 column used in this purification procedure. Human hemoglobin (HbA, a tetramer) and myoglobin (Mb, a monomer) were used as markers. The red arrows indicate the position of β-HbTb.

3.1.3 Comparative spectroscopic /computational study of the β subunits of HbA and HbTb

3.1.3.1 Heme coordination of ferric and ferrous adducts

Purified β_4-HbTb has been analysed *via* optical spectroscopy (UV/VIS and CD). The oxidation pathway of β_4-HbTb, through air-exposure of protein solutions, was followed by electronic absorption spectroscopy at 20°C and pH 7. In analogy to HbITn and HbTb, the autoxidation was started from the carbomonoxy derivative and not from the oxy or the deoxy forms, since the former is more stable towards oxidation [74, 75]. This guarantees a higher reproducibility of the autoxidation process, which is much faster than that of HbA, and even faster than that of HbTb. Indeed, the autoxidation process of β_4-HbTb is practically concluded within 10 minutes, whereas the autoxidation of HbTb takes place in about 10 hours. The spectrum of the initial CO form has the usual Soret band at 420 nm and the Q bands at 540 and 570 nm (Figure 3.12 A). At the end of the autoxidation process the Q bands have moved to 535 nm and 565 nm, respectively, and the Soret band moved to 414 nm which is diagnostic of a hexacoordinate low spin (6cLS) system, assigned to a bis-histidine heme species. Repeated cycles of reduction/oxidation steps consistently reproduce the hemichrome state, showing the formation of the bis-His complex is a reversible process. CD spectra show that the bis-His is a folded state (Figure 3.11,

solid line). Moreover, CD spectra hardly change during the autoxidation process, and their features indicate that the starting carbonmonoxy form as well as the final bis-His form are fully folded (Figure 3.11).

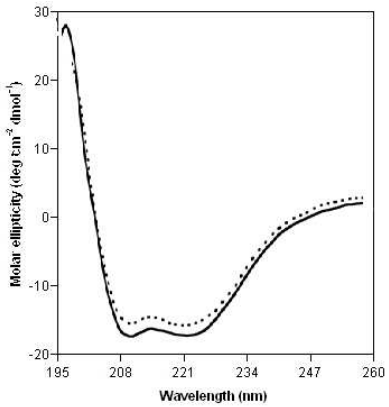

Figure 3.11: CD spectra of β_4-HbTb of the bis-His (solid line) and of the carbonmonoxy form (dashed line). Spectra were recorded in the far-ultraviolet region, at 10°C in sodium phosphate buffer 20 mM pH 7.0, with a protein concentration of 0.1 mg/mL^{-1}.

It is noteworthy that, consistently with HbTb and in contrast with Hb1Tn [74], no pentacoordinate high spin (5cHS) ferric form is apparent during the autoxidation process.

During the early stages of air-exposure (one minute), the appearance of the weak charge transfer (CT1) band at 630 nm is clearly observed in the absorption spectrum (Figure 3.12 B), suggesting that a ferric aquo 6cHS species first forms, and eventually and quantitatively evolves in the 6cLS hemichrome species, analogously to what observed *via* X-ray crystallography for the HbTb ($\alpha_2\beta_2$)at β-subunits [75]. This route differs from that observed for HbITn, whose hemichrome is formed *via* a 5c ferric intermediate [74].

For the sake of comparison with the behavior of human hemoglobin, we have also collected the UV/VIS spectra of the HbA β subunits in their tetrameric (β_4-HbA) and monomeric (β-HbA, bound to PMB) forms, at the same conditions used for β_4-HbTb. Ferric β_4-HbA and ferric-β-PMB chains were prepared by oxidation of oxy-forms with potassium ferricyanide, 4 : 1 molar excess per heme, in presence of 20% (v/v) glycerol. The addition of such proteins stabilizer was needed for preventing precipitation of proteins from solution[142].

Indeed ferric β_4-HbA and ferric-β-PMB are very unstable and rapidly tend to aggregate and to precipitate. Excess oxidizing agent was removed by gel filtration through a Sephadex G-25 column (since the ferriprotein eluted faster than the yellow excess ferricyanide, visual observations of clean separations could be made).

In agreement with previous observations by Peisach [120] and Shikama [106] we found that the isolated β-subunit and β_4-HbA are in an almost complete 6cHS aquo-met state that evolves spontaneously, though much slower than in β_4-HbTb, in a mixture of 6cLS hemichrome (a peak at 535 nm and a shoulder near 565 nm) and 6cHS aquo-met state (bands at 500 and 630 nm) (Figure 3.13), characterized by a Soret at 408 nm.

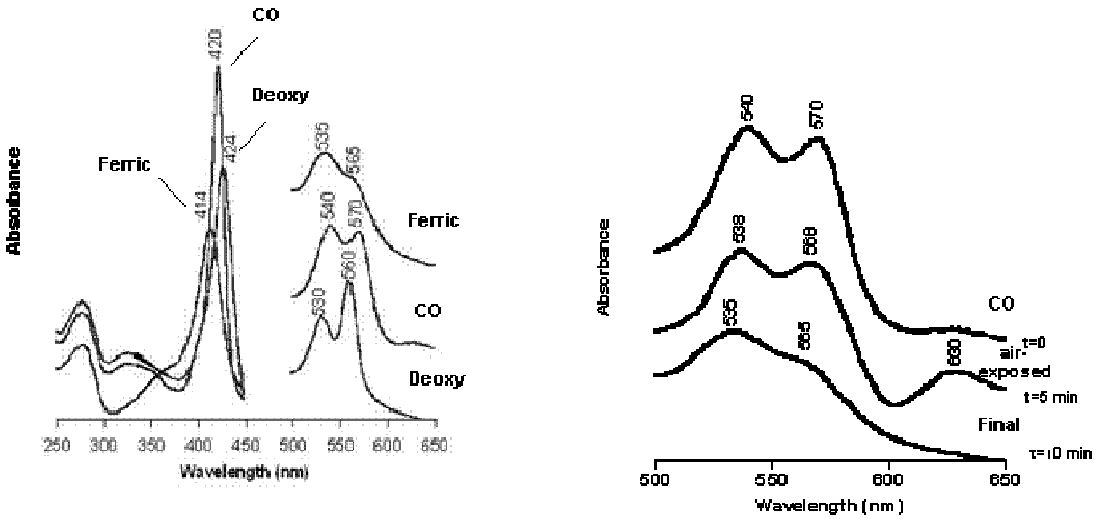

Figure 3.12: UV/VIS Spectra were recorded at room temperature in 40 mM Tris/HCl pH 7, 80 mM NaCl with a protein concentration of 0.2 mg mL^{-1}. **A**) Solution spectra of β_4-HbTb in the deoxygenated (Deoxy), carbomonoxy (CO) and ferric forms. **B**) Absorption spectra of air-exposed β_4-HbTb. Spectra were recorded after exposure of the carbomonoxy form of the protein to air at pH 7.0, as indicated. The region between 500 and 700 nm was eightfold expanded. The concentration of protein was 0.5 mg mL^{-1}.

As discussed in section 3.1.1, the crystal structure of β_4-HbA at pH 7 in the ferric form contains only 6cHS aquo-met adducts at the four hemes, with no trace of bis-histidyl adduct.

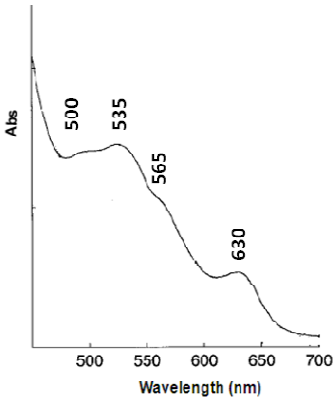

Figure 3.13: Absorption spectra of β_4-HbA oxidized with potassium ferricyanide 4 : 1 molar excess per heme. Spectra were recorded at room temperature, in 50 mM Tris-HCl pH 7.0 and 20% (v/v) of glycerol, with a protein concentration of 0.2 mg mL^{-1}.

It is worth reminding that the heterotetramer $\alpha_2\beta_2$ of ferric HbA at pH 7 are completely in an aquo-met state.
Upon reduction of the ferric β_4-HbTb, *via* addition of stoichiometric amount of sodium dithionite, a 424 nm Soret band and 560 nm Q_0 and 530 nm Q_1 bands appear, assigned to a bis-histidyl ferrous heme species, without significant traces, even at longer time, of 5cHS deoxy state (433 and 555 nm) (Figure 3.14).
On the contrary, no hemochrome was ever observed in HbTb heterotetramer [58, 75].

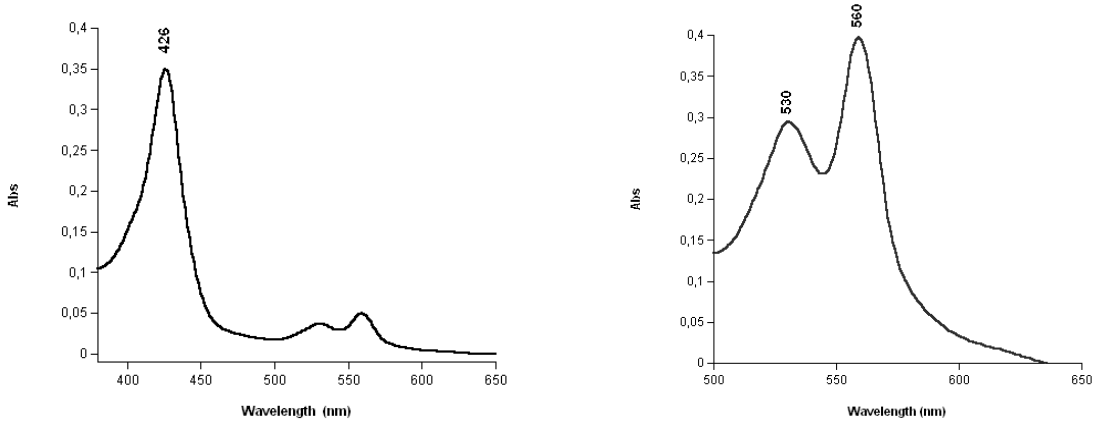

Figure 3.14:. UV/VIS spectra were recorded at room temperature in 40 mM Tris/HCl pH 7, 80 mM NaCl, with a protein concentration of 0.2 mg mL^{-1}, upon reduction of the ferric β_4-HbTb *via* addition of stoichiometric amount of sodium dithionite. *Right:* The region between 500 and 700 nm was eightfold expanded.

The behavior for HbA is more complicated (Scheme 1), since the addition of solid sodium dithionite to ferric β_4-HbA produces hemochromes that evolves to 5cHS deoxy state at longer time [120]; and reduction of ferric β_4-HbA starting from the cyano-met state [120] or photolysis of the carbomonoxy form, leads straightforwardly to deoxy penta-coordination. Indeed, the only crystal structure of deoxy β_4-HbA reveals a 5cHS state [140].

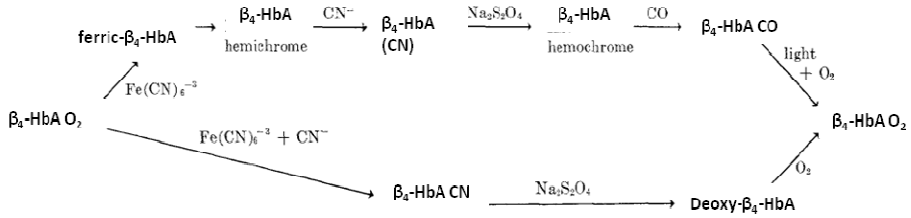

Scheme 1 Cycles oxidation / reduction of β_4-HbA (adapted from reference [120]).

3.1.3.2 Molecular dynamics simulation of β-HbTb and β-HbA isolated chains

These experimental findings show that the β chain of *Trematomus bernacchii* Hb is able to form the bis-histidyl complex both in the $\alpha_2\beta_2$ tetramer [45, 75] and in the β_4 tetramer; for β_4-HbA, under similar conditions, the 6cLS hemichrome state is much less populated and the aquo-met state is preferred (crystal structure contains only 6cHS aquo-met adducts). Since the quaternary assembly of the chains is essentially the same for the two Hbs, these data suggest that the greater propensity of the fish Hb to form the bis-hystidyl complex should be caused by an intrinsic property of the β-chain, that is partially lost in the case of HbA. In order to address this specific point, a comparative molecular dynamics (MD) study of the HbTb and HbA isolated β-chains in the hemichrome state has been carried out (in collaboration with Dr. Antonello Merlino, University of Naples "Federico II").

MD simulations with an atomistic description of the protein and solvent molecules have previously been applied to probe the stability of a protein structure [193, 194] and of protein fragments [193, 195]. In the case of globin chains, MD techniques have been also used to investigate the conformational impact of mutations, to understand the role the CD loop structure and dynamics, as well as to determine the stability of liganded forms [196-198] [58, 199]. 35 ns MD simulations of β-HbTb and β-HbA isolated subunit have been performed (see Methods for details). Several time-dependent properties of the system were analyzed to verify the stability of the MD simulations. The RMSD of the coordinates during the simulation versus the starting models as function of time is reported in Figures 3.16A and B. These plots show that a *plateau* is reached after 5000 ps for the C^{α} atoms and for all atoms of the two proteins and that the simulated structures remain close to their starting model (C^{α} RMSD is about 2 Å for β-HbTb and about 2.6 Å for β-HbA, respectively).

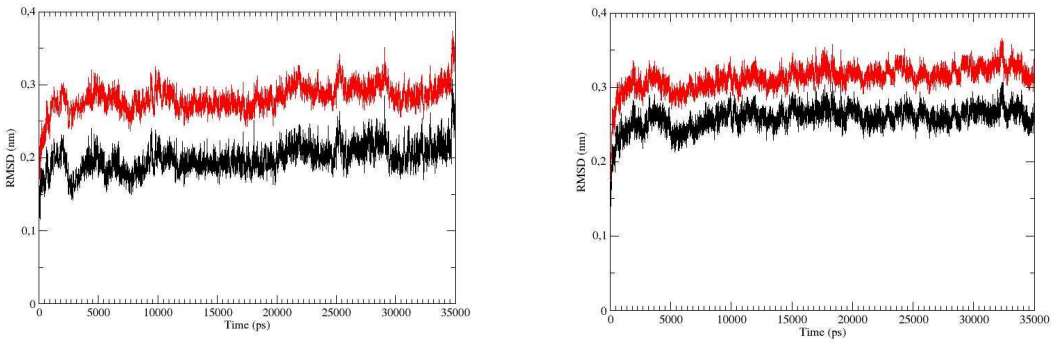

A **B**

Figure 3.16: Root mean square deviation of Cα atoms (black) and of all atoms (red) versus time. A) β-HbTb and B) β-HbA.

The time evolutions of the secondary structure elements, the total number of hydrogen bonds (Figures 3.17A and B) and the radius of gyration (Figures 3.18A and B) indicate that the two proteins maintain the correct globular folding during the simulation, thus suggesting that the presence of the bis-hystidyl complex does not affect the overall stability of the isolated HbTb β-chain and is also compatible with the sequence of β-HbA.

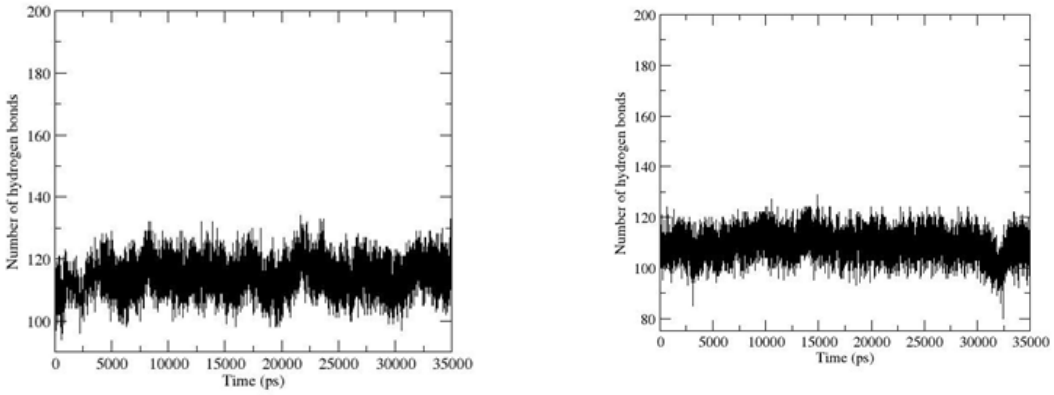

A) **B)**

Figure 3.17: Time course of the total number of hydrogen bonds of β-HbTb (A) and β-HbA (B) during the simulations.

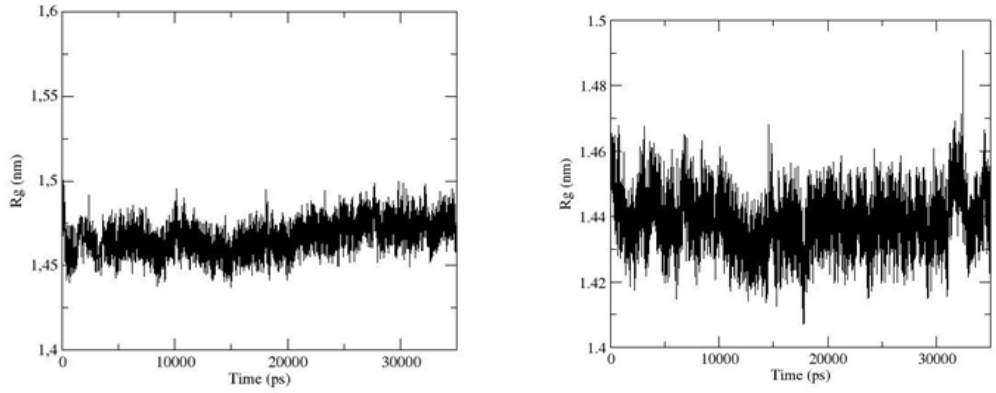

A) **B)**

Figure 3.18: Time course of radius of gyration (Rg) of β-HbTb (A) and β-HbA (B) during the simulations.

To better characterize the differences between the structure of the isolated β-HbTb chain and that within the $\alpha_2\beta_2$ tetramer, were computed the RMSD between the average conformation

obtained from the simulation and the ferric structure of HbTb derived from the Protein Data Bank, code 1S5X. The overall structure of β-HbTb closely matches the crystallographic one (RMSD= 1.69Å), thus suggesting that the isolated β-chain of HbTb is able to retain its fold in the simulated time-scale. The RMSD per residue plot shows that deviations from the starting model larger than 2.0 Å are located at the chain termini, between helices A and B residue (residues 17-22), close to the CD loop (residues 39-42 and 53-56), in the EF loop and between helices G and H (Figure 3.19).

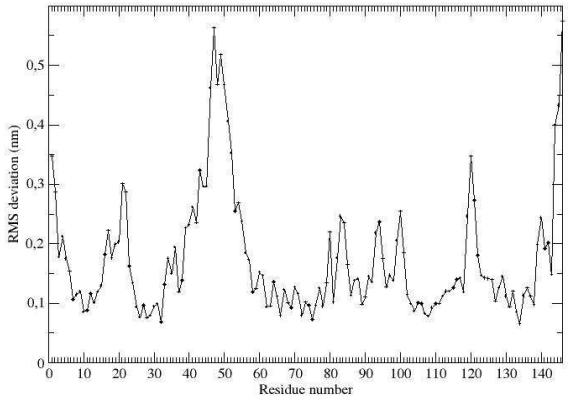

Figure 3.19: Root mean square deviations of each amino acid of β-HbTb versus the starting structure calculated from the simulation.

These data are not surprising given that the most significant differences between the corresponding structures are located on flexible loops. In conclusion, our simulated data clearly show that the presence of the bis-hystidyl complex does not affect the overall stability of the isolated HbTb β-chain.

The fluctuations of protein residues during the simulations have also been analyzed (Figure 3.20). The RMSF plot shows that the presence of the covalent bond between proximal and distal His and the heme iron strongly limits the fluctuations of E and F helices (RMSF=about 0.05 Å) in β-HbTb. On the contrary, larger fluctuations (>0.1 Å) take place at the F helix in β-HbA. It should be also noted that the CD loop region appears more mobile in β-HbTb than in β-HbA. Notably, these data well correlate with the experimental observation that CD loop of the β-chain is considerably disordered in the X-ray structure of ferric HbTb [45] and provide further support to previous results indicating a strict relationship between the structure and dynamics of CD region and that of the residues lining the heme pocket [196].

These data agree with previous findings indicating that the equilibrium between pentacoordinated and bis-histidyl state in globins is largely controlled by the structure and dynamics of the CD loop [200].

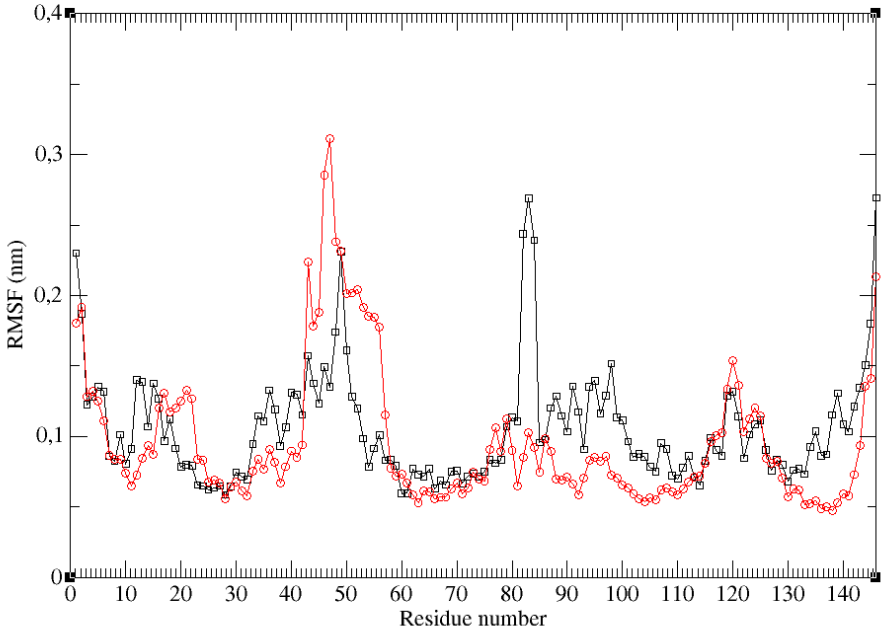

Figure 3.20: Root mean square fluctuations (RMSF) *vs* residue number of β-HbTb (red circles) and β-HbA (black squares).

3.1.3.2 Possible functional role of hemichrome: Peroxidase activity of β_4-HbTb

As a preliminary functional characterization of the ferric form of β_4-HbTb (and also of HbTb and HbA for comparison), an essay of peroxidase activity, which should be strictly sensitive to the hemichrome presence [67], was performed. Indeed, recently, has been suggested that hemichrome can be involved in the protection of the Hb molecule from peroxidation attack [201]. Peroxidase activity was measured for β_4-HbTb and HbTb at 20°C and pH 7 (phosphate buffer), according to a published procedure [67], using dopamine as substrate. Dopamine is a hydroxyquinone that can be oxidized to form the corresponding quinone and which eventually forms insoluble melanin (for details see Methods). The samples were previously oxidized by addition of ferricyanide. The data are plotted in Figure 3.21 as a function of Hb concentration.
A low peroxidase activity was measured for β_4-HbTb, 13 and 2 times lower than HbTb and HbA, respectively (at 0.3 mg/ml and pH 7 for comparison, Table 3.5).

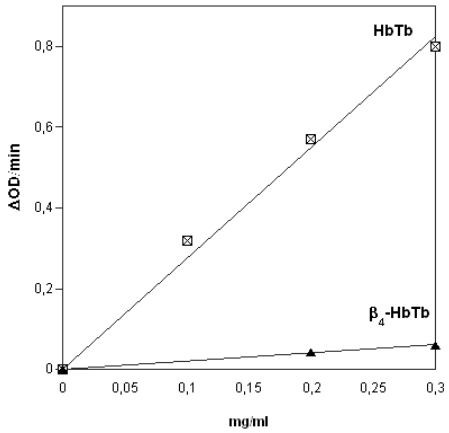

Figure 3.21: Peroxidase activity of β_4-HbTb and HbTb at pH 7, monitored by the increase in optical density at 475 nm.

Table 3.5: Peroxidase activity at [Hb]= 0.3 mg/mL of different Hbs

[Hb]=0.3mg/mL	**ΔOD/min**
HbTb	0.78850
HbA	0.11015
β_4-HbTb	0.05883

Notably, peroxidase activity of both the separate subunits of human hemoglobin are reduced with respect to the tetramer [202]. Furthermore hemichrome in isolated human α subunits complexed with the alpha-hemoglobin stabilizing protein (AHSP) does not exhibit peroxidase activity [201].

3.1.4 Comparative analysis: HbA vs HbTb

The recombinant production of HbTb β-chain has given the opportunity to carry out an integrated study on the propensity to form bis-histidyl adduct at the β-subunits of AfHbs by putting together the results of the MD simulations on the isolated chains with the experimental data on the homo- and hetero-tetramers. The results provides a deeper insight on the role of tertiary and quaternary structures on the hemichrome occurrence in AfHbs with respect to mammalian Hbs and in particular to HbA.

The protein was produced and accumulated in recombinant *E. coli* as IBs and from them recovered in almost folded state by mild detergent treatment. It is indeed now largely accepted that properly folded proteins are usual components of IBs [188, 189], confuting the consolidated idea that solubility of recombinant protein directly implies protein conformational quality [190, 191]. In solution, the purified chain was made to react with hemin A, reconstituting the holo-protein that turned out to assume a homo-tetrameric state, as demonstrated by gel-exclusion chromatography.

Previous works have indicated that major structural events associated with the hemichrome formation in Antarctic fish Hb, and presumably sub-Antarctic fish Hbs [203, 204], are a) the closure of the EFβ helices with a scissor-like motion, and b) a sliding motion of the heme out of the pocket. More precisely, in the formation of the bis-His adduct, the distance between the Cα atoms of proximal and distal His decreases from 14-14.5 Å generally observed in the canonical R and T state to 12.5 Å, whereas the heme slides out of the heme pocket of almost 1 Å.

Apart for the AfHbs, the only known example of a crystal structure that demonstrates the presence of the bis-His linkage in a tetrameric Hb, is provided by the low pH crystal form of horse Hb in the ferric state, where the hemichrome linkage occurs at the α heme iron. Although the combined scissor-like/sliding motion, observed in the hemichrome form at the β subunit of AfHbs, is mostly conserved also for the α-chain of the horse Hb, in this case the crystal packing contacts appear to play an important role in the stabilization of the large modifications observed at the CD corner and associated with the formation of the distal histidine linkage. On the other hand, for AfHbs there is a clear correlation between the propensity to form a bis-histidine adduct in the isolated chain and in the homo- and hetero-tetrameric form both in solution and in the crystal structure. Therefore, the AfHbs represent an interesting structural model for studying the molecular determinants of bis-histidyl coordination in a globin-like folding.

Electronic spectroscopy of β_4-HbTb has shown that it readily and quantitatively forms a hemichrome state. Recalling that in the $\alpha_2\beta_2$-HbTb heterotetramer the β subunits also oxidize to a bis-His state, we can confidently conclude that the chain, independently of the aggregation state, β_4-HbTb is prone to form a bis-His complex. The MD simulations data indicates that the bis-histidyl complex in β-HbTb retains the folded globin structure, suggesting that this state could be accessible also for the isolated monomeric chain as well. Altogether, these data suggest that HbTb β-chain has an intrinsic propensity to the endogenous hexa-coordination. In particular, the finding that the carbomonoxy derivative of the β-chain is endowed with an intrinsically high flexibility [61] may well play a role in favouring the EF rearrangement that is necessary for the formation of the bis-His complex. As a result, in the latter derivative the r.m.s. fluctuation of the EF region is considerably low. In this context, of particular interest is the parallel simulation performed on the β-chain of HbA; the results indicate that the hemichrome state is also accessible to the isolated β-chain of HbA. However, in comparison to β-HbTb, the CD region displays a significantly less

pronounced mobility. This result is somewhat expected, as the occurrence of localized regions with different intrinsic flexibility is a common observation in comparative studies between meso- and psychrophilic proteins, and it is related to cold-adaptation [205]. On the contrary, in the MD simulation of the human β-chain, the E helix and the FG corner display a larger fluctuation, which could have a role in the decreased relative stability of the bis-His adduct with respect to exogenous ligation. This different behaviour can be correlated to some critical substitutions at the EF region.
In HbTb, the hydroxyl group of Tyr85(F2)β (Phe in HbA) forms two H-bonds with the oxygen carbonyl atom of Gly70β and the N atom of Gly74β; this produces a break of the 5-1 hydrogen bond between these two residues of the E helix and causes the helix to kink [45]; thus the Tyr acts as a wedge that facilitates the movement of the distal His positioned on the N-terminal side of the E helix and also decreases the mobility of the F helix. The absence of these interactions in the human chain may well justify the higher fluctuation of the region and adversately affects the stability of the bis-His adduct with respect to the aquo-met derivative. In addition, the mutation of Ala70β for Gly in HbTb also favours the sliding of the heme group.
The higher propensity to form hemichrome in AfHbs with respect to HbA can also be due to quaternary structure elements, namely related to the $\alpha_2\beta_2$ hetero-assembly. Indeed, the crystal structures of HbTb and HbITn revealed that hemichrome is allocated in an R/T intermediate quaternary structure [108]. The major regions responsible for the stability of this quaternary structure are the $\alpha_1\beta_2$ ($\alpha_2\beta_1$) and $\beta_1\beta_2$ interfaces. This study strongly suggests that quaternary structure is able to affect the bis-His coordination in ferrous HbTb. Indeed, the heterotetramer of HbTb never forms hemochrome [57, 75], whereas the subunits in the β_4 state do exhibit the bis-His coordination in the ferrous state. This evidence suggests that in HbTb the T quaternary state [57] is too rigid to assist the scissor-like closure necessary for the endogenous coordination. The evidence of an incompatibility of endogenous coordination within the T-state also matches with the observation that HbTb in the ferric state within a T quaternary structure does not host the bis-His coordination but a penta-coordinated ferric state at the β subunits [67].
Our study also supports the mechanicistic evidence that hemichrome forms *via* an aquo-met intermediate [75]. Therefore, the mechanism seems not to be affected by the different aggregation state (β_4 or $\alpha_2\beta_2$).
The comparative analysis with β_4-HbA and with heterotetrameric HbA provides a more general perspective of our findings. Not only β_4-HbA exhibits, in solution, a propensity to form hemichrome lower than β_4-HbTb (about 50 vs 100 %in solution while in the crystal structure is fuon only the aquo-met coordination), but also the presence of the α subunits in HbA heterotetramer further depresses the conversion of the partner β-chain from aquo-met to the hemichrome state, whereas in HbTb the α subunits does not significantly affect the intrinsic ability of the β subunit to form the hemichrome coordination.

The determination of the three-dimensional structure of ferric β_4-HbTb or the hybrid α_2-HbA/β_2-HbTb could expand our understanding of this different behaviour.
The absence of a peroxidase activity of β_4-HbTb, has two relevant consequences. 1) First it supports a recent hypothesis that the functional role of bis-His coordination is to protect from the peroxidase attack. 2) Secondly, the negligible peroxidase activity in β_4-Hb*Tb* in comparison with that measured for AfHbs [67] indicates that in going from a homotetramer with all the hemes in the hemichrome state to the heterotetramer with only the two α -chains in the usual aquo-met state, the reactivity with H_2O_2 significantly changes. We speculate that, in the heterotetramer the reaction of H_2O_2 starts at the α heme (in the aquomet state), and, *via* heme-heme communication, at the β-chains the breakage of the bis-His coordination occurs, thus producing a strongly reacting species, i.e. the ferric 5C, frequently observed in AfHbs [67, 74]. Furthermore, the high peroxidase activity and the hemichrome presence in AfHbs would make a sense for Antarctic fish, living at -2 °C with a high oxygen concentration (e.g. high oxidative stress), and with a high mitochondrial density in the slow muscle fibers [206].
In Table 3.5 was summarized the comparison between the coordination states of HbA and HbTb $\alpha_2\beta_2$ heterotetramer and corresponding β_4 homotetramers in the ferrous and ferric state.

Table 3.6 Comparison between the coordination state of HbA and HbTb $\alpha_2\beta_2$ heterotetramer and corresponding β_4 homotetramers, in the ferrous and ferric state.

	Homo sapiens		*Trematomus bernacchii*	
	$\alpha_2\beta_2$-HbA	**β_4-HbA**	**$\alpha_2\beta_2$-HbTb**	**β_4-HbTb**
Deoxy state	5C-HS	mixture 5C-HS/6C-LS	5C-HS	6C-LS
Ferric state	**6C-HS**	**mixture 6C-HS/6C-LS (solution) 6C-HS (crystal)**	**α_2(6C-HS)/ β_2(6C-LS)**	**6C-LS**

(6C, hexa-coordination; 5C, penta-coordination; LS, Low Spin; HS, High Spin).

3.2 Crystallographic /spectroscopic study of hemichrome formation in Hb from Antarctic and sub-Antarctic fish.

In order to complete an extensive crystallographic study previously undertaken within of group work of Prof. Mazzarella (Biostructure Group of Naples), aimed at detailed characterization of the bis-histidine complex formation in a tetrameric Hb, the study of the crystals structure of the component principal of Antarctic fish *Trematomus newnesi* (HbITn) at high-resolution (1.65 Å) oxidized with potassium ferricyanide (ox-HbITn) was made.
Finally, together with the aim of obtaining insights into to understand the structural basis of the formation of bis-His adducts in Hbs, a study by microResonance Raman

on single crystals, of Hb from sub-Antarctic fish *Eleginops maclovinus*, in the deoxygenated, carbomonoxy and ferric forms, was performed
Below are discussed separately the results obtained.

3.2.1 Crystal structure of Hb from *Trematomus newnesi* oxidized by ferricyanide

Previous studies on the oxidation pathway of the carbomonoxy form of HbITn (PDB code 1T1N [207]) at several times of air exposure: a) three hours air exposure in solution [74], b) seven days exposure in solution [43], c) thirdy days (1m-HbITn) and one year air-exposed (1y-HbITn) in the crystal state (unpublished) offered a clear observation that, in Hbs from Antarctic fish, α and β chains follow distinct but interdependent oxidation pathway. Interestingly, in 3h-HbITn structure, corresponding to three hours of air exposure, the heme is oxidized with two visible states of coordination (a pentacoordinated β-iron with high-occupancy, and a water molecule at low-occupancy), a molecule of CO is still bound to Fe (II) at the α-heme (PDB code 3D1K, [74]). Increasing the time of air exposition (seven days, referred to as 7d-HbITn, PDB code 1LA6), in α-subunit the iron is oxidated and coordinates a water molecule. At the β-heme the distal histidine occupies the apical sixth coordination of the metal (hemichrome, with a binding length His63β-Fe^{3+} of 2.0 Å) [43]. This process is associated with the change of quaternary structure that passes from R to an intermediate structure between R and T (H), that remains at longer times (when the form hemichrome occurs). Alternativily other coordination has been observed, or with a His63β-Fe^{3+} distance unusually long 2.9 Å (thirdy days), or even with mixture of bis-histidyl and penta-coordinated states (in which distal histidine shifts out of the heme pocket) (Figure 3.22).
The complexity of the coordination states observed form the X-ray structures at different times of air-exposure has a spectroscopic (resonance Raman) counterpart. Indeed, at long time the air-exposure in solution produces a mixture of high-spin (aquo-met and penta-coordinated) and low-spin (bis-histidyl) ferric adducts [74].
The interpretation of such multiple binding modes (related to multiple sequential and/or serial oxidation reactions) requires a systematic crystallographic study, where the different coordination states must be well characterized. In order to simplify the chemical systems ferric HbITn species oxidized by ferricyanide has been crystallized in the Biostructure Group. This crystal structure should be unambiguously assigned to a completely ferric, giving a simplified picture of the chemical composition. The complete oxidation by ferricyanide would provide a homogeneous distribution in solution of the crystallizing molecule, and consistently a reduced number of iron coordination.
Diffraction data were previously collected in-house at 100K. Detailed statistics on data collection are reported in Table 3.7. During this thesis, diffraction data at 1.65 Å resolution have been analyzed, refining a structure that represents the first reference of a completely ferric HbITn structure (ox-HbITn).

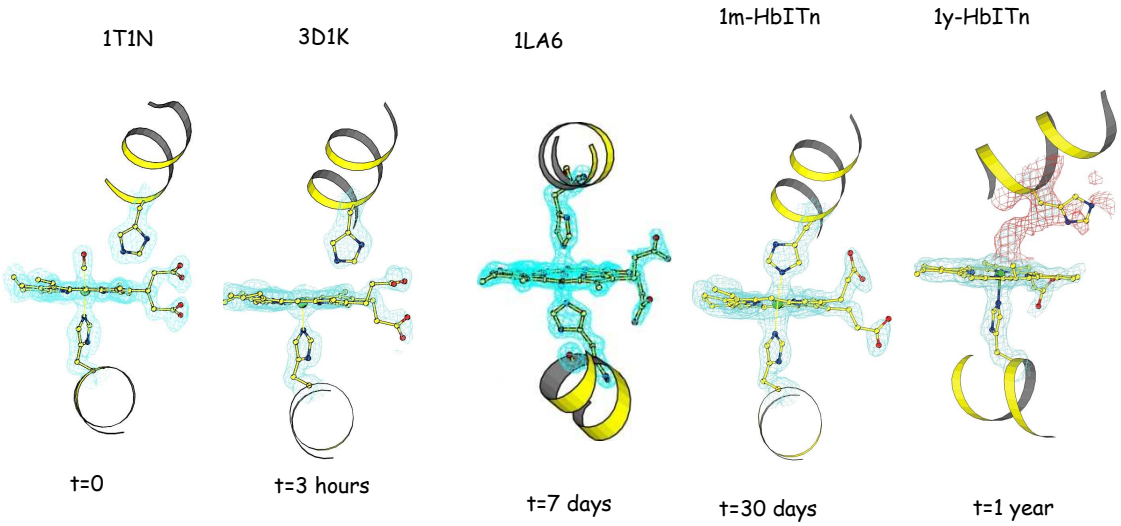

Figure 3.22: Electron density maps (contoured at 2.5 σ) corresponding to the β-heme regions of carbomonoxy form of HbITn (PDB code 1T1N) and of intermediate oxidation (previously determined at several times of air exposure).

Table 3.7: X-ray data collection statistics for ox-HbITn.

Space group	C2
a (Å)	88.513
b (Å)	87.230
c (Å)	55.536
α (°)	90.00
β (°)	98.080
γ (°)	90.00
Resolution limits (Å)	50.00-1.65
No. of observations	49800
Completeness (%)	99.4 (98)
I/σ(I)	19.6 (4.5)
Average multiplicity	5.2
Rmerge (%)	5.6

R_{merge} = $\Sigma_{hkl}\Sigma_i$ |Ii(hkl)-<Ii(hkl)>|/ $\Sigma_{hkl}\Sigma_i$ Ii(hkl), where Ii(hkl) is i_{th} intensity measurement of the reflection hkl, including symmetry related reflections, and <Ii(hkl)> is its average. Values in brackets are for the highest resolution shell.

The structure of ox-HbITn was solved by molecular replacement using the program AMoRE [181] and a previous structure partially oxidized of HbITn (PDB code 1LA6)[43] as a starting model. The refinement was performed using the program SHELX [146]. The refinement runs were followed by manual intervention using the molecular graphic program O [147], to correct minor errors in the position of the side chains. Water molecules were identified by evaluating the shape of the electron density

and the distance of potential hydrogen bond donors and acceptors. The structure of ox-HbITn was refined to an R_{factor} of 21% (R_{free} 26%) by using diffraction data (49.800 reflections) in the resolution range 50.0–1.65 Å. The model, a this level of refinement, includes 198 water molecules and nine residues modeled in alternative conformations (Ser21α, Leu29α, Ser72α, Glu83α, Glu87α, Ser9β, Met18β, Asp72β, Met78β). The electron density is well defined for both the main chain and the side chains of most of the residues. As frequently reported in R state Hbs [43], the regions corresponding to the CD loop (residues 43–53) are completely disordered.

The inspection of the electron density maps clearly indicates that the binding state of the heme iron of α and β chains is different. Indeed the α-heme iron is hexa-coordinated with a spherical density assignable to a water molecule bound to the sixth coordination position of the heme iron at distance of 2.1. Å (Figure 3.22a). A completely different picture emerges from the analysis of the electron density maps corresponding to the β-heme (Figure 3.22b). The β-heme shows a well ordered single coordination, confirming the goodness of the strategy and of the chemical protocol used (addition of ferricyanide). Indeed, the iron coordinates both the proximal (92β) and the distal (63β) histidine residues, forming a complex bis-histidine. No traces of aquomet or pentacoordinated ferric species is observed at the β heme. That indicates that the crystallization from the oxidized solution (containing the three species aquo-met, penta-coordinated and bis-His adducts) selected only two coordination, whereas the Hb ferric form containing the 5C adducts did not co-crystallize.

This structure provides the chance to definitively record the structural features associated to the only ferric bis-His adduct at the β hemes. Hemichrome formation at β-hemes group is characterized of AfHbs produces relevant modifications of the position of and the helices Eβ and Fβ [43]. In ox-HbITn structure, the hemichrome formation in the β subunit of HbITn is associated with a significant modification of the pocket in which the heme group is located.

The comparison of such structure with the other oxidation intermediates, reported in Figure 3.22, may shed light on the chemical and structural oxidation pathway of HbITn. The overall structure of ox-HbITn is very similar to those of intermediates of oxidation. Indeed, the RMSD based on the Cα atoms between 3h-Hb1Tn [74], 1LA6 [43] and, 1m-HbITn, were 0.36 Å and 0.45 Å, and 0.28 Å, respectively, indicating that these structures display the hemichrome quaternary structure but different tertiary structure, at level of heme regions.

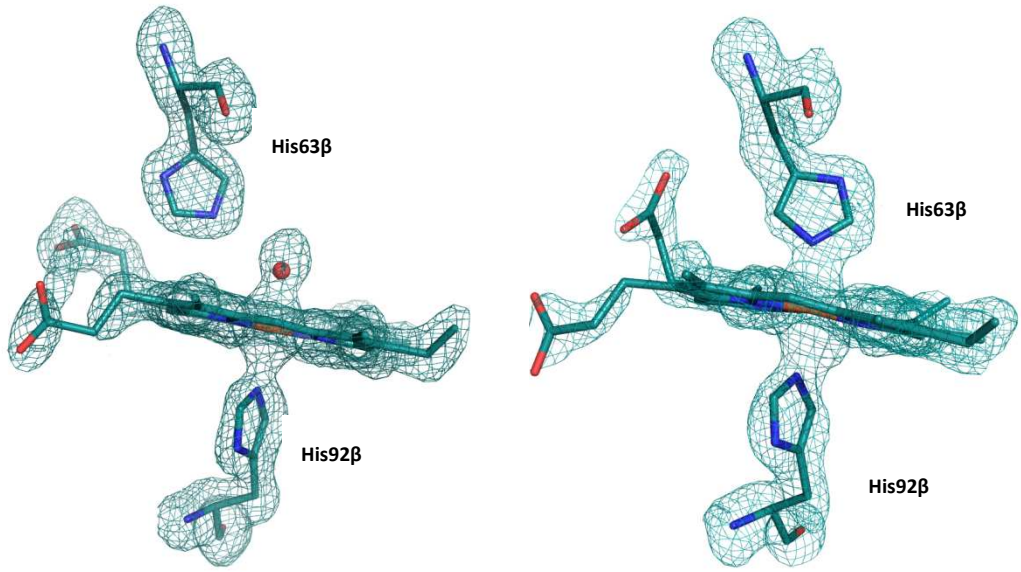

a) **b)**

Figure 3.23: Electron density maps (contoured at 2.5 σ) corresponding to the α (a) and β (b) heme regions of ox-HbITn.

A quantitative evaluation of the entity of the scissors-like motion of the EF segment may be provided by the analysis of the distance between the C^{α} atoms of the proximal and the distal histidine residues, which belong to helix F and E, respectively. This distance, which is almost invariantly close to 14.5 Å (± 0.2) in α and β-chains of Hb structures extracted from different organisms and in a variety of liganded states, is as low as 12.6 Å in the β subunit of ox-HbITn, similar to the value of the bis-His in 1LA6 structure (12.4 Å) [43], but different from the values reported for 3h-HbITn (13.9 Å)[74] and 1y-HbITn (13.1 Å) (unpublished).
In conclusion, the high-resolution data and the chemical oxidation by potassium ferricyanide, allowed a more reliable characterization of the heme stereochemistry in HbITn. Ox-HbITn is a model for decoupling the density of bis-His coordination from alternative structures (penta- and hexa-coordinated species) at heme groups, particularly interesting for future investigations of Raman-assisted crystallography.

3.2.2 microRaman study of single crystals of Hb from *Eleginops maclovinus*

Eleginops maclovinus is a member of non-Antarctic notothenioid species, belonging to the family *Eleginopidae* and is the only species of its genus. It is an important component of the ichthyofauna in the coastal temperate and sub-Antarctic waters of South America, adapted to 278–288 K; it is also found in coastal waters around the Falkland Islands [208].

The blood of *E. maclovinus* shows one cathodal (HbCEm, accounting for 25%) and two anodal components (Hb1Em and Hb2Em, accounting for 70 and 5%, respectively) [144].
We studied the major component Hb1Em, a tetrameric Hb that displays the Root effect. Sequence alignments show a significant similarity to high-Antarctic fish Hbs. Indeed, Hb1Em shares 85% sequence identity to HbTb.
Initial screenings for Hb1Em in the carbomonoxy form (Hb1EmCO) crystallization were conducted in dialysis buttons using the ammonium sulfate solutions that yielded crystals of the major Hb component of *T. newnesi* [207]. 10 ml protein solution at 20 mg/ml in 100 mM Tris–HCl buffer pH 8.0 and 2 mM sodium dithionite was dialyzed against a 25 ml reservoir containing 2 M ammonium sulfate, 100 mM Tris–HCl pH 8.0 and 2 mM sodium dithionite. The quality of the crystals was then improved by fine-tuning the sulfate concentration. The best crystals were obtained in a week using 20 mg/ml Hb1Em and 1.8 M ammonium sulfate. In the same flask, different dialysis buttons contained crystals displaying two different morphologies, that have called Ortho and Hexa crystals (rod-like and bipyramidal, respectively). The maximum dimensions of Ortho crystals (rod-like morphology) were 0.05 x 0.05 x 0.4 mm, whereas those of the Hexa crystals (bipyramidal morphology), were 0.1 x 0.1 x 0.2 mm.
Resonant Raman (RR) microscopy experiments were conducted on Hb1EmCO crystals (both Ortho and Hexa) as well as on their ferric and deoxy forms.
RR spectroscopy represents an important investigative tool to characterize hemoproteins [74, 209]. The RR phenomenon, for which the intensity of some Raman-active vibrations increases of several orders of magnitude, can occur when wavelength of the exciting laser is within the heme electronic absorption bands, in particular in the Soret band or in the α, β bands (see Methods for further details).
Upon Soret excitation, the RR spectrum in the high frequency region from about 1300 to 1700 cm^{-1}, *core size* region, consists of in-plane porphyrin vibrations (Figure 3.24). These bands are sensitive to the electron density of the macrocycle and the oxidation, coordination and spin state of the iron ion [210].

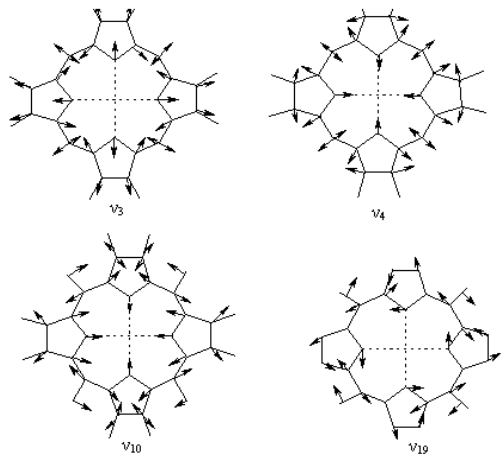

Figure 3.24: Main vibrational normal modes in the high-frequency region (*core size*) of porphyrin ring [210].

To assign the Raman spectroscopic markers of hemoglobins analysed in this thesis, were used the assignement, both oxidation state and the spin state of iron ion, as reported in literature for linked hemoglobin [211] (Table 3.8) and for various systems: myoglobin and hemoglobin in the oxidized form linked to the fluoride ion ($Mb^{III}F$ and $Hb^{III}F$, respectively), myoglobin in the deoxygenated form (Mb^{II}) and the model system [210, 212-214].

Table 3.8: Core size marker bands (excitation wavelength: 514.5 nm) for hemoglobin in different bound, spin and oxidation states [211]

Molecule	Oxidation state	Spin state	*Marker* Oxidation state (cm^{-1})		*Marker* Spin state (cm^{-1})		*Marker* Oxidation and Spin state (cm^{-1})	
			ν_4	ν_{11}	ν_{19}	ν_2	ν_3	ν_{10}
metHbCN	Fe(III)	LS	1374	1564	1588	1583	1508	1640
metHbF	Fe(III)	HS	1373	1565	1555	1565	1482	1608
deossi Hb	Fe(II)	HS	1358	1546	1552	1565	1473	1607
HbO_2	Fe(II)	LS	1377	1564	1586	1582	1506	1640

(LS, Low Spin; HS, High Spin,; dp, depolarized band; p, polarized band; ap, anomalous polarized band).

High frequency Resonant Raman spectra of Hb1Em crystals of the Ortho and Hexa forms together with those of the corresponding ferric and deoxy forms obtained with 514.5 nm excitation are shown in Figure 3.27.
The ferric form contains a hexa-coordinated low-spin hemichrome with bands at 1505, 1h559, 1588 and 1640 cm^{-1} assigned to ν_3, ν_{38}, ν_{19} and ν_{10} modes, respectively (Figure 3.26, Hexa crystal), as previously observed in HbTb crystals [216].

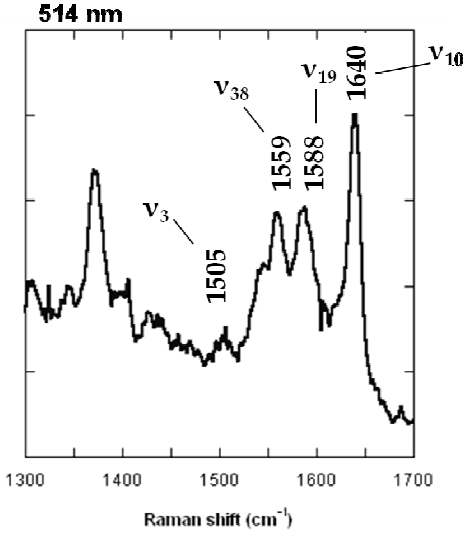

Figure 3.26: RR spectrum for Hexa crystals of Hb1Em in ferric form, in 100 mM Tris–HCl buffer pH 8.0 at room temperature. Bands diagnostic of hemichrome are evidenced.

The deoxy forms of both Ortho and Hexa are penta-coordinated high-spin states (ν_4, ν_{19}, ν_{37} and ν_{10} at 1355, 1548–1549, 1582 and 1602–1607 cm^{-1}, respectively). However, after long laser exposure times (about 10 min), the Ortho but not the Hexa form appears to be unstable under laser irradiation, since it irreversibly converts to a hexa-coordinated low-spin hemochrome state (hemo, with ν_4, ν_3 and ν_{19} at 1361, 1496 and 1587 cm^{-1}, respectively). Even at low laser power (0.1 mW), the degree of photolysis of both carbomonoxy forms of Hb1Em was high, as was apparent from the relative intensity of the ν_4 bands of the CO and photolyzed species (1374 and 1355 cm^{-1}, respectively) and the presence of bands arising from ν_{19} and ν_{10} of both the deoxy form and the CO complex (deoxy bands at 1548–1549 and 1602–1607 cm^{-1}, respectively).
Raman microscopy, as previously demonstrated [123, 216, 217], is a valuable tool for the preliminary investigation of protein single crystals. Indeed, apart from the different stability in the laser beam, no significant difference was observed using Hb1Em is the first sub-Antarctic fish Hb to be crystallized. Raman spectroscopy and the spectra of Hb1Em (Hexa and Ortho) in the carbomonoxy, deoxy and ferric forms are indistinguishable within the experimental noise.

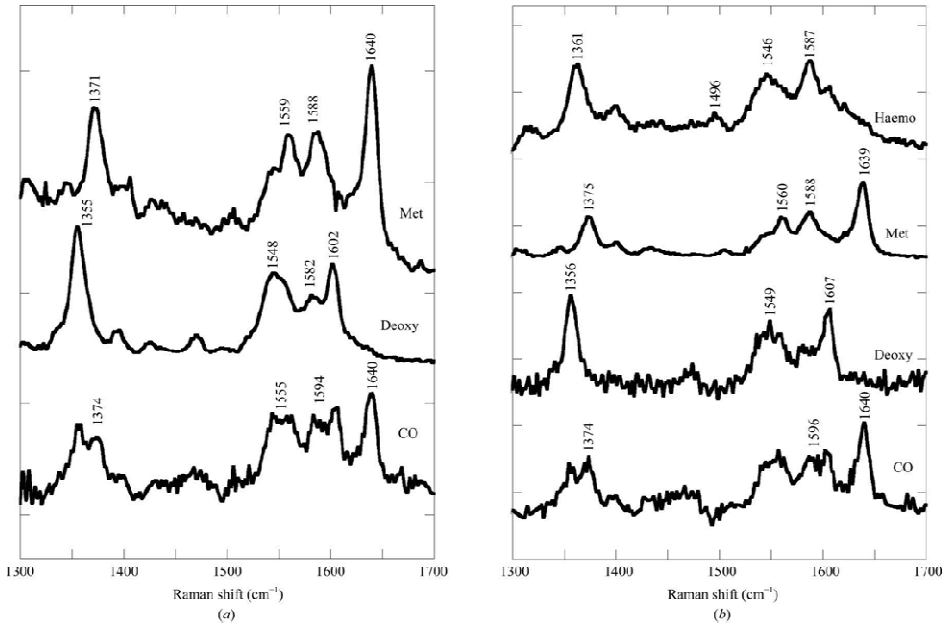

Figure 3.26: Resonance Raman spectra of crystals of Hb1Em in 100 mM Tris–HCl buffer pH 8.0 at room temperature in the carbomonoxy (CO), deoxygenated (Deoxy) and ferric (Met) forms for Hexa (a) and Ortho (b) crystals. The Ortho deoxygenated form (b) converts quickly into hemochrome (hemo) after 10 min laser exposure. Excitation wavelength, 514.5 nm; laser power at the sample, 2 mW for the ferric and deoxy forms and 0.1 mW for the carbomonoxy form. All spectra were an average of at least six spectra with 2 min integration time [215]

Chapter 4

Role of the tertiary and quaternary structure in the modulation of the Root effect

The Root-effect Hb isolated from the Antarctic fish *Trematomus bernacchii* (HbTb) has been used in pioneering investigation on the structural basis of the Root effect [53, 57, 63] and constitutes an optimal model for studies of allostery in proteins. Comparison of the deoxygenated crystal structures of HbTb at two different pHs, 6.2 and 8.4, shows that the most significant differences are localized at the CDα region, (suggested to be involved in the allosteric transition of mammalian Hbs [13, 72]), where a salt bridge between Asp48 and His55 breaks during the low-to-high pH transition [57]. Therefore these structures, characterized by the same quaternary structure, but some subtle changes in tertiary structure, offer the possibility to investigate the influence of the tertiary structure of the exogenous ligands binding to the heme group [20].
In this context HbTb crystals in T-state, at two different pHs, are excellent starting points for planning binding experiments by crystallographic /microspectroscopics studies.
In order to delucidate the role of the tertiary and quaternary structure in the modulation of Root effect, the work strategy was divided into two fields of investigation:
1) equilibrium and crystallographic studies of oxygen (O_2)and carbon monoxide (CO) binding to the T-state HbTb crystals at pH 6.2 and 8.4.
2) combined crystallographic (X-ray diffraction)/ Resonance Raman (RR) microspectroscopic study on the mechanism of nitric oxide (NO) binding and release to the T-state HbTb crystals at two different pHs.

4.1.1 Equilibrium studies of O_2 binding to the T-state HbTb crystals

In collaboration with Prof. Andrea Mozzarelli at University of Parma was performed the oxygen equilibrium study at HbTb crystals in T-state at two different pHs.
Use of crystals for binding studies (analogously to the case of silica gel encapsulation) allows to separate the changes of quaternary structure (locked by the crystalline matrix) from those of the tertiary structure that occur following the exogenous ligand binding. In order to obtain crystals of Hb in T-state linked to any ligand, it is necessary to act with care of the experimental conditions. In fact, although the crystal packing restricts the degree of conformational flexibility of the macromolecule, it is not sufficient to prevent the transition between the two states quaternary T and R, which commonly occurs as a result of the binding event. For this reason, in order to determine oxygen binding curves at HbTb crystals in the T-state at pH 6.2 and 8.4, the

drops containing crystals are treated with a solution which has the same pH and concentration of the same buffer, but at a higher concentration (up to 30%) of polyethylene glycol (PEG), which further stabilizes T-state, avoiding the breakage of crystal as a result of binding (Figure 4.1).

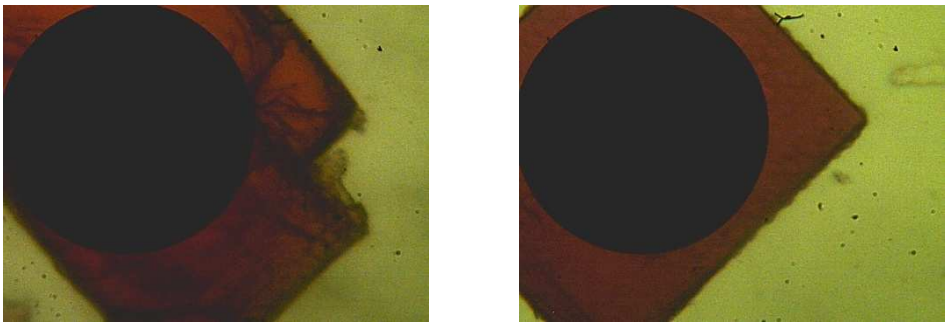

Figure 4.1: Deoxygenated HbTb crystals, at pH 8.4, during experiments of oxygen binding curves in stabilizing solution containing *left*) 15% anaerobic PEG 6000, *right*) 30% anaerobic PEG 6000.

Oxygen binding curves of HbTb single crystals were determined by measuring polarized absorption spectra, between 450-700 nm, as a function of oxygen pressure (between 7.4 and ~742 torr). The spectra were collected with a microspectrophotometer UV-Vis in two directions of extinction, defined as maximum (//M) and minimum (//m) absorption. The spectra for single crystal at pH 8.4 are presented in Figure 4.2.
The crystals binds reversibly oxygen. In particular: the crystal at pH 6.0, even at 100% of O_2 pressure, is not completely saturated, while at pH 8.4 is completely saturated.
The estimation of the fraction of saturation was determined from reference spectra [154] obtained on other crystals at pH 6.0 and pH 8.4 in deoxygenated and oxy forms, and calculating the ratio between the absorbance at 575 nm and 555 nm at the same pH. The contribution of trace amounts of hemoglobin in the ferric form has been removed from the spectrum recorded after long air exposure in the absence of reducing agent.

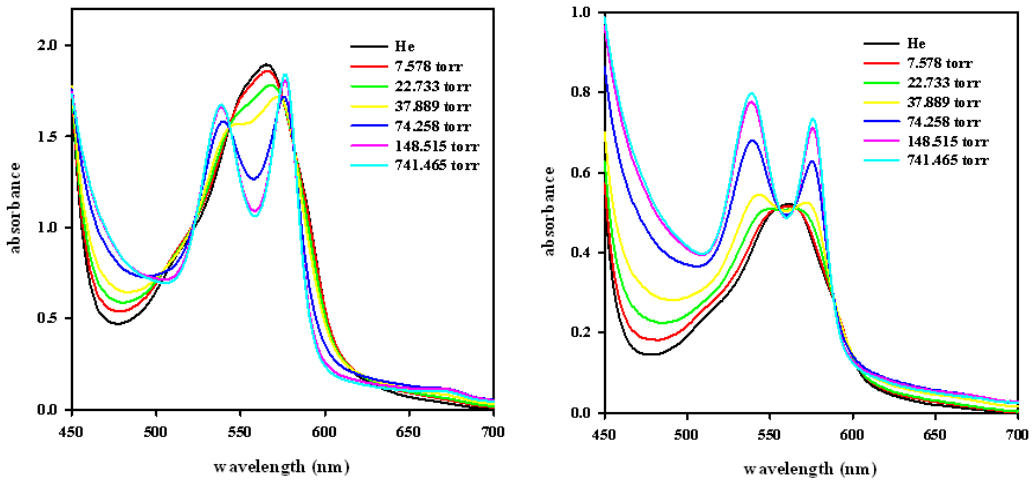

Figure 4.2: Polarized absorption spectra of HbTb single crystal in the T-state at pH 8.4 at increasing oxygen pressure, between 7.4 and ~742 torr (30% PEG 6000, 50 mM Tris /HCl pH 8.4, 100 mM KCl, 2.5mM sodium ascorbate and 4000 units/ml catalase) in two directions of extinction defined as maximum (// M) and minimum (//m) absorption.

The Hill plots of the fractional saturation, in two directions of extinction for HbTb single crystals are shown in Figures 4.3 and 4.4, at pH 8.4 and 6.2, respectively. Crystals grown at low pH have shown an average p50 of 98.3 ±7.4 torr and a Hill coefficient very close to unity, indicating no cooperativity in oxygen binding within the T-state, in agreement with the prediction of the MWC model [1]. Crystals grown at high pH, instead, have shown an average p50 of 64.7 ±3.4 torr and surprisingly a Hill coefficient of 1.49, indicating that about half of the cooperativity is retained in crystals grown at pH 8.4.

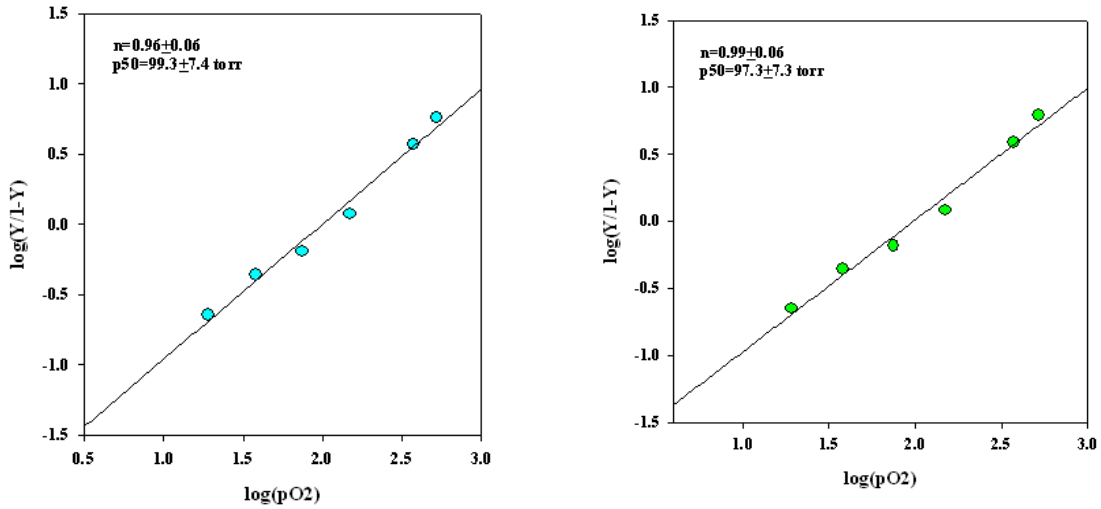

Figure 4.3: The Hill plots of the oxygen binding curves for HbTb single crystal in T-state at pH 6.2, in two directions of extinction defined: *left)* maximum (// M) and *right*) minimum (//m) absorption.

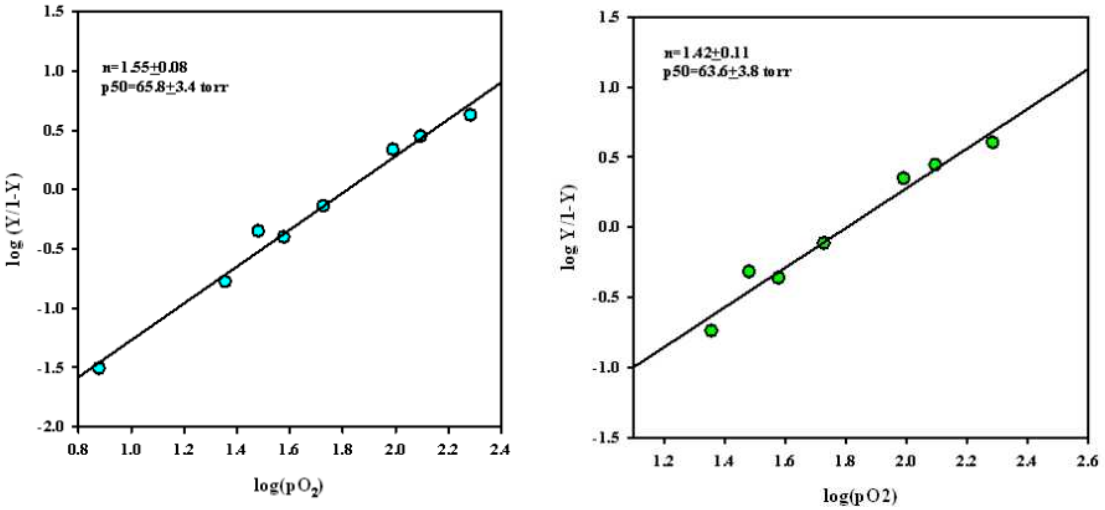

Figure 4.4: The Hill plots of the oxygen binding curves for HbTb single crystal in T-state at pH 8.4, in two directions of extinction defined: *left)* maximum (// M) and *right*) minimum (//m) absorption.

This functional study shows that the low -to- high pH transition induces 2-3 fold increase in oxygen affinity, highlighting that the Root effect is still present in T state Hb, even if strongly reduced with respect to solution (where oxygen affinity decrease about 100-fold between pH 8.5 and 6.5 [53]). These findings are consistent with a greater tension of the crystal structure of deoxygenated HbTb at pH 6 than that at pH 8. Possible sites of such a tension are, both $\alpha_1\beta_2$ interface (strong interaction between

Asp95α and Asp101β) and the CDα corner (strong salt bridges His55α-Asp48α). Based on the available structures, it can be assumed that the difference in oxygen affinity in HbTb lies mainly on the α-chains, because on the β-chains the structural difference of the deoxygenated forms at the two pHs is minimal. Therefore, our functional data are interpreted assuming that the increase of pH, in deoxy-HbTb at pH 8, α-and β-chains follow different paths of oxygenation, with the α-subunit that binds more strongly compared to pH 6. Changes in the affinity within the quaternary T and R state are provided from the recent "tertiary two-state (TTS) allosteric" model for Hb [218, 219]. The TTS model assumes that both T and R quaternary states are populated by two tertiary states, *t* and *r*, endowed, respectively, with a low and a high oxygen affinity and ligand-binding rates that are independent of the overall quaternary state of the tetramer.

Based on this model, in HbTb, the α-chains tend to be predominantly in a *r* tertiary structure (that is relaxed as R quaternary state), while the β-chains maintain the tertiary structure *t*. This observation thus suggests a marked heterogeneity among the α- and β-subunits.

Furthermore the evidence of the role of the tertiary structure in oxygen binding affinity exhibited by HbTb at different pHs is supported, very recently, by computational studies performed in the laboratory where this thesis has been conducted [199]. These studies highlight that a pH decrease induces the oxygen release from HbTb in a process that involves a conformational change in the protein tertiary structure at level of CDα region, affecting the O_2 access to heme pocket. In particular, the profile of free energy of O_2 binding at the α-subunit of deoxygenated HbTb at pH 6 and 8 (2.6 kcal / mol lower at pH 8, Figure 4.5) is consistent with a factor of 2-3 higher affinity for HbTb at pH 8 related to pH 6 [199]. This computational study provides a theoretical explanation for the different affinity for O_2, but it tells us nothing about the appearing cooperativity of deoxy HbTb crystals at pH 8.4. A crystallographic study was addressed to have some clues.

4.1.2 Crystallographic study of CO binding to the T-state crystals of HbTb at basic pH

Oxygen binding study to deoxygenated HbTb crystals has shown, besides the effect of pH on the oxygen affinity, that about half of the cooperativity present in solution is retained in crystals grown at basic pH, but not at pH 6. This indicates that the cooperativity can be elegantly switched on by the only changes in tertiary structure, at quaternary structure blocked (by the crystalline matrix).

In order to identify the structural reasons for this functional feature we attempted to crystallize the T-state carbomonoxy form of HbTb at pH 8.4 (referred as to HbTb8CO).

Carrying out the CO binding reaction, and crystal manipulation, under aerobic conditions is complicated by the tendency of deoxy-hemoglobin crystals to disorder or oxidize in the presence of oxygen [220]. Furthermore, the work was difficult for the

inability to operate experimentally with CO cylinders, during crystal handling and and during the collection of X-ray diffraction data.
Deoxy-HbTb single crystals were soaked, for various hours, with a deoxygenated / CO saturated stabilizing solution, containing 30% PEG 6000, 100 mM Tris/HCl at pH 8.4, 200 mM potassium chloride, 2 mM dithionite reducing agent and flushed of gaseous CO, before data collection. Diffraction data from HbTb8CO, at the resolution of 2.2 Å, were collected in-house at 100K by fast transfer into CO saturated stabilizing solution, containing 30% PEG 6000, to prevent the breakup of the crystal as a result of binding [221], and 14% glycerol as cryoprotectant.
All the data were indexed, processed and scaled with HKL2000 [145]. Detailed statistics on data collection are reported in Table 4.1. Matthews coefficient [150] calculation suggested the presence of one tetramer in the asymmetric unit. An analysis of the unit cell parameters, show that HbTb8CO is not strictly isomorphous with respect to the starting crystal: CO binding involves an expansion of 10 Å of b axis (from 94.63 Å in deoxygenated form to 104.72 Å). An analysis of the collected diffraction data shows, similar to the starting deoxygenated crystal [57], that the crystal present pseudo-merohedral twinning. The twin fraction for HbTb8CO, determined by the algorithm implemented in the program SHELX, [146] is 0.30.
The structure of deoxygenated HbTb at pH 8.4 (PDB code 2H8D) [57] was used as starting model in the refinement, which was carried out by using the program SHELX, [146]. The overall position of the tetramer was initially refined by rigid body minimization. The R_{factor} of this model was 29.8% in the resolution shell of 10–2.2 Å.

Table 4.1: X-ray data collection statistics for HbTb8CO

Crystal data	
Space group	$P2_1$
Unit-cell parameters	
a (Å)	61.57
b (Å)	104.72
c (Å)	61.63
α (°)	90.00
β (°)	90.28
γ (°)	90.00
Data processing	
Resolution limits (Å)	50.00 - 2.20
No. of observations	860323
No. of unique reflections	110132
Completeness (%)	91.5 (91.2)
Average multiplicity	2.9 (2.8)
Rmerge (%)	0.085 (0.56)

*R*merge = $\Sigma hkl \Sigma_i |I_i(hkl) - \langle I_i(hkl) \rangle| / \Sigma hkl \Sigma_i I_i(hkl)$, where $I_i(hkl)$ is ith intensity measurement of the reflection hkl, including symmetry related reflections, and $\langle I_i(hkl) \rangle$ is its average. Values in brackets are for the highest resolution shell.

The partially refined structure of HbTb8CO, R_{factor} of 0.25 and a R_{free} of 0.30, shows only a partial CO binding due to oxidative phenomena, that are very fast in HbTb [75].
Indeed |Fo-Fc| electron density maps, corresponding to the heme regions, showed that a CO molecule was bound to the heme iron in the α-chains, whereas β-chains are characterized by the contraction of the heme pocket, typical of the formation of a bis-histidine complex (Figure 4.6).

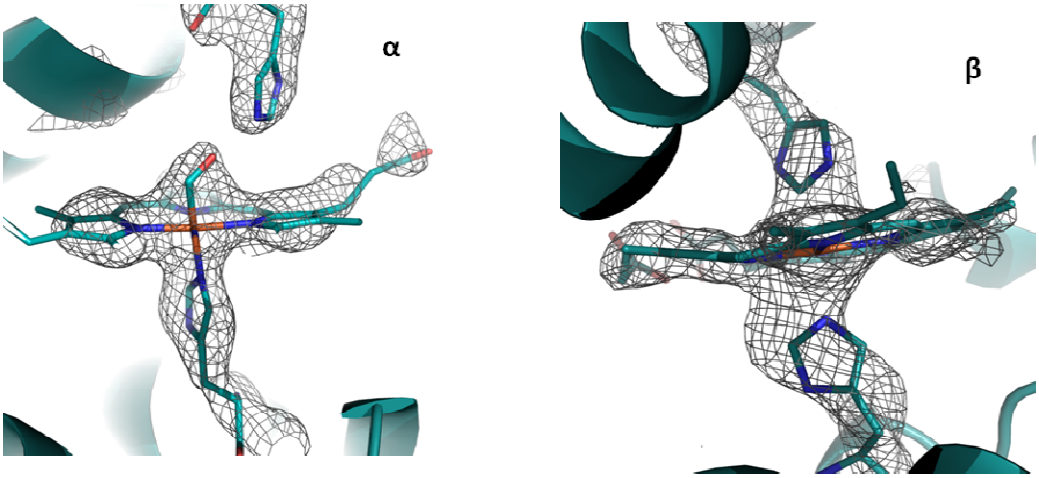

Figure 4.6: Omit |Fo-Fc | electron density maps (contoured at 3.0 σ) of HbTb8-CO for α-heme and β-heme.

Table 4.2 reports the comparison of the Cα-Cα distances for the four subunits of partial HbTb8CO and the corresponding starting deoxygenated structure (HbTb8). The distance between the C^{α} atoms of the proximal and the distal histidine residues provides a quantitative evaluation of the entity of this scissors-like motion of the EF segment, associated at the formation of the bis-histidyl adduct [45]. Indeed, in HbTb the β subunit undergoes to an oxidation with a contraction of the heme volume. The partial oxidation, an undesired event, makes the interpretation of our data more difficult.

Table 4.2: Cα-Cα distance of the proximal and the distal histidine residues for partial HbTb8CO and HbTb8

Cα-Cα Distance (Å)		
	HbTb8CO (partially)	HbTb8
α_1	14.2	14.1
α_2	13.8	14.2
β_1	12.6	14.1
β_2	13.2	14.0

To evaluate in HbTb8CO structure an eventual transition T → R due to binding, an analysis of difference distance matrices (DDM) were performed. DDM analysis, that has frequently been used to analyze structural transitions of tetrameric Hbs [44, 222, 223], were computed by using the program DDMP (http://www.csb.yale.edu/ userguides/ datamanip/ ddmp/ dmp_descrip.html) for the structures of HbTb8CO, HbTb8 (deoxy) and HbTb-R(CO).
As a reference, in Figure 4.7 DDM between HbTb8 (deoxy) and HbTb-R(CO) related to T → R transition is reported.

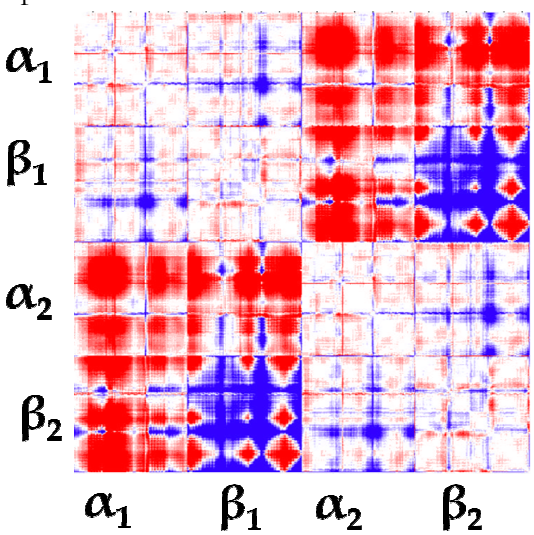

Figure 4.7: Difference distance matrices of T → R transition: HbTb8 (T state) *vs* HbTb-R(CO). Blue regions represent residues that move closer in the second structure, whereas the converse happens in the red regions. The color range extends from -2.0 Å (dark red) to 2.0 Å (dark blue).

As expected, the greatest variation of distances between Cα pairs are found for residues at the $\alpha_1\beta_2$ and $\alpha_2\beta_1$ interfaces (red regions).
The DDM between the deoxy- and carbomonoxy-HbTb and HbTb8CO structure are shown in Figure 4.8.
A comparative analysis of the analogies of the diagrams reported in Figures 4.7 and 4.8 (A and B) clearly indicates that the events linked to the ligand binding at the α heme and the partial formation of the bishistidine complex at the β heme generate some of the structural alterations induced by the T → R transition.
In particular the quaternary structure of HbTb8CO is "T-like", because DDM of HbTb8CO vs HbTb-R(CO) (Figure 4.8 B) shows a type of structural variation (color code) in the same direction of T → R transition.
These data, though perturbed by the partial oxidation, indicate that no quaternary structure modification occurs upon binding in the T-state, and that all the effect is at the level of tertiary structure.

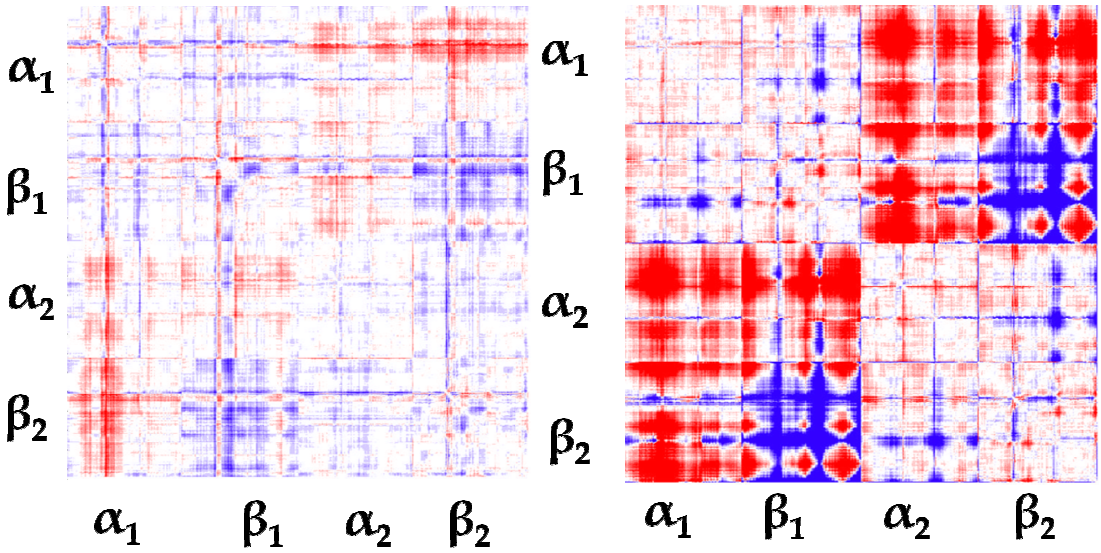

A **B**

Figure 4.8: Difference distance matrices of (A) HbTb8 *vs* HbTb8CO; (B) HbTb8CO *vs* HbTb-R(CO). The color range extends from -2.0 Å (dark red) to 2.0 Å (dark blue).

Attempts to obtain a fully CO form in a T-state HbTb structure at pH 8.4 that could completely explain the origin of cooperativity, failed. Some clue on the possible regions that are responsible for such a high modification of the heme upon binding at the T state can be indirectly extracted by an other study of this thesis, NO reactivity studies to T-state HbTb crystals.

4.2 Combined X-ray crystallography / Resonance Raman (RR) microspectroscopic study on the mechanism of NO binding and release to T-state HbTb crystals

The diffusion of NO generated *in situ* inside the crystal is more or less rapid depending on various factors, including physical and chemical properties of the solution and crystal. Clearly, the kinetics of the binding reaction cannot be followed with ordinary procedures through X-ray crystallography. A methodological approach to the study of biochemical reactions in the crystalline phase is the simultaneous combination of crystallographic and microspectroscopic techniques, available in many lines of synchrotron radiation. A micro-spectroscopic technique recently successfully applied to assist crystallography is the Raman spectroscopy [224]. In particular at synchrotron ESRF (France, 2007) and SLS (Switzerland, 2010) *in situ* experiments can be made, in which the crystallographic study is combined with Raman spectroscopy [225].

In this thesis combined crystallographic/RR micro-spectroscopic studies were perfomed in-house and at the PXII beam line of swiss SLS. Approach in-house consisted of an experiment *ex situ* crystallographic / spectroscopic (on physically distant tools), from which we have obtained structural and kinetic information on the reaction of nitrosylation of HbTb. In particular, we studied the NO binding to deoxygenated HbTb crystal at two different pH values (6.2 and 8.4), using micro-Resonance Raman spectrometry (RR).

4.2.1 Determination of nitrosylation protocol and evidence of Oxidative Denitrosylation in HbTb crystals

In literature the protocols for nitrosylation of hemoproteins are different; some of them are reported in Table 4.3. In summary, the nitrosyl crystals, from deoxygenated form, can be prepared in two ways: a) by the gas of interest flowing at a controlled concentration or, b) by generating *in situ* using NO-donor compounds. The nitrosylation of HbTb provides a twofold complication. The high oxidation tendency of HbTb in deoxygenated form when exposed to air [44, 75], and the rapid release of NO from iron-nitrosyl-hemoglobin by oxidative denitrosylation [226-228], imply that the deoxygenated and nitrosyl-crystals must be constantly kept in a glove nitrogen box, making, in fact, the procedure a) impractical. Therefore, we followed the procedure "b" for which the stabilizing solution is enriched with two precursors of nitric oxide: sodium nitrite (NO_2^{-}) and sodium dithionite ($S_2O_4^{2-}$).
Following Raman spectroscopic markers (for assignment of bands see section 3.2.2), was developed a soaking protocol (time and concentration of precursors) to obtain HbTb crystals in the nitrosylated form.
For the composition of the solution used for the nitrosylation of the crystals refer to Methods section.

Table 4.3: List of PDB codes and soaking conditions of nitrosyl hemoproteins

Year Publication PDB	PDB Code	Soaking Condtions
1999	1CL6	NO gas
1999	1CMJ	NO gas
1999	1CMN	NO gas
1999	1DP8	DEA/NONOate
2000	1DW2	nitrite/ dithionite
2000	1FOO	nitrite/dithionite
2000	1FOP	nitrite/ dithionite
1994	1GDL	NO gas
1997	1HJT	NO gas
2002	1J02	dithionite /NOC-12
1998	1JDO	NO gas
2001	1KOI	NO gas
2003	1NPF	nitrite/ dithionite
2003	1OZL	nitrite/ dithionite
2003	1OZW	nitrite/ dithionite
2003	1P3U	nitrite/ dithionite
2003	1RPS	NO gas
2003	1RQ4	NO gas
2003	1RQA	NO gas
2004	1SXW	NO gas
2004	1SXX	NO gas
1998	1BUW	NO gas

Year Publication PDB	PDB Code	Soaking Condtions
2004	1SY1	NO gas
2004	1SY3	NO gas
2004	1WOX	NOC-12
2004	1X8N	NO gas
2004	1X8O	NO gas
2004	1XK3	nitrite/ dithionite
2004	1Y21	NO gas
2005	1YWB	NO gas
2006	2E3A	NOC-12
2005	2FBZ	citrulline/dithionite
2005	2FC1	citrulline/dithionite
2005	2FC2	citrulline/ dithionite
2006	2FRJ	nitrite/ dithionite
2006	2FRK	NO gas
2006	2GHH	nitrite/dithionite
2006	2GHC	nitrite/ dithionite
2006	2NX0	DEA/NONOate
2006	2NRM	S-nitrosocysteine
2006	2O0C	SNAP (S-nitroso-N-acetylpenicillamine)
2009	3HSP	NO gas
2011	3RGP	DEA/NONOate

4.2.1.1 micro Resonance Raman spectroscopy studies on HbTb crystals

Initially, the soaking process NO on deoxygenated HbTb crystals at pH 6.2 and 8.4 have been monitored in-house *via* Raman microscopy exciting at 514 nm, using degassed solutions and reducing environment.

Nitrosyl formation was monitored following the intensity of Raman bands exchanging from values typical of the high-spin deoxygenated form (ν_4 1355 cm^{-1}, ν_{10} 1605 cm^{-1}, Figure 4.9) [229] to the low-spin nitrosyl form (ν_4 1370 cm^{-1}, ν_2 1505 cm^{-1} and ν_{10} 1635 cm^{-1}) [104].

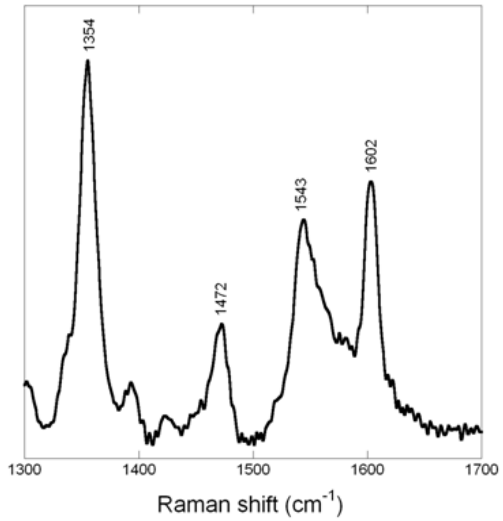

Figure 4.9: Resonance Raman spectrum of HbTb single crystals in the deoxygenated form, at pH 6.2

The processes observed by the addition of the precursors were essentially two: rapid formation (2-5 minutes) of the nitrosyl species and subsequent oxidative denitrosylation with the formation of low-spin hemichrome [45] species (Figure 4.10), which terminates in about 15 minutes.

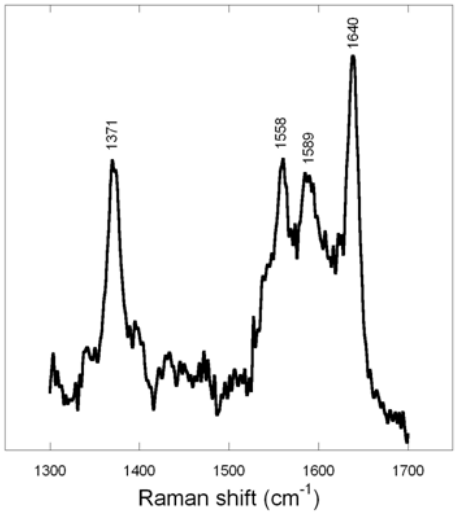

Figure 4.10: Resonance Raman spectrum of HbTb single crystals in the ferric form , at pH 8.4, after 60 minutes of air exposure. For assignment of bands see section 3.2.2. Excitation line: 514 nm.

The results obtained in these conditions showed that it was possible to obtain nitrosyl-HbTb, although yields are low (at most 70%). However subsequently at the nitrosylation, HbTb crystals, inevitably exposed to air, underwent partial oxidation, which reduced the presence in solution of nitrosyl form in favor of the oxidized (metHb) in times ranging from 15 to 20 minutes. With these conditions, which seemed quite satisfactory, two X-ray data collection at 100 K (see par. 4.2.1.3) were collected on nitrosyl-HbTb crystals, trying to minimize the air-exposure time before flash freezing of crystals. However, the examination of electron density maps clearly shows the phenomenon, both pH 6.2 and 8.4, of a partial oxidative denitrosylation (see par. 4.2.1.3).

To limit this oxidation process, although the dithionite to ensure an environment oxygen free, were subsequently amended the conditions of soaking, introducing sodium ascorbate and liver bovine catalase. Ascorbate selectively reduced the Fe(III) regenerating the deoxygenated form that can bind NO. The addition of catalase, an enzyme belonging to class of oxidoreductases, it is necessary for the elimination of reactive oxygen species produced by oxidation of ascorbic acid.

The micro-Raman study on HbTb crystals performed in these conditions, shows that the relative kinetic of the two processes, oxidation and nitrosylation, makes it potentially possible to obtain the complete form nitrosylated in T-state. Notwithstanding, repeated experiments have shown that it is not always achieved a yield of 100% of nitrosylation, the latter fact is no higher than 70% using only the precursors nitrite and dithionite and is instead between 70 and 100% adding ascorbate and catalase. Figures 4.11 and 4.12 show the RR spectra recorded on crystals, in two different pH conditions.

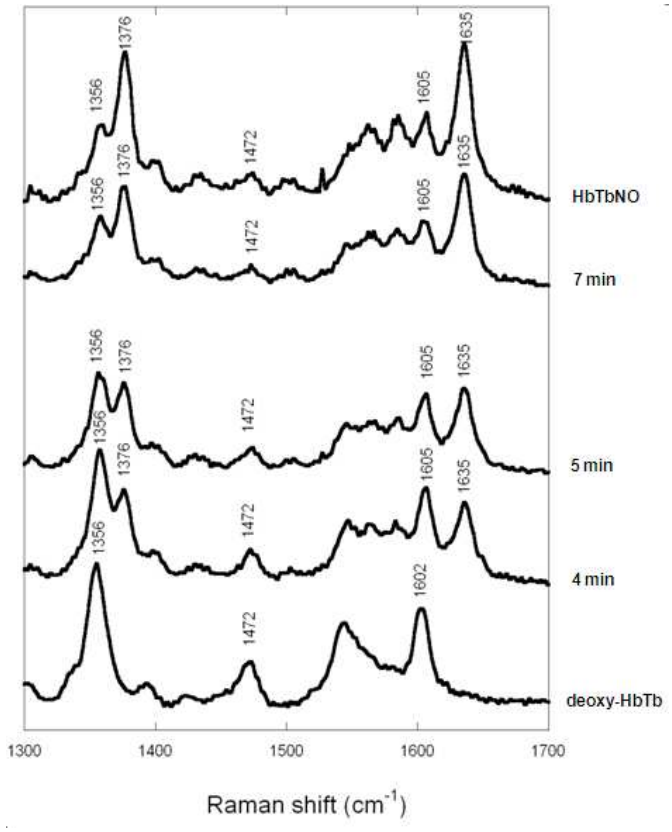

Figure 4.11: RR spectra of HbTb crystals at pH 8.4 at different times of soaking the beginning of NO. Concentration of precursors: 20 mM nitrite; 30 mM dithionite, ascorbate 5 mM, 4000 U / mL catalase. Excitation wavelength: 514 nm. Exposure time 600 s, spectral resolution 4 cm^{-1}.

Fully nitrosylated form was obtained for HbTb crystal in T-state at pH 6 (Figure 4.12). The best conditions are 30 mM sodium dithionite, 20 mM sodium nitrite, 5 mM ascorbate and 4000 U / mL liver bovine catalase, with about 10 minutes soaking time. Soaking experiments have been highly producible, once degassed solutions and reducing environment were used.
The ν_{10} value of 1635 cm^{-1} strongly supports the evidence of a hexa-coordinated Hb, since no bands (or content lower than 10 %) of the penta-coordinated, whose ν_{10} was reported to 1640 cm^{-1}, is observed [104]. The six-coordination is in line with the results obtained from Hb of carp [104] (see par. 4.2.1.2).

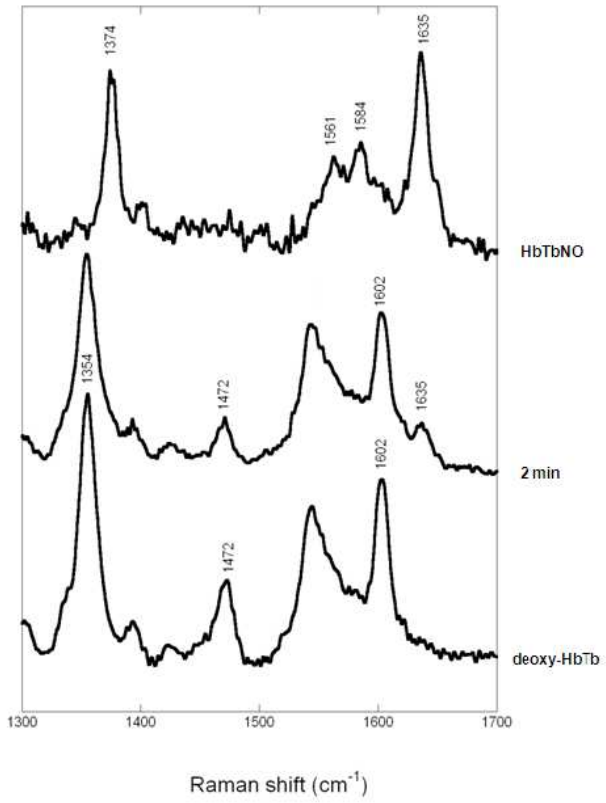

Figure 4.12: RR spectra at several steps of NO soaking into HbTb deoxygenated crystal at pH 6.0. The kinetics of binding in this case is very rapid and the yield is practically 100%. Concentration of precursors: 20 mM nitrite, 30 mM dithionite, 5 mM ascorbate and 4000 U / mL liver bovine catalase. Excitation line is 514 nm (2mW at the sample), exposure time 600 s. Spectral resolution 4 cm^{-1}.

4.2.1.2 microResonance Raman study in solution

The microspectroscopic study to HbTb crystals has been accompanied by a study in solution. In this case, in order to maintain the bound structure in T-state, ATP was added to the solution [204] in a 6:1 stoichiometric ratio with the heme group. In particular, the use of the powerful allosteric effector concentration was 6 mM ATP. The strategy of preparing nitrosyl HbTb in the form T is as follows: at a solution with a concentration of 3 mM in heme, were added to the precursor of nitric oxide, nitrite and dithionite 30 and 60 mM, respectively. The spectrum recorded after a few minutes (Figure 4.13), shows a single band ν_{10} to 1635 cm^{-1}, due to low-spin ferrous species hexa-coordinated, HbNO. The lack of ν_{10} bands around 1605 cm^{-1} and ν_4 around 1354 cm^{-1} indicate the total absence in solution of deoxygenated form, while the absence of ν_{10} band around 1640 cm^{-1} values exclude, however, the presence of ferric species.

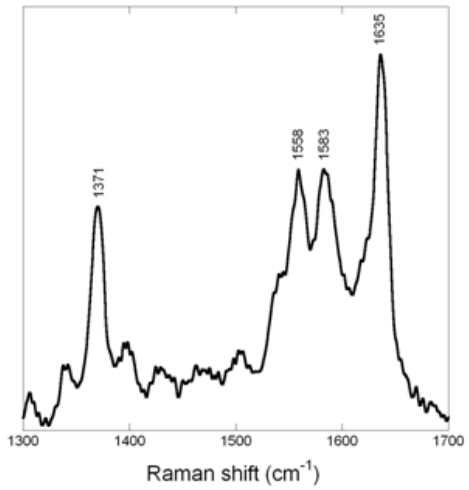

Figure 4.13: Resonance Raman spectrum of nitrosyl-HbTb solution, in T-state, at pH 8**.**

In solution, the behavior of NO binding to HbTb is different than that of human hemoglobin (HbA). The RR spectrum of the nitrosyl-HbA in solution, in the form R, presents the band ν_{10} at 1633 cm^{-1}, assigned to the NO-bound form hexacoordinated (6c) [230]. The addition at this solution of the powerful allosteric effector inositol hexa-phosphate (IHP), involves the shifts of the equilibrium toward the bound form T and a significant variation of the RR spectrum. RR spectra show the appearance of another band at 1643 cm^{-1} and the simultaneous decrease in the intensity of that at 1633 cm^{-1}, as can be seen in Figure 4.14 [231]. This second band is due to NO-related species penta-coordinate (5c), confirmed by a crystallographic study [100] (see Introduction).

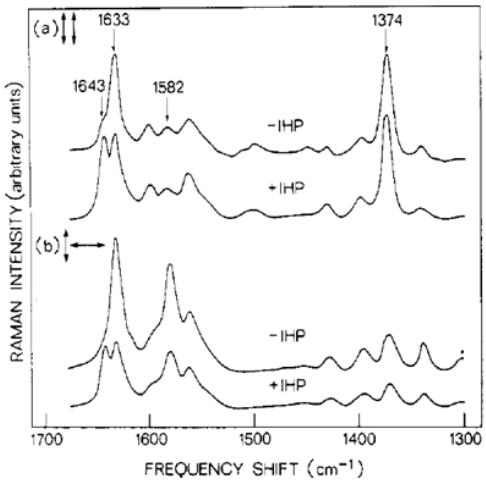

Figure 4.14: Polarized (a) and depolarized (b) RR spectra of the nitrosyl-HbA in the absence and presence of IHP [231]. Excitation wavelength: 514.5 nm.

Our work on HbTb solution, even in the case of carp Hb, the RR spectrum of its nitrosyl-form in T-state (after the transition R → T for IHP addition) due to addition allosteric shows no splitting of the band ν_{10} (Figure 4.15) [104].

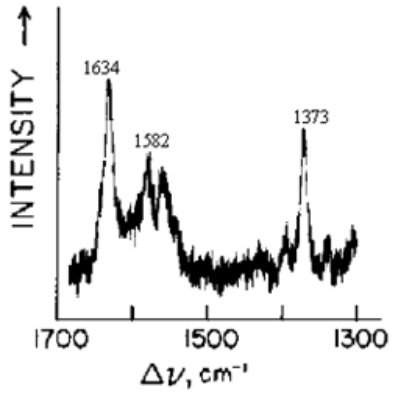

Figure 4.15: RR spectrum of carp Hb with IHP [104].

Table 4.4 shows the most relevant bands that characterize the RR spectra, in solution, of nitrosylated form of HbA and carp Hb in the absence (R state) and presence (T state) of IHP [230] and HbTb in T-state (results of this thesis).

Table 4.4: Raman shift (cm^{-1}) of nitrosyl human hemoglobin, Hb carp (T and R state) and HbTb in T state.

	HbA-NO		HbNO (carp)		HbTbNO
	T	**R**	**T**	**R**	**T**
ν_4	1373	1375	1373	1373	1375
ν_3	1500	1498	1501	1499	1498
ν_{11}	1563	1561	1561	1560	1558
ν_{19}	1584	1582	1583	1583	1583
ν_2	1581	1580	1582	1580	1584
ν_{10}	1633(6c)	1633	1634	1632	1635
ν_{10}	1644(5c)				

4.2.1.3 Crystallographic studies on HbTb nitrosylated and partially oxidized

On nitrosyl-HbTb crystals at pH 6 and 8, obtained by fast soaking of deoxygenated crystals with a stabilizing solution containing 30 mM dithionite and 15mM nitrite precursors (in absence of ascorbate and catalase) using the protocol described above (par 4.2.1.1) two X-ray high-resolution data collections were performed. In particular the diffraction data were collected, at 100 K and using 22% glycerol as cryoprotectant, a) in-house at 1.9 Å resolution, for crystals at pH 8.4 (HbTb8NO) and b) at synchrotron ELETTRA (Trieste) at 1.5 Å resolution, for crystals at pH 6.2 (HbTb6NO). The HbTb8NO crystals resulted to be highly isomorphous to those of HbTb6NO. An analysis of the collected diffraction data shows that the crystals present pseudo-merohedral twinning. This finding is in line with the previous results of Mazzarella et al. for deoxy-HbTb crystals [57]. The twin fractions for HbTb8NO and HbTb6NO, determined by the algorithm implemented in the program SHELX [146], are 0.36 and 0.32, respectively. These values together with the high resolution still allow a highly significant refinement of the two models. All the data were indexed, processed and scaled with HKL2000 [145]. Detailed statistics on data collection are reported in Table 4.5. Matthews coefficient [150] calculation suggested, for both structures, the presence of one tetramer in the asymmetric unit.

The structures were solved by the method of Fourier difference. Indeed, since the isomorphism of two crystals, in comparison to the respective deoxygenated forms HbTb crystals, and the small changes expected due to the addition of the ligand, was skipped the research of the starting model, and we proceeded with a rigid body refinement.

The initial models used are the two structures at pH 6.2 and 8.4 of deoxy-HbTb already present in the literature [57] (PDB codes: 2H8F and 2H8D, referred as HbTb6 and HbTb8, respectively). The refinement of HbTb8NO and HbTb6NO structures was performed using the program SHELX [146]. Each refinement run was alternated with manual intervention using the molecular graphic program O [147], to correct minor errors in the position of the side chains. Water molecules were identified by evaluating the shape of the electron density and the distance of potential hydrogen bond donors and acceptors. At convergence, the R_{factor} values were 0.218 (R_{free}, 0.245) for HbTb6NO and 0.207 (R_{free}, 0.249) for HbTb8NO, respectively. A summary of the refinement statistics is presented in Table 4.6. Although crystals are affected by pseudo-merohedral twinning, the resolution of the diffraction pattern ensures sufficient data to produce a well-refined molecular structure, as evidenced by the good quality of the omit electron density maps for both the main chain and the side chains of most of the residues (Figure 4.16).

Table 4.5: X-ray data collection statistics for HbTb6NO and HbTb8NO

	HbTb6NO (pH 6.2)	HbTb8NO (pH 8.4)
Space group	$P2_1$	$P2_1$
Unit-cell parameters		
a (Å)	61.74	62.01
b (Å)	94.21	94.81
c (Å)	61.63	62.10
β (°)	90.32	90.61
Data processing		
Resolution limits (Å)	50.00-1.50	50.00-1.90
No. of observations	338986	342297
No. of unique reflections	107769	56056
Completeness (%)	95.6 (68.9)	99.1 (91.9)
Average multiplicity	3.1 (2.6)	6.1 (4.2)
Rmerge (%)	0.068 (0.20)	0.085 (0.52)
I/σ	12.1 (2.4)	17.1 (3.0)

*R*merge = $\Sigma hkl \Sigma_i |I_i(hkl) - \langle I_i(hkl) \rangle| / \Sigma hkl \Sigma_i I_i(hkl)$, where $I_i(hkl)$ is ith intensity measurement of the reflection hkl, including symmetry related reflections, and $\langle I_i(hkl) \rangle$ is its average. Values in brackets are for the highest resolution shell.

Table 4.6: Refinement statistics for HbTb6NO and HbTb8NO

	HbTb6NO	HbTb8NO
R/Rfree (%)	21.8 / 24.5	20.7 / 24.9
No. of atoms		
protein	4660	4660
water molecules	312	306
No. of residues	576	576
RMSD from ideal values		
Bond lengths (Å)	0.013	0.007
Bond angles (°)	2.9	1.9
Average B-factors (Å²)		
Protein, overall	26.5	34.2
Main chains	24.4	33.6
Solvent atoms	31.6	36.5

Consistent with Resonant Raman studies, reported above, |Fo-Fc| electron density maps of quaternary-T nitrosylHbTb, both HbTb6NO and HbTb8NO, clearly reveal a partial binding due to oxidative denitrosylation: NO binds to heme in α-chains but not in β-chains, as can be seen in Figure 4.16.

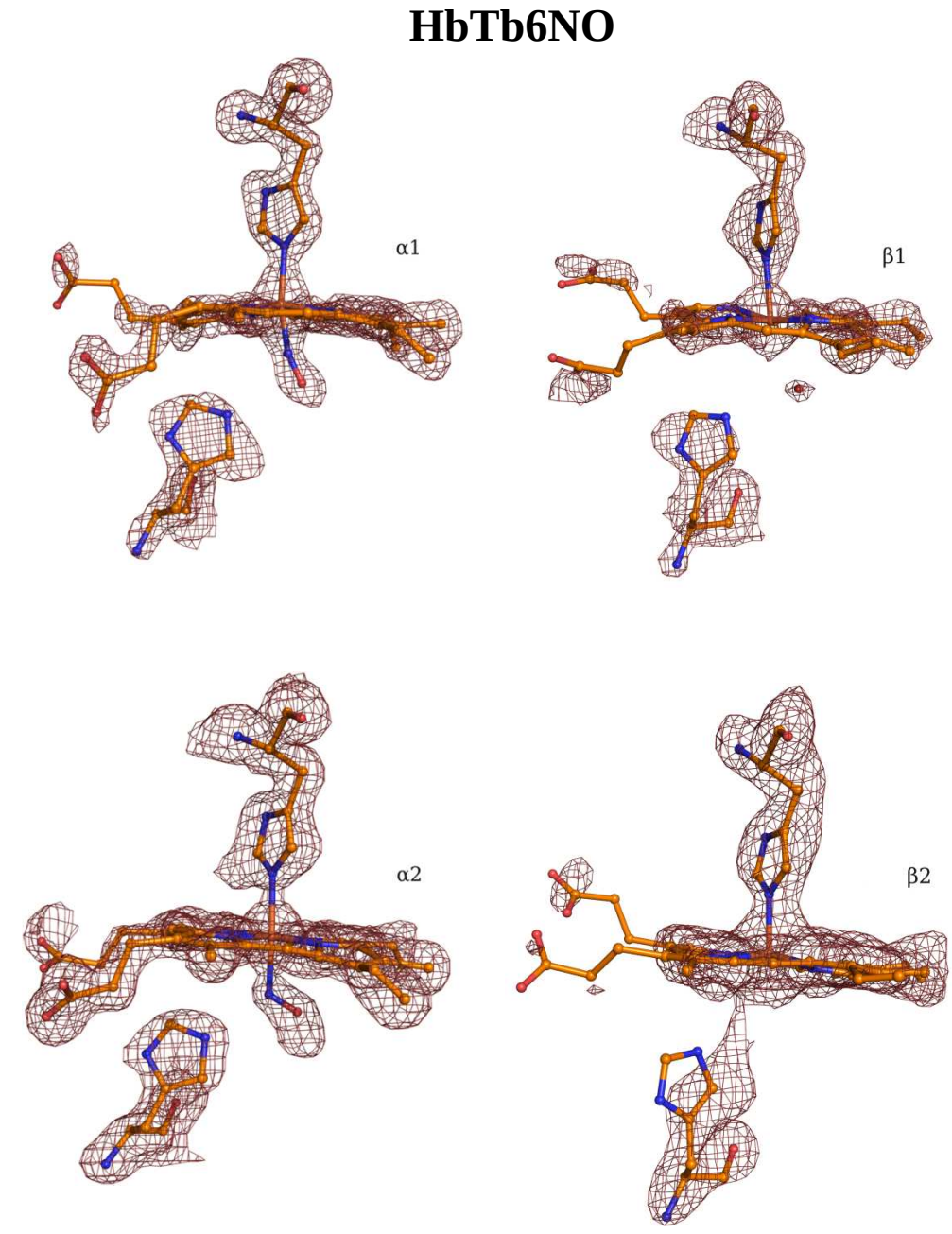

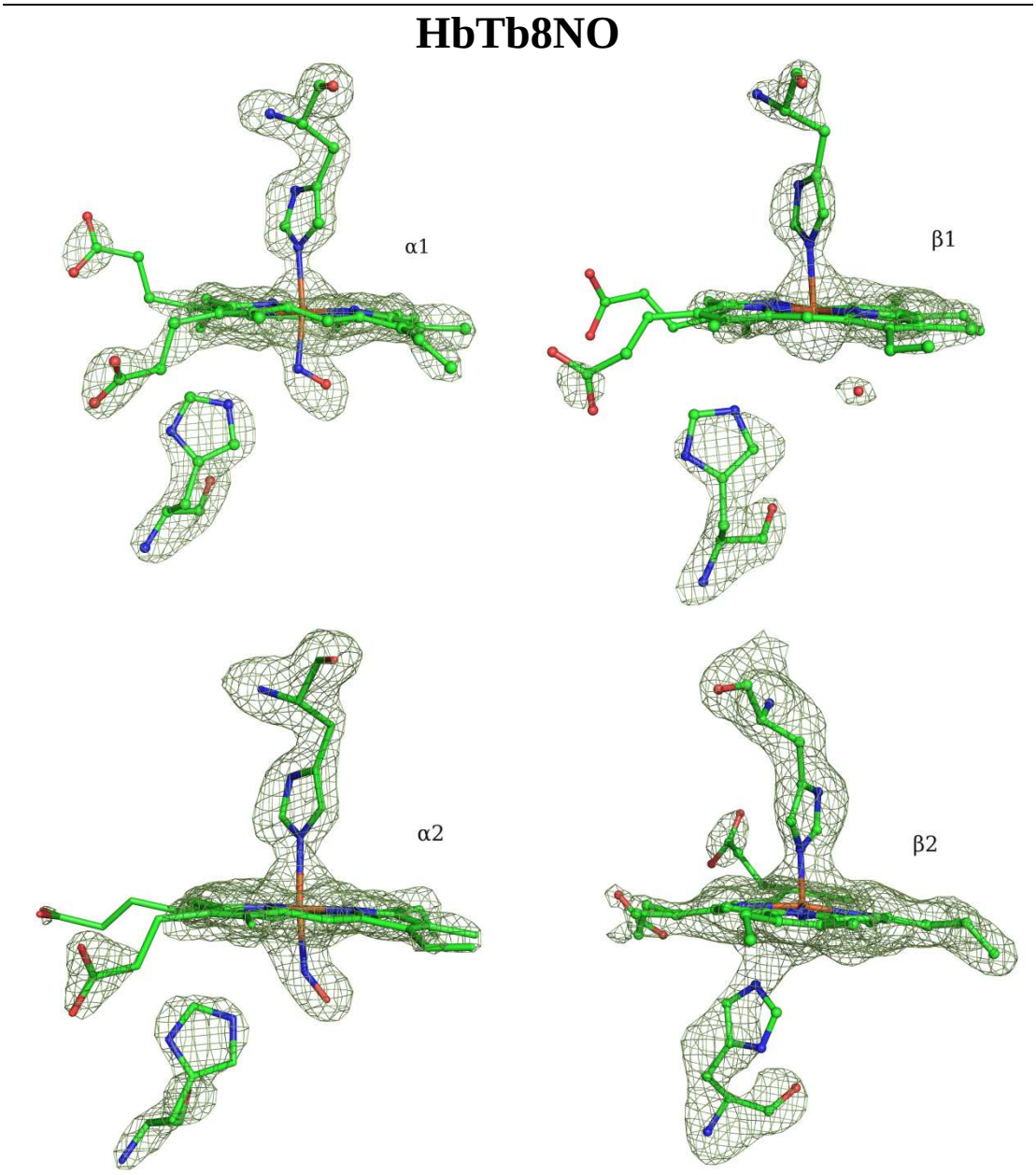

Figure 4.16: Omit |Fo-Fc | electron density maps (contoured at 3.0 σ) of HbTb6NO(above in red) and HbTb8NO (below in green) of the four heme groups.

The geometry of NO coordination in the α-chains of HbTb6NO and HbTb8NO and is very similar. Continuous electron density is observed between the α Fe and the proximal histidine in both HbTb6NO and HbTb8NO electron density maps, clearly showing that the Fe-N$^{\varepsilon}$-His88(F8)α bond remains intact after NO binds to crystalline deoxy-HbTb. Consequently, the α-heme groups are six-coordinate with both NO and the imidazole group of the proximal histidine serving as axial ligands. These results are in contrast with crystal structure of quaternary-T nitrosyl-human hemoglobin which nitrosylation of the heme groups breaks the Fe-N$^{\varepsilon}$-His87(F8)α: the distance between the α Fe atom and the N$^{\varepsilon}$ atom of His87(F8)α is 4.06 Å [100]. In the case of crystal structure of partial nitrosyl-HbTb, is found only a slight lengthening of this bond, from 2.2 to 2.3 Å, a distance that agrees well with those reported in other crystallographic studies and that is consistent with the presence of a trans axial Fe-NO bond [232].

The main differences between HbTb6NO and HbTb8NO are observed in the β-subunits, where the situation is more complex (Figure 4.16). The structures show a slightly different behavior between them. In one subunit, HbTb6NO shows a neatly shaped density centered at 2.2 Å from the iron ion, interpretable with a water molecule. In HbTb8NO, instead, the density is centered at 3.1 Å from the metal. A recently statistical analysis, conducted on x-ray structures of Hbs, myoglobins in their met-form deposited in the PDB, showed that the average iron-to-water distance is 2.08 ± 0.04 Å [67], suggesting that at pH 8, the water molecule is not coordinated to Fe. In contrast, in the second β-chain, in both HbTb6NO and HbTb8NO, no electron density is observed close to Fe. It is worth noting that in the case of HbTb8NO the distance Fe-N$^{\varepsilon}$-His63(E7)β is reduced about 1 Å (from 3.9 Å to 3.1 Å in HbTb8 in HbTb8NO), a sign of oxidation towards a partial bis-histidyl form, feature of ferric-HbTb at pH-neutral and basic [45]. This observation is supported by Raman spectra (Figure 4.10) of nitrosyl-HbTb crystals at pH 8 (ν_{10} at 1640 cm^{-1}) recorded at long air exposure time.

Table 4.7 report the Cα-Cα distances for the four subunits of structures: HbTb6, HbTb6NO, HbTb8, HbTb8NO.

Table 4.7: Cα-Cα distance of the proximal and the distal histidine residues for structures analyzed

Cα-Cα distance (Å)				
	HbTb6	**HbTb6NO**	**HbTb8**	**HbTb8NO**
α_1	13.8	14.2	14.1	14.2
α_2	14.1	14.3	14.2	14.2
β_1	14.2	14.1	14.1	14.1
β_2	14.1	14.0	14.0	13.2

It has been reported that nitrosylation of HbA in aerobic environment produces the formation of covalent adducts with Cys93β [100]. The careful analysis of electron

density maps excluded the nitrosylation of thiol groups of cysteine residues for HbTb6NO and HbTb8NO (Cys105α, Cys31β and Cys109β).
As expected, on the basis of the the isomorphism of crystals and of the adoption such conditions that force the quaternary T-state to avoid the crystal breakage due to NO binding, the root mean square deviation (RMSD), calculated on the backbone atoms (N, C^{α}, C), between the deoxygenated and nitrosylated structures, is very small (less than 1 Å).
The RMSD between the deoxygenated and nitrosyl structures at the two pH values (6.2 and 8.4) is reported in Table 4.8.

Table 4.8: Root mean square deviation (Å) between backbone of structures in analysis

	HbTb6	**HbTb8**	**HbTb6NO**
HbTb6	-		
HbTb8	0.649	-	
HbTb6NO	0.437	0.747	-
HbTb8NO	0.811	0.572	0.837

In order to obtain information on local differences induced by nitrosylation, the RMSD for residue are plotted, calculated by comparing HbTb6NO and HbTb6 (nitrosylated and deoxygenated forms, respectively, at pH 6.2) and HbTb8NO and HbTb8 (similar to pH 8.4) (Figure 4.17).

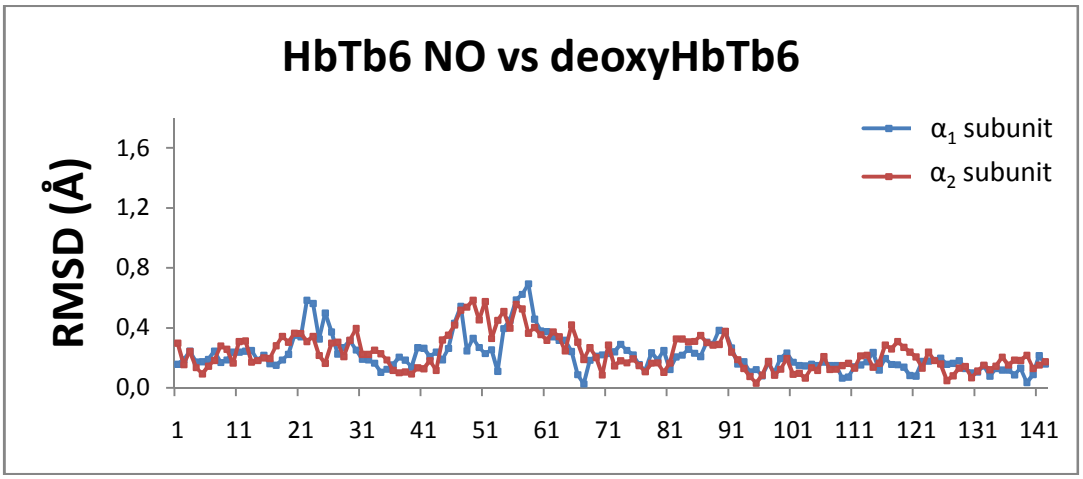

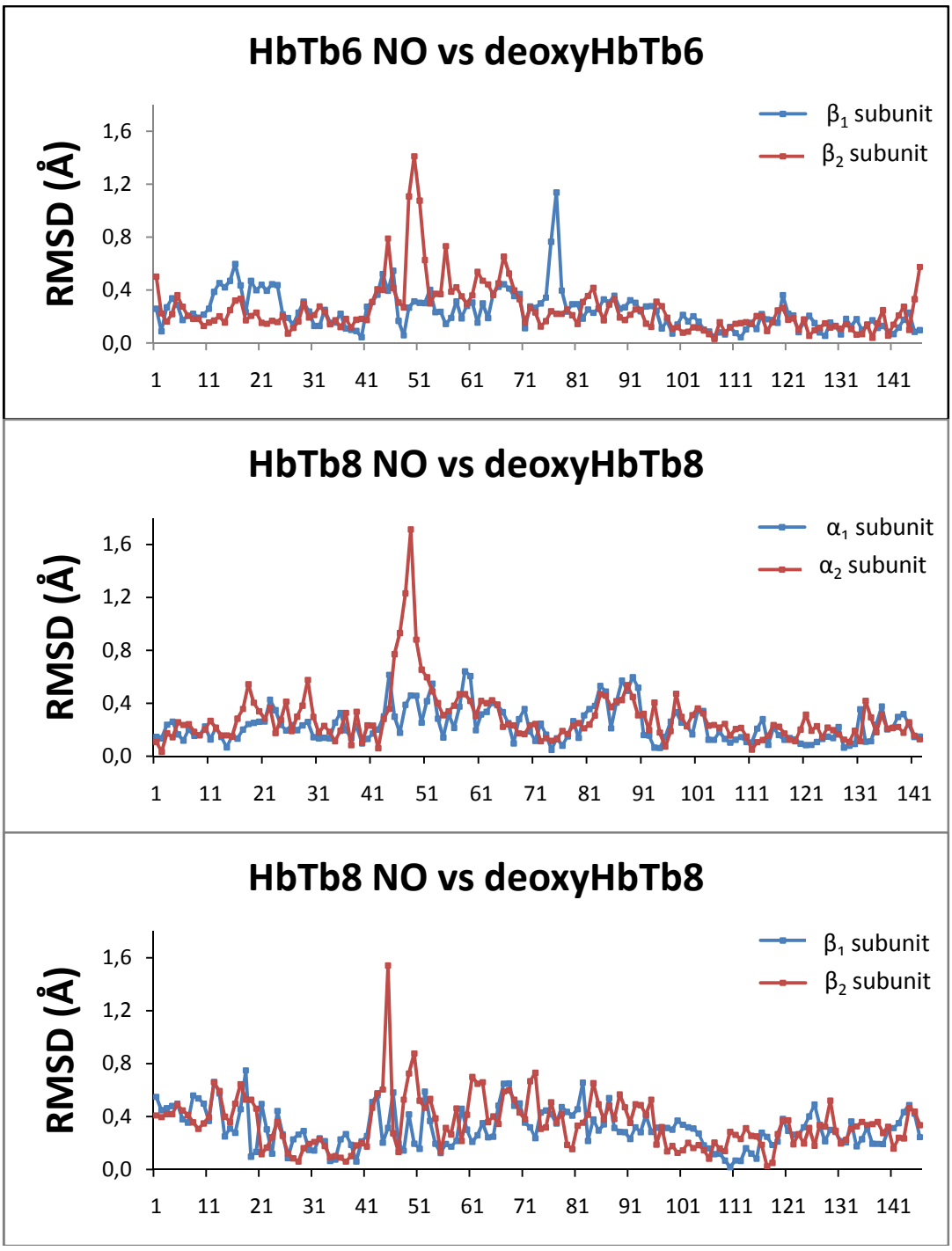

Figure 4.17: RMSD for residue between α and β-subunits of deoxygenated and nitrosyl-HbTb at the two pHs.

It is immediately apparent that the main differences are found almost exclusively in the CD loop, a flexible region that plays an important role in the transition process R/T [13] and the Root effect [57].
In the section 4.2.3 a detailed comparison among deoxygenated, partially and fully nitrosylated HbTb was discussed. The observation of a partial NO binding seemed in contrast with the RR evidence, therefore a combined study of *in situ* X-ray crystallography/Raman microscopy was planned.

4.2.2 NO-photodissociation selective X-ray induced in HbTb T-state crystals

Indeed, the combined study of *in situ* X-ray crystallography/Raman microscopy revealed an additional experimental source of denitrosylation, due to X-ray photolysis on crystals of nitrosylated-HbTb. Furthermore few months ago, X-ray induced photodissociation was reported in solution for human Hb at low temperature *via* XANES studies [233]. X-ray induced photodamage is a recently frequent phenomenon, using third generation synchrotrons. Several evidences of photodamage to protein side chains is known [234]. Raman microscopy prior and after x-ray data collection can be a valuable tool to detect such artefacts. Indeed, few examples of Raman-assisted crystallography studies have been recently reported: Br dissociation from DNA [235] and disulfide reduction [236]. Herein we report the first crystallographic evidence of a X-ray induced NO-photodissociation at 3rd generation synchrotron (Swiss Light Source), along with Raman spectra of the X-ray exposed single crystals, showing a selective photo-dissociation of α and β subunits.
As discussed above despite the reproducibility of the soaking procedure, monitored *via* RR, the in-house X-ray diffraction data collection resulted only in a partial NO coordination (see Figure 4.16) limited at the α-subunits. Since oxidative denitrosylation was supposed, a protective environment (a mixture of ascorbate 10m M and catalase 1000 U/mL) was used. But, even under this oxygen-free conditions, again a partial binding was obtained.
Diffraction data on fully ($HbTb(NO)_4$) and 3 partially nitrosylated HbTb crystals (NO1-3-HbTb) were also collected at the PXII beamline of Swiss Light Sourse (SLS) at 4 different X-ray dose, evaluated by the RADDOSE software (version.2 [237]). Diffraction statistics are reported in Table 4.9. For the fully nitrosylated HbTb 2.5 Å-resolution data (using only 2 % of the available flux) were collected. All crystals are isomorphous to the starting HbTb deoxygenated crystals [57]. All data sets were collected at 100 K using glycerol as cryo-protectant and processed with the program suite HKL [145]. A summary of the data processing statistics is reported in Table 4.9. An analysis of the collected diffraction data shows that NO-HbTb crystals present pseudo-merohedral twinning. This finding is in line with the previous results [57]. The twin fractions for NO-HbTb, were determined by the algorithm implemented in the program SHELX [146], are 0.56.

Preliminary refinements were performed with SHELX [146] to evaluate the coordination state and to evaluate the occupancy factors (Table 4.10).
The simultaneous X-ray data collection assisted by online Raman acquisition, prior and after the collection at SLS synchrotron, solved the puzzle. Indeed, at SLS the RR spectra (exciting with 405 nm) prior X-ray exposure showed a complete binding prior the X-ray exposure (Figure 4.18), as revealed by the ν_4 and ν_3 bands.

Table 4.9: X-ray diffraction statistics of fully and partially nitrosylated HbTb

	$HbTb(NO)_4$	NO1-HbTb	NO2-HbTb	NO3-HbTb
Space group	$P2_1$	$P2_1$	$P2_1$	$P2_1$
a (Å)	62.21	61.59	61.59	61.61
b (Å)	94.09	93.58	93.59	93.74
c (Å)	62.12	61.64	61.65	61.71
α (°)	90.00	90.00	90.00	90.00
β (°)	90.79	90.41	90.38	90.22
γ (°)	90.00	90.00	90.00	90.00
Resolution limits (Å)	50.0-2.5	50.0-2.15	50.0-2.17	50.0-2.24
No. of observations	249932	167905	164535	151865
No. of unique reflections	30400	37616	36709	33402
Completeness (%)	82 (68)	98.9 (92.7)	99.2 (94.4)	99.1 (94.1)
Average multiplicity	2.9	4.5	4.5	4.5
Rmerge (%)	0.09 (0.13)	0.054 (0.11)	0.053 (0.12)	0.049 (0.13)

*R*merge = $\Sigma hkl \Sigma_i |I_i(hkl) - \langle I_i(hkl) \rangle| / \Sigma hkl \Sigma_i I_i(hkl)$, where $I_i(hkl)$ is ith intensity measurement of the reflection hkl, including symmetry related reflections, and $\langle I_i(hkl) \rangle$ is its average. Values in brackets are for the highest resolution shell.

The RR data collected at increasing X-ray dose revealed a detectable decrease of the LS signal due to NO, and the appearance of a new HS signal due to a photodissociated species (deoxygenated form). Particularly, the x-ray exposure produced an almost 50 % drop of the NO band in favour to the deoxygenated form. Therefore, RR data clearly showed an X-ray induced NO-photodissociation. This kind of evidence is supposed a general properties of nitrosyl hemoglobins. Indeeed, recent solution studies revealed an X-ray induced photodissociation in human Hb at low temperature [233]. The only available NO structure of human Hb was collected at a moderate resolution (a low X-ray dose), and at room temperature. Therefore, our Raman microscopy evidence of NO-photodissociation for Hb from *Trematomus bernacchii* can have a general impact, and thus explaining the surprisingly low number of crystal structures of nitrosyl Hbs deposited in the Protein Data Bank.

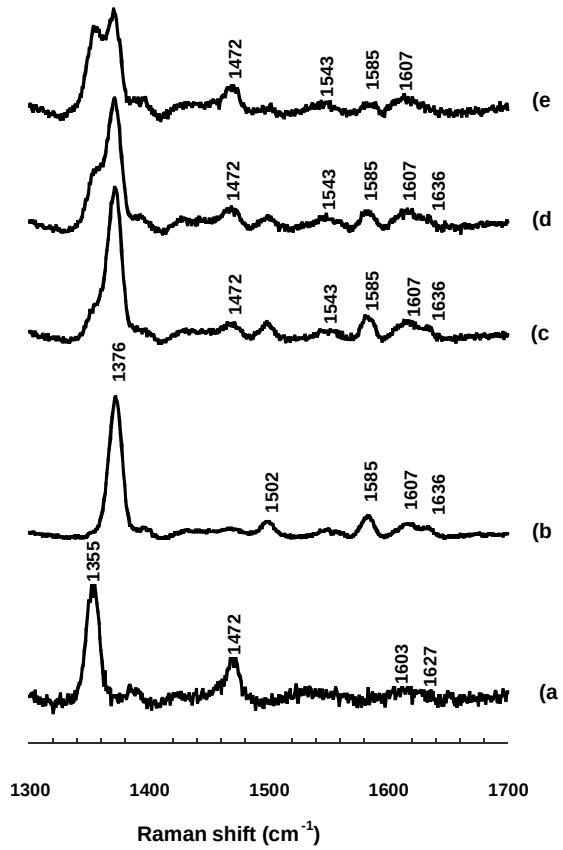

Figure 4. 18: Resonance Raman spectra (a-e) of HbTb crystals in the deoxygenated form (a), fully nitrosylated (at 0.4 MGy) (b) and partially ligated due to X-ray exposure at three different dose 4, 7.6, 11.2 MGy (c-e, respectively). Excitation line is 405 nm (50 mW at the sample), exposure time 300 s. Spectral resolution 8 cm^{-1}.

Indeed, if only a limited literature is stating the absence of expected NO in hemo-protein structure [238], an unpredictably high number of unpublished data could be kept in scientists drawers. A methodological take-home of this work is the advice to monitor NO binding *via* Raman microscopy prior and afterwards X-ray diffraction data, keeping the dose as low as possible and (if possible) working at room temperature. X-ray diffraction collections were performed at several steps of dissociation (at different X-ray dose). In order to collect a fully nitrosylated form, a 2 % of the available X-ray flux were used, corresponding to a 2.5 Å resolution, despite the crystal diffracted better. Electron density maps from these moderate resolution data provide a clear qualitative and quantitative interpretation of the changing intensity of the NO signal (Figure 4.19). Indeed, almost only the β-subunits undergoes photodissociation, whereas α subunits are still in a nitrosyl state. (Figure 4.19 b-d). In order to make the comparison as consistent as possible, Figure 4.19 shows electron

density maps evaluated by using data at the same resolution (2.5 Å) and at the same electron density level (2.8 σ). From inspection of Figure 4.19 (and Table 4.10) it is clearly evident that NO photo-dissociation occurs at a different degree at the α and β-subunits. Indeed, the NO photodissociation is almost confined to β-hemes.
The refined occupancy factor for NO are reported in Table 4.10, along with X-ray dose used, and the ratio between the ν_4 and ν_2 intensity corresponding to the deoxygenated and nitrosylated forms. This is probably the first example of a crystallography-assisted Raman microscopy meyhod for evaluating relative resonance Raman cross-section of different coordination states starting from crystallographic refinement of occupancy factors.

Table 4.10: Occupancy factors and relative intensity of some Raman bands for the nitrosylated and photodissociated species

Collection	**Dose (MGy)**	**NO occupancy (α,β)**	$\mathbf{I_{1355}}$ / $\mathbf{I_{1370}}$	$\mathbf{I_{1475}}$/ $\mathbf{I_{1505}}$
$HbTb(NO)_4$	0.4	1.00, 1.00	0	0
NO1-HbTb	4.0	1.00, 0.90	0.2	1.2
NO2-HbTb	7.6	1.00, 0.76	0.6	1.3
NO3-HbTb	11.2	1.00, 0.48	0.8	2.8

Ultimately, our combined crystallographic and spectroscopic method has provided 1) an experimental protocol to detect X-ray induced NO-photodissociation on hemoprotein crystals, and 2) a quantitative information on the relative Raman cross-section of deoxygenated and nitrosylated Hbs, useful to evaluate the degree of NO-photodissociation for future studies.

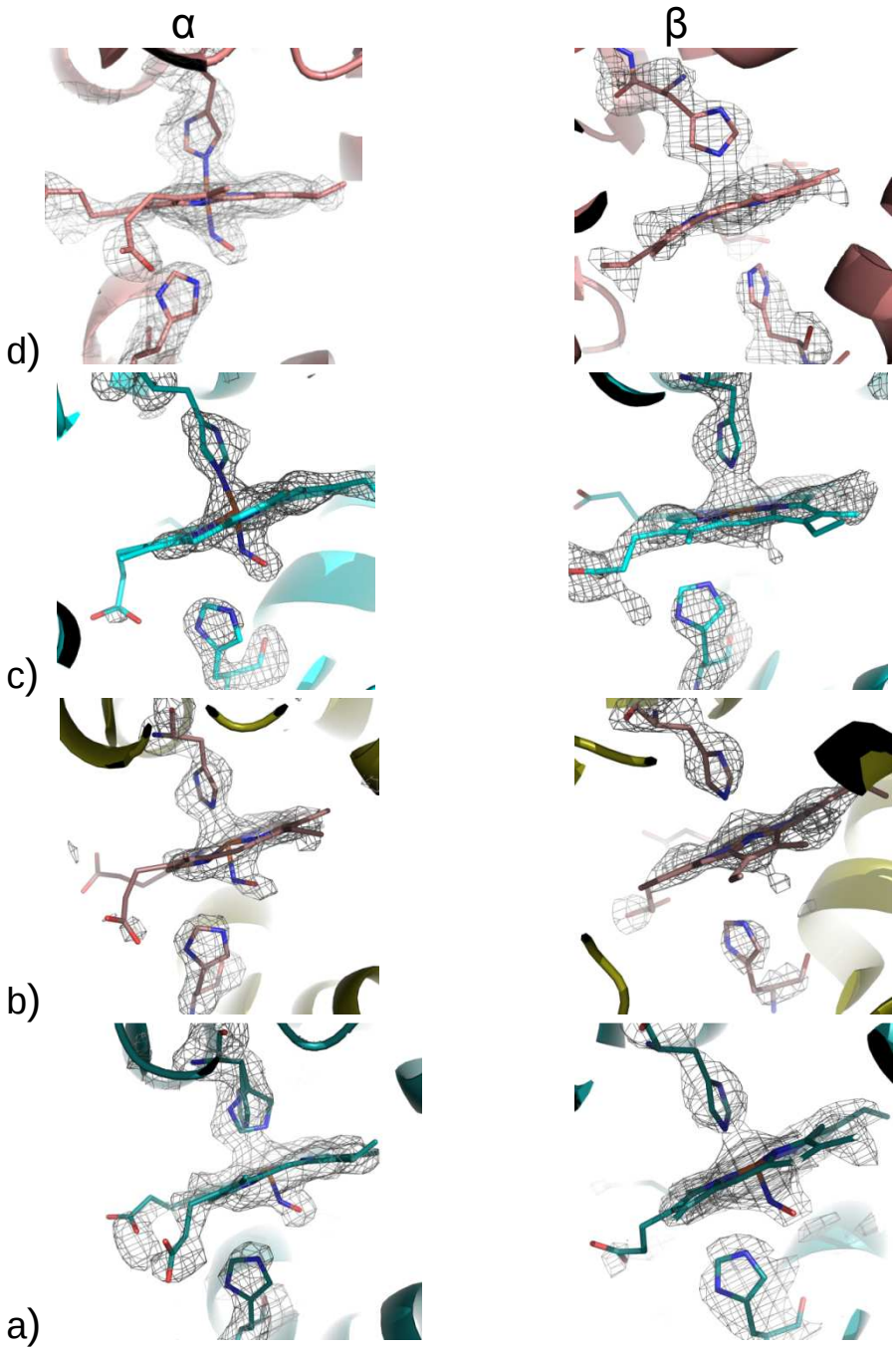

Figure.4.19: Electron density maps of the fully and partially ligated NO-HbTb at different X-ray dose: 0.4, 4.0, 7.6, 11.2 MGy (a-d). Maps have been prepared using data at the same resolution (2.5 Å) and at the same electron density level (2.8 σ**).**

4.2.3 Comparison among deoxygenated, partially and fully nitrosylated HbTb

The nitrosylation does not induce variations in the overall structure of HbTb$(NO)_4$ which displays all the features typically associated to Hbs in the T-state. The RMSD computed on the Cα atoms with respect to the structures of deoxy, HbTb6 [57], and partially ligated, HbTb6NO, is 0.46 Å and 0.42 Å, respectively. Furthermore in order to obtain information about the flexibility of the polypeptide chain are plotted of relative B-factors of each residue, that is the average value of the normalized B-factors per the average B factor of the whole structure, as a function of the residue. The analysis of the diagrams for deoxygenated form (HbTb6), partially (referred in figure 4.20 to as HbTb6NO-partial) and fully nitrosylated (HbTb6NO referred in figure 4.20 to as) at pH 6 (Figure 4.20), showed no significant differences between the structures : the larger values are unevenly distributed along the chain and are particularly associated to the CD loop.

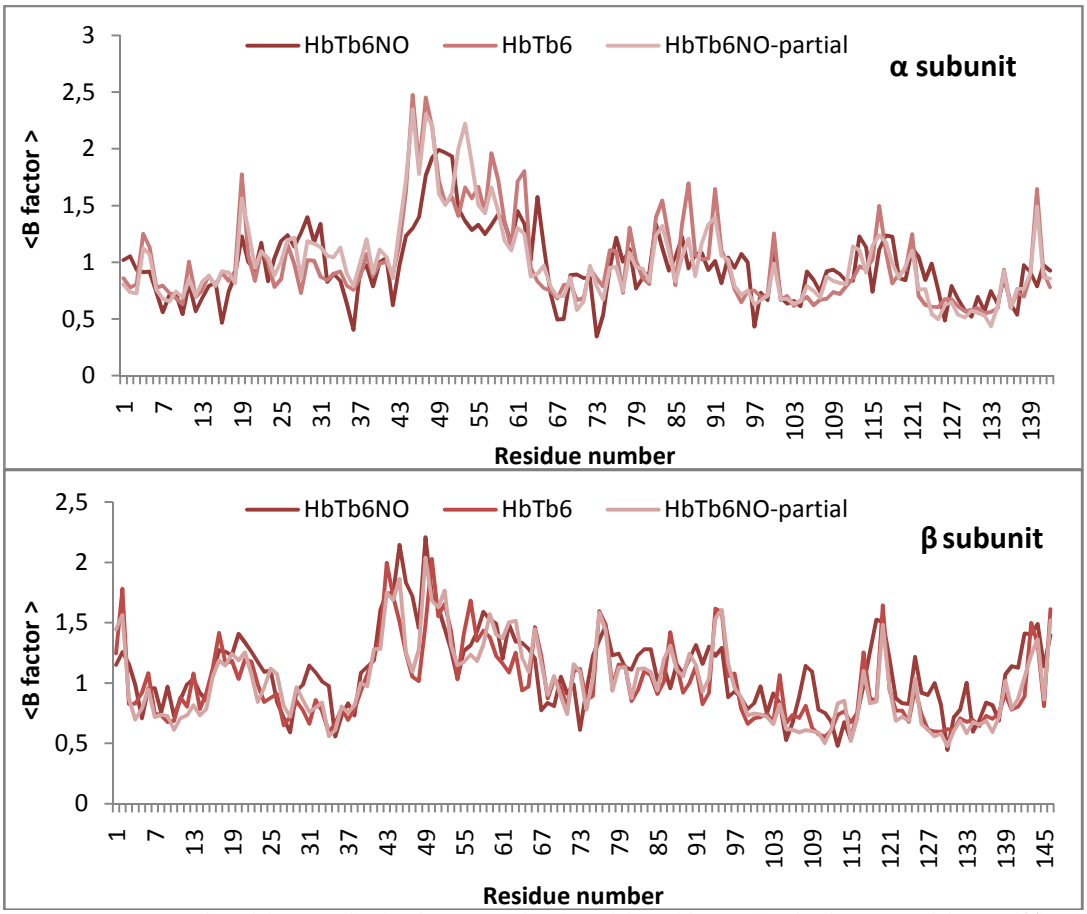

Figure 4.20: Average value of the normalized B factors as a function of the residue number for deoxygenated form (HbTb6), partially (HbTb6NO-partial) and fully nitrosylated (HbTb6NO) at pH 6, for the α (above) and β chains (below)are reported.

However, some elements of tertiary structure (in particular the salt bridges present in the deoxygenated forms) are modified after nitrosylation.
The strong stabilizing interaction, at acid pHs, between the Asp triad (95α, 99β, 101β) at the $\alpha_1\beta_2$ ($\alpha_2\beta_1$) interfaces in deoxygenated Root effect-Hbs, (shown in Figure 4.21 for HbTb8NO and HbTb6NO) is an important structural motif recognized as the minimal structural requirement for Root effect [46, 55, 57, 63]. Albeit slightly, these interactions appear to strengthen the interface following the NO binding, especially at the interface $\alpha_2\beta_1$ at pH 8.4 (Table 4.11).

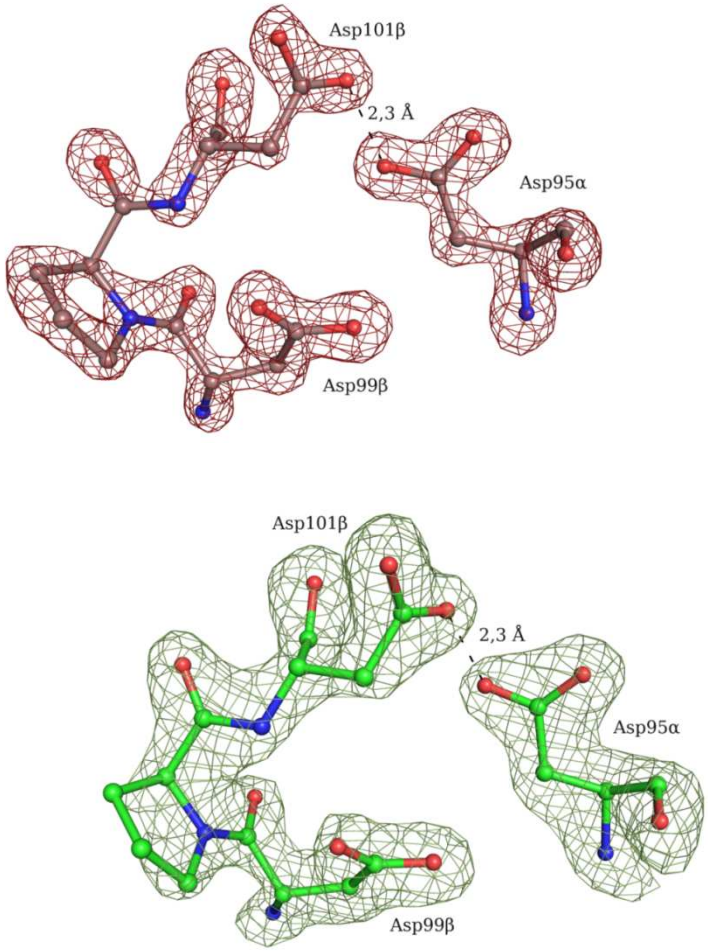

Figure 4.21: Omit Fo-Fc electron density maps (contoured at 4.5 σ) at the $\alpha_1\beta_2$ interface for HbTb6NO (above in red) and HbTb8NO (below in green).

Table 4.11: Distances (Å) between O^{δ} of Asp95α and Asp101β side chains at the $\alpha_1\beta_2$ and $\alpha_2\beta_1$ interfaces of the deoxy, fully and partially nitrosylated HbTb structures, at pH 6 and 8.

	HbTb6 (deoxy)	HbTb6NO (partial)	$HbTb(NO)_4$ pH 6.2	HbTb8 (deoxy)	HbTb8NO (partial)
$\alpha_1\beta_2$	2.5	2.3	2.5	2.5	2.3
$\alpha_2\beta_1$	2.5	2.6	2.3	3.2	2.8

Two other salt bridges, between the side chains of His146β - Glu94β and His69β - Asp72β mentioned as interactions that contribute, though small, to the Root effect [57], are slightly changed due to binding (see Table 4.12). His146β has been proposed to be responsible for a large fraction of Bohr effect in human Hb, where it forms a strong hydrogen bond with Asp94β [17]. In fish Hbs, Asp94β is replaced by a Glu residue. In deoxygenated HbTb structure, at pH 6, despite the favorable conformation of $His146\beta_1$, the distance from $Glu94\beta_1$ is too large (4.6 Å) for a hydrogen-bond interaction [57], in nitrosyl form is found strengthening of this interaction (Table 4.12).

His69β, located at the region of the Eβ helix, in HbTb6 is salt-bridged to Asp72β (2.7 Å)[57]. This interactions is perfectly maintained in HbTb6NO and in β_1 of $HbTb(NO)_4$, but in the latter in β_2 the distance is significantly lengthened (3.4 Å). At pH 8 in HbTb8NO, as in deoxygenated structure [57], this interaction is retained in β_1, where His69β is affected by packing interaction, but destroyed in β_2, where no significant packing interactions occur (Table 4.12).

Table 4.12: Distances (Å) between the O^{ε} of Glu94β and N^{ε} of His146β and between the N^{δ} of His69 and O^{δ} of Asp72 of the structures in analysis, at pH 6 and 8.

	HbTb6 (deoxy)	HbTb6NO (partial)	$HbTb(NO)_4$ pH 6.2	HbTb8 (deoxy)	HbTb8NO (partial)
$His146\beta_1$ -$Glu94\beta_1$	4.6	3.5	3.4	*	*
$His146\beta_2$ -$Glu94\beta_2$	*	*	*	*	*
$His69\beta_1$ –$Asp72\beta_1$	2.7	2.5	3.4	2.7	2.8
$His69\beta_2$ –$Asp72\beta_2$	3.0	3.0	2.9	3.3	*

(*) The distance is greater than 5 Å.

CDα Region

The largest deviations due to binding are located at the CDα region. In the deoxygenated form His55α at low pH is salt bridged to Asp48α and forms a π-stacking interaction with Trp46α, His45α on the other side of Trp46α, is in contact with the side chain of this residue and with a propionate group of the α-heme [57]. In the nitrosylated form, instead, the salt bridge between His55α and Asp48α is lost, the π-stacking interaction with Trp46α is also weakened, and His45α side chain flips assuming a T-shaped interaction with the aromatic side chain of Trp46α [73]. These events are clearly showed in Figure 4.22 in which are superimposed residues of the CDα region, heme and His59α of deoxygenated (black), fully (marine blue) and partially nitrosylated structures (grey) of HbTb.

Noteworthy, the dissociation of NO at β-heme induces, *via* heme-heme communication, changes of tertiary structure in CDα region, precisely those interactions that were suggested to be contributor to the Root effect in HbTb [57, 58].

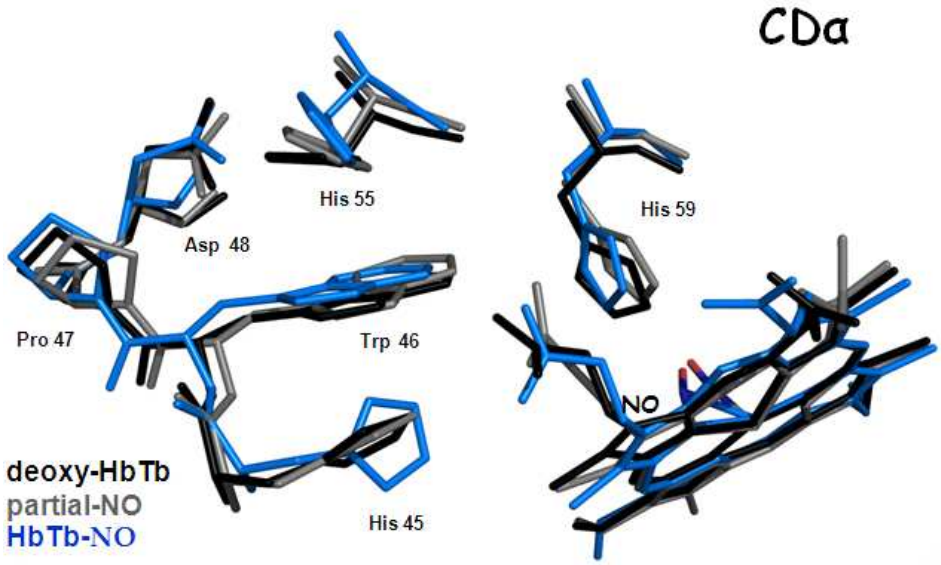

Figure 4.22: Superimposition of residues of the CDα region, heme and His59α of HbTb structures, at pH 6.2, in the deoxygenated form (black), fully (marine blue) and partially nitrosylated (grey) re-oriented to afford the best superimposition of the CDα region of the three models.

A comparison of the overall structure of HbTb6 and HbTb$(NO)_4$ clearly indicates that the structural modification associated with ligand binding at the α heme is propagated to the β heme (Figure 4.23). The modifications of the CDα region are transmitted to FGβ corner either directly or through the heme (Figure 4.21). As a result of the NO binding (see Figure 4.23), the subunits α_1 and β_2 (in blue), move slightly away, unlike to deoxygenated form (in black), towards a structure, that although still T, is about to transit to the R state.

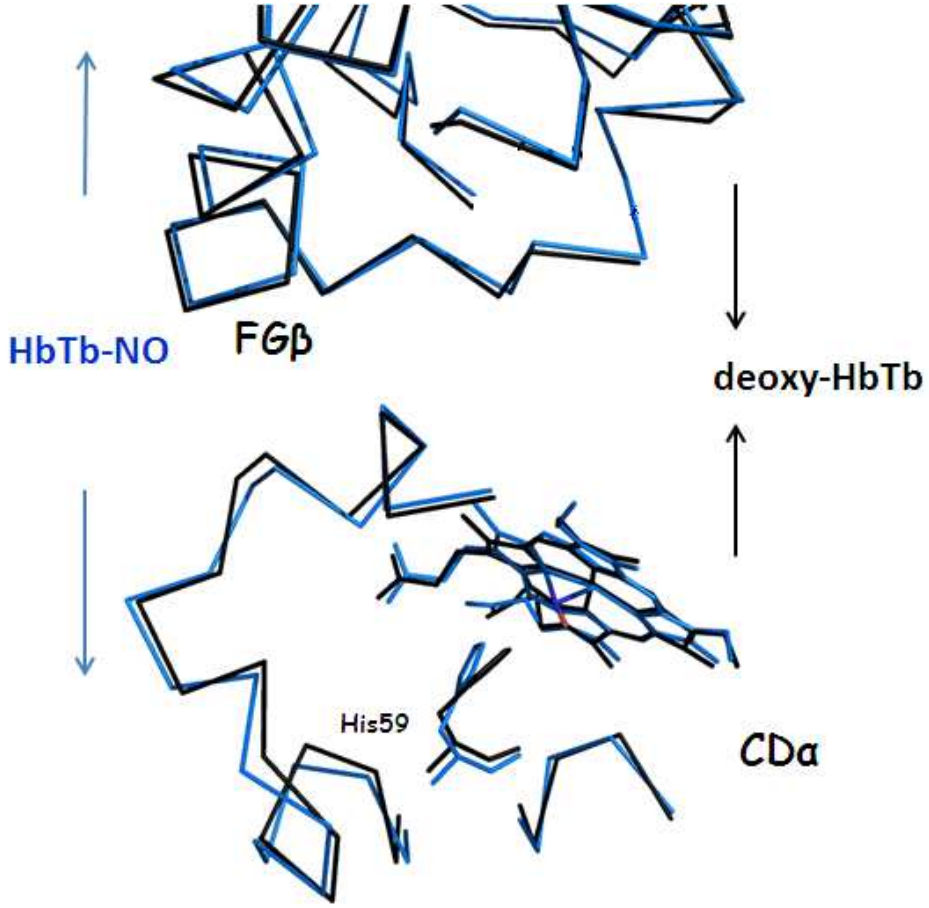

Figure 4.23: Representation of the modifications induced by the ligand binding. The Cα trace, of the CDα region and FGβ helix, of HbTb6 (deoxy-HbTb, in figure) and HbTb$(NO)_4$ (HbTb-NO, in figure) structures is colored in black and blue, respectively. His59α, heme and NO molecule are shown in sticks representation.

Chapter 5

Raman Imaging and mechanical characterization of healthy and diseased red blood cells

Biochemical assays are labor intensive, not applicable to single cells and are unable to monitor changes *in situ*. Raman spectroscopy is a well established technique for the chemical identification of molecules. The development of confocal Raman microscopy and cellular imaging, for single living cells, is of particular interest in cell and molecular biology as it helps to observe and understand important cellular processes in real time, without the use of exogenous markers [239]. Therefore, the combination of this technique with an Optical Tweezers system (Raman Tweezers), allows to select and manipulate individual cells *ex vivo* to study the cellular diseases, such as thalassemias and hemoglobinopathies [240].
In this section, we present the results of the characterization spectroscopic and of mechanical properties of human healthy and anemic erythrocytes (affected from HbS (β6Glu → Val), HbC (β6Glu → Lys) and HbSC), by Raman imaging and Optical Tweezers studies, in order to define protocols to differentiate healthy from pathological erythrocytes.
The experiments of Raman Imaging were a) performed by Dr. Alessandro Vergara in collaboration with Prof. Cees Otto at the University of Twente, Netherlands, and b) analyzed by myself. The experiments of mechanical properties by Optical Tweezers were performed and analyzed by myself in collaboration with Prof. Antonio Sasso at the Department of Physical Sciences of the University of Naples "Federico II".

Raman Imaging

Modern biology is increasingly interested in having a better understanding of the inner workings of cells and their communications amongst each other. This need requires new tools and methods that enable us to follow cellular pathways in living cells with minimal disturbance. Although several experimental techniques provide the morphology of single cells, only few of them are able to reconstruct the distribution of an assigned protein within the cell itself [241]. The field of optical bio-analytical

techniques has been dominated, for decades, by fluorescence based techniques. However, this techniques often require staining with specific fluorophores, which, in some cases, can affect the normal cellular function. Other single-cell analysis and imaging techniques, such as electron microscopy or secondary ion mass spectrometry (SIMS) can complement optical methods by providing higher spatial resolution or chemical information, but they either only work for frozen or fixed cells, or they destroy the cells during the analysis. Thus, since non-destructive optical methods can a) continuously analyze living cells during their lifecycle, b) probe their interactions with other cells, and c) provide details about cellular chemistry, they are highly desired. Among these, Raman spectroscopy and imaging is rapidly gaining popularity, because it enables the nondestructive, label-free biochemical analysis of individual living cells, which complements very well other molecular, cellular, and physiological analysis techniques [242].

The main goals of application of Raman scattering in biology are to identify, locate and, possibly, to follow the chemical changes of the molecules in time. Indeed, since the late 1960s Raman spectroscopy has been widely applied to study biological macromolecules such as nucleic acids, proteins and lipids [243-246].

Confocal microscopy is a standard optical technique used to increase micrograph contrast and/or to reconstruct three-dimensional images by using a spatial pinhole to eliminate out-of-focus light or flare in specimens [247]. Confocal microscopy offers several advantages over conventional wide field optical microscopy, including the ability to control depth of field, the elimination or reduction of background information away from the focal plane (that would lead to image degradation), and the capability to collect serial optical sections from thick specimens.

The first studies using Raman micro-spectroscopy, at a single cell level were made animal [248] and bacterial [249] cells. Since then, non-stimulated micro-Raman spectroscopy has taken significant strides toward becoming an accepted technique in the biological sciences for investigating the biochemistry of single cells, micro-organisms, and subcellular components. This direction continued to develop and during last years Raman micro-spectroscopy and imaging was applied to study versatile biological processes also in different human cell types [250-256]. Applications in a wide variety of fields, such as microbiology [257-259], cancer research [260, 261], and cardiovascular research [262, 263] have been demonstrated.

The development of the confocal Raman microscopy has permitted to couple the structural and chemical information contained in Raman spectra with spatial information, with a lateral resolution which is in principle only limited by light diffraction. Spectral characteristics can be "mapped" on the sample, in the approach named "Raman mapping or imaging", by superimposing a two-dimensional grid of points over the sample and collecting a whole spectrum from each point [264].

The Raman cell images (obtained by a combination of confocal Raman microscopy and simple data analysis tools) can be more easily interpreted than spectra alone by biomedical researchers already familiar with microscopy. The values of the intensity at

a certain peak or peaks are plotted as a function of position. These images provide more information than conventional microscopy images alone as they contain information on all cell components and different cell components can be visualised by post-processing of data. So far, single living cells and sub-cellular compartments can be molecularly examined rapidly, non-invasively, and without the use of external markers or fluorescent dyes. This novel technique has great potential in medical applications, tissue engineering, for determining where assignment biochemical transformations occur inside a cell with spatial resolution of a few nanometers.

Erythrocytes and hemoglobinopathies. Our case of study

The erythrocytes, also referred as to red blood cells (RBCs), are the most numerous blood cells (about 4-6 millions/mm^3) and play an essential role in respiratory function. A typical erythrocyte has a disk diameter of and a thickness of 2 μm, being much smaller than most other. The human RBCs represent a very simple cell that can be schematized as vesicles (cell membrane), devoid of the nucleus and rich in hemoglobin (Hb). The high symmetry and the chromophoric structure of the heme of Hb result in strong enhancement of the Raman Scattering (up to 4 order of magnitude higher than in the nonresonant case, see Methods section) using laser wavelengths close to the heme electronic absorption bands [256, 265-267]. The occurrence of Raman Resonance spectroscopy (RR) from the Hb prostheic group allows the investigation of the Hb inside a single erythrocyte without any influence of the surrounding globin or other parts of the RBC crossed by the Raman probe [209, 268]. This is a quite interesting issue for the characterization of Hb-related blood diseases, such as the hemoglobinopathies.

The hemoglobinopathies are the most common monogenic diseases and one of the world's major health problems. They includes all genetic hemoglobin disorders. The hemoglobinopathies fall into two main groups: thalassemia syndromes and structural Hb variants (abnormal hemoglobins). Both are caused by mutations and/or deletions in the α- or β-globin genes. When gene defects cause Hb synthesis disorders, this gives rise to thalassemia (α- and β-thalassemia are the main types of thalassemia). Hb structure in these cases is normal. When they cause changes in Hb structure, this mutation gives rise to abnormal hemoglobin; the main structural hemoglobin variants are HbS, HbC and HbE [269].

The HbS (sickle cell hemoglobin) and HbC, are aggregating hemoglobins and, for decades, have been of interest to structural biologists, pathophysiologists, and clinicians. HbC (β6Glu → Lys) shares with HbS (β6Glu → Val) the site of mutation at position 6 of β chain, but the consequences of the specific substitutions are very different. In red blood cells, deoxygenated HbS forms polymers [270]. Accumulation of the sickle cell polymers deforms red blood cells into a sickled shape, leading to vaso-occlusion (Figure 5.1) and other pathologies.

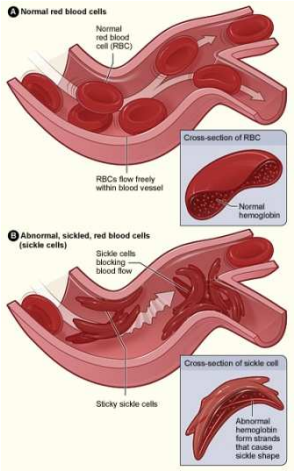

Figure 5.1: A shows normal red blood cells flowing freely in a blood vessel. The inset image shows a cross-section of a normal red blood cell with normal hemoglobin. Figure **B** shows abnormal, sickled red blood cells blocking blood flow in a blood vessel. The inset image shows a cross-section of a sickle cell with abnormal (sickle) hemoglobin forming abnormal strands.

HbC forms intraerythrocytic crystals in the oxygenated state [271]. The formation of these crystals initiates the pathophysiology of homozygous CC disease and contributes to the significantly more severe heterozygous SC disease (For a review of the clinical manifestations, see Nagel and Steinberg 2001 [272]).
Here is shown an application of Raman imaging in reconstruction of the Hb distribution within a single RBC. In particular the results of the characterization of comparative study between human healthy (A) erythrocytes and erythrocytes of three patients heterozygous for HbS, HbC and Hb C+S (S, C and C+S respectively) were reported.

Experimental method

The Raman spectra of RBC depends on the excitation line [273], due to the occurrence of Resonance Raman effects. In order to limit heating and photochemical reactions, we avoided both the violet and green lines. Therefore, we preferred the 647 nm excitation line, that provides a quasi off-resonance condition. With the 647 nm line, numerous bands associated with the porphyrin macrocycle and globin component of Hb molecule are apparent [273] (Figure 5.2).

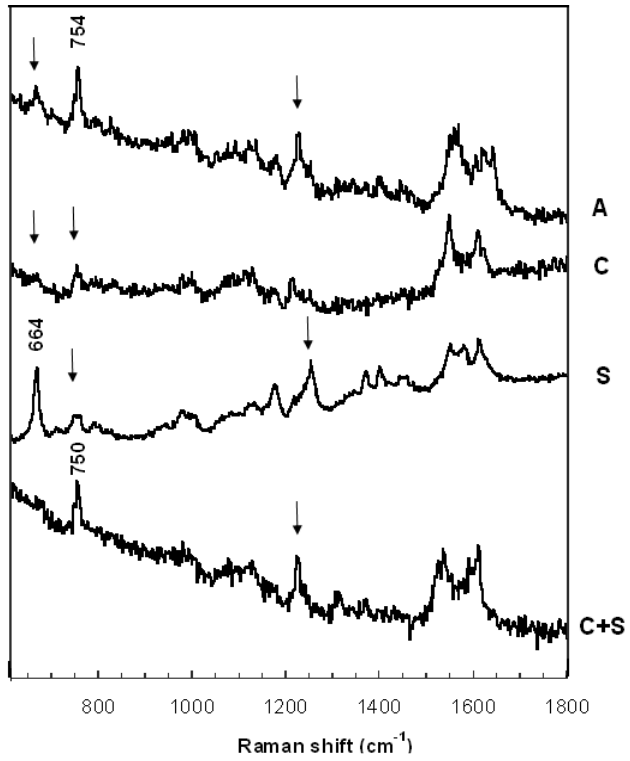

Figure 5.2: Raw Resonance Raman spectra in the oxygenated form for human healthy (A) erythrocytes and erythrocytes of three patients heterozygous for HbS, HbC and Hb C+S (S, C and C+S respectively). Excitation line is 647 nm (1 mW at the sample).

Raman spectroscopy and imaging experiments of RBCs were performed on a homebuilt confocal Raman microspectrometer [274]. The Figure 5.3 illustrates the main components of experimental set-up of the laboratory of Prof. Cees Otto (University of Twente, Netherlands), used for these experiments.

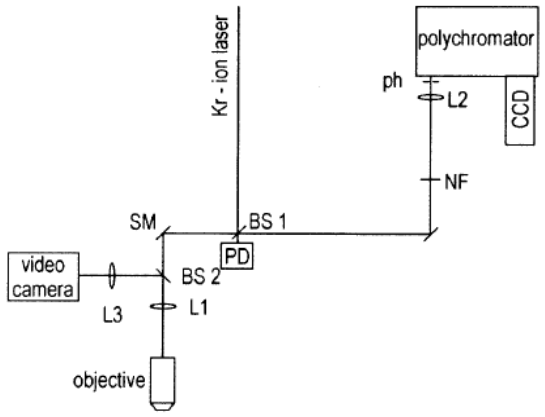

Figure 5.3: Scheme of the confocal Raman microscope. BS1 - dichroic beamsplitter. Images were acquired by scanning the sample with a scanning mirror (SM) (Leica Laser technique). BS2- pellicle beamsplitter;NF-holographic notch filter; L1-lens (focal length f_1=100 mm); L2- lens (f_2=35 mm); L3- lens (f_3=100 mm); PD-photodiode; ph-confocal pinhole (image dapted from reference [251]).

A Kr-ion laser (Coherent, Innova 90-K, Santa Clara, CA) provided the excitation wavelength of 647.1 nm. Raman images were collected in the following way: a) during Raman imaging a full spectrum (width 1600 cm^{-1}) was recorded at each position of the laser beam; b) Raman images of a single cell in a selected vibrational band of interest were reconstructed after the measurement. A water-immersion objective (100x, Zeiss Plan Neofluar, Carl Zeiss, Thornwood, NY) was used for the acquisition of all Raman spectra and Raman images. A blazed holographic grating with 600 gr/mm (Jobin-Yvon, Paris, France) was used for dispersion, the spectral resolution on the charge-coupled device (CCD) camera was 1.7 cm^{-1}/pixel and placed at the spectrometer exit. The output power of the laser source during Raman imaging was monitored by a photodiode in synchronicity with the raster scanning in Raman imaging. Raman spectra of the cells were recorded with 1 mW laser power and the accumulation times of 1s per spectrum.
Raman and Cluster images of a single cell, in the vibrational band of interest, are reconstructed after the processing of the Raman data based on:

- **Singular value decomposition** (**SVD**) is a method from linear algebra [275] for factoring a matrix A (mxn) into the product of three matrices: a matrix *U* (mxn), a diagonal matrix S (nxn) and a transpose of an ortogonal matrix *V*(nxn):

$$A = USV^T$$

where U is a matrix containing the so-called "basis spectra", which are normalised component spectral shapes that combine to form the family of spectra in the data matrix; S is a diagonal matrix containing the "singular values", the magnitude of which are the weights of the basis spectra and V is a matrix containing the "amplitude vectors" as a function of the experimental variable. SVD was applied to analyze the Raman spectral datasets for the reduction of noise in the images datasets and subsequent analysis of the spectral content.

- **Principal component analysis** (**PCA**) is the first step in the cluster analysis procedure. PCA is a mathematical reduction of the dimensionality of the measurement matrix into fewer variables (principal components), which describe the most significant variance between the data [239] and allows extracting the information from noise-filtered spectra, defining relevant components of the Raman spectra that are clustered.

- **Hierarchical cluster analysis (HCA)** was performed to create a partitioning of the cellular space into several regions (clusters) examining the interpoint distances between all samples in the high-dimensional measurement space and the resulting images are "chemical maps" in which the sample is divided into areas (i.e., group of pixels) having different colors, where each color corresponds to a different cluster.

We selected 650 cm^{-1} as vibrational band of interest, since it comes froma spectral region sufficiently different for the three different cells (see below). Successively, both Cluster and Raman images can be constructed (Figure 5.4). The Raman image gives

the quantitative distribution of one component within the cell, whereas the cluster analysis provides an image of the principal components revealed within the cell.

Sample preparation

Fresh blood was obtained by a clinic case in a family (mother, father and daughter, respectively heterozygous for HbS, HbC and Hb C+S). Control samples were drawn from normal adults. The samples were kindly provided by the consenting patients of Dr. Michela Grosso (Department of Biotechnology and Biomedicine of University of Naples "Federico II"). To acquire space-resolved spectra it is necessary to settle down the cells. The cells were deposited on a glass slideh. After incubation at 37°C for 30 minutes, the adhered cellswashed 3 times in PBS. A glass slide containing cells or was transferred to a petri dish and 3 mL of PBS was added.

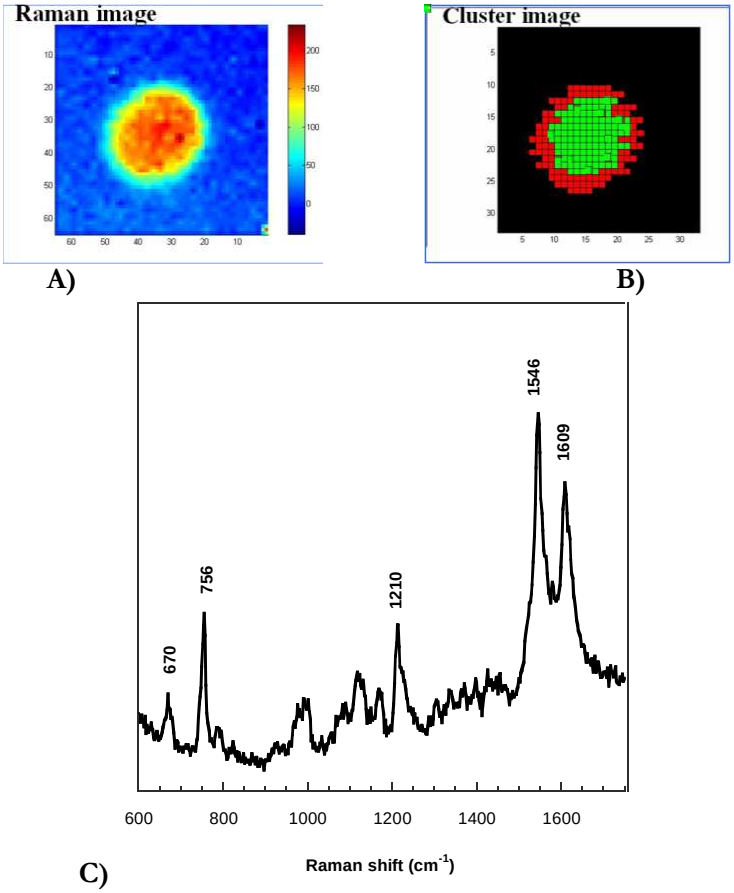

Figure 5.4: Example of (A) Raman image for deoxy healthy erythrocyte using the Raman signal at 650 cm^{-1}, (B) corresponding HCA image, which each color represents a different cluster and (C) average Raman spectrum.

Results and Discussion

Raman spectra both healthy and anemic RBCs from patients heterozygous for HbS, HbC and Hb C+S (samples S, C and C+S respectively) are recorded, in the oxygenated and deoxygenated state, using 647 nm excitation, 1024 s of laser exposure and 1 mW of defocused laser power.

HCA allows the mapping of the maximum number of chemical species having distinct Raman spectra. Being hemoglobin the most abundant species in erythrocytes and homogeneously distributed throughout the cell, HCA images, for RBCs examinated, are comprised essentially of clusters of hemoglobin, photoproduct of the Hb and background.

The Raman spectra of the deoxygenated cells were indistinguishable. Consistently, in the deoxygenated state the samples do not show photosensibility at all, and the Raman and Cluster images of healthy, C, S and C+S cells are practically indistinguishable (for example healthy deoxygenated cell is reported in Figure 5.4), thus little informative.

On the contrary, the Raman spectra of the oxygenated forms were distinguishable for human A, S, C and C+S cells (see Figure 5.2). Particularly, a different photosensibility to the 647 nm excitation is shown by the three cells. More generally, when biological samples are exposed to laser radiation it is important to be aware of possible photoinduced effects. These last have been investigated for normal RBC exposed to visible and IR radiation [273]. In general, it has been established [273] that exposure to high power radiation in the green region leads to protein denaturation and Hb transfer into the metHb state, in which the oxygen is irreversibly bound to the heme.

In particular our experiments exhibit this trend of photosensitivity: C<C+S=healthy<S.

In the S cells, there is an instantaneous appearance of a photoproduct with a high bands at 664 cm^{-1}, and a low at 750 cm^{-1} , with a relative intensity inversed with respect to healthy cells (Figure 5.2, S). This photoproduct is typical of S cells only (Figure 5.2, S). In HbA, at short time there is a stable oxy spectra, that at longer times (100 s) tends to change the ratio between the two 650 and 760 cm^{-1} bands (data not shown). These two well separable Raman bands are suggested as marker of photosensibility. Consistently Raman and Cluster images have been reconstructed for healthy, S and C cells using the signal at 650 cm^{-1}.

The different time-scale of photosensitivity is reflected in the Raman and cluster images, collected during a photo-induced chemical evolution in the healthy cells. Consistently, healthy RBCs show a spatial heterogeneity within the sample during the data acquisition (1024s exposure time), due to a partial transformation of the oxy form into a photoproduct. In Figure5.5 are compared the Raman and HCA images for normal RBC obtained at different exposure time. As it can be seen, for long exposure the cell exhibits a uniform distribution of the photoproduct, indicating irreversible Hb transition to the photoproduct.

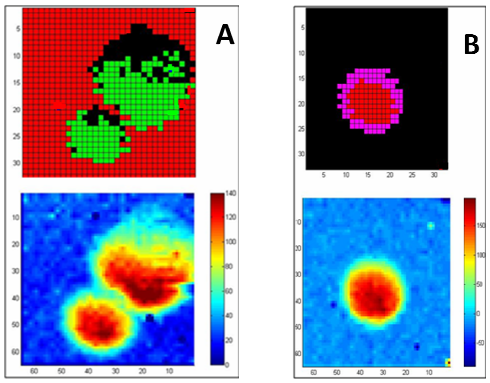

Figure 5.5: confocal Raman image using the Raman signal at 650 cm^{-1} and corresponding HCA image for healthy erythrocyte in the oxy state; A) during the data acquisition, B) for long exposure time.

The photoproduct does not seems a simple met form, but some more complex irreversible modification. Similar effects have been already reported for healthy erythrocytes exposed to radiation even at 785 nm and they have been attributed to protein denaturation, resulting in heme aggregation within the cell [266]. More study is required to assign the structural nature of the photoproduct.
Sample C retains the initial oxy state during the full measurement. No etherogeneity during the data acquisition of the Raman image, thus almost no photosensitivity is apparent in C samples(1024 s) (Figure 5.6).

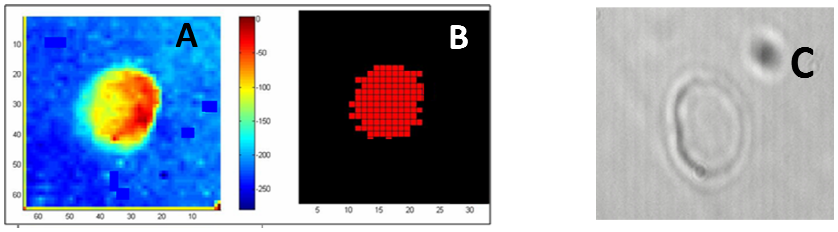

Figure 5.6: (A) confocal Raman image and (B) corresponding HCA image for C erythrocyte in the oxy state; (C) corresponding white-light transmission image.

On the contrary, sample S shows an instantaneous transformation (homogeneous Raman image) of the oxy form into a photoproduct, thus showing a high degree of photosensitivity (Figures 5.7 and 5.2, S).

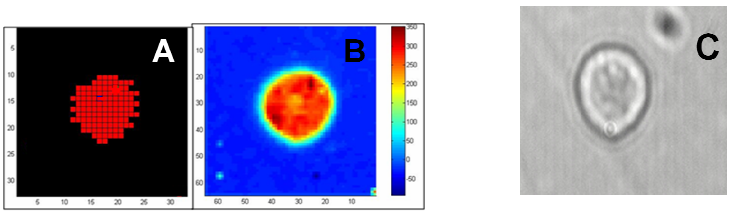

Figure 5.7: (A) HCA image, (B) confocal Raman image and (C) corresponding white-light transmission image, for S erythrocyte in the oxy state.

The sample C+S resembles much the C sample, indicating a low content of the S component.
The different degree of photosensibility, and the different aspect of the Raman images, suggest that Raman microscopy has a potential in the diagnosis of anemic S diseases.

Optical Tweezers

Optical Tweezers (OT), since their invention in the eighties, by Arthur Ashkin and colleagues [276] have emerged as an essential tool for manipulating single biological cells and performing sophisticated biophysical/biomechanical characterizations. Indeed the non-destructive trait and the versatility of the technique has provided a means of studying molecular mechanical properties [277, 278], cellular functions [279] and receptor-ligand interactions [280].
OT use the radiation pressure effect from a highly focused laser beam to trap and manipulate microscopic objects ranging in size from 50 nm to over 100 mm, such as latex beads or biological samples (cells, bacteria etc.) with forces of the order of few pN.

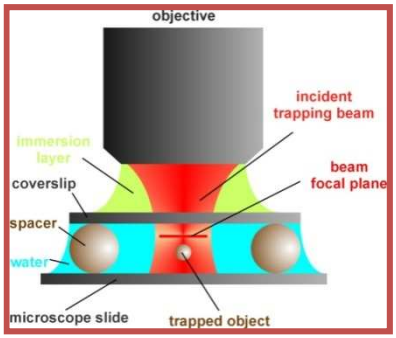

The tightly focused laser beam, through an objective lens (100x), exerts on dielectric particle essentially two forces:

- **Scattering force** that point in the direction of the incident light (z) and is proportional to the optical intensity;
- **Gradient force** that point in x-y plane towards the focus of the laser beam and is proportional to the gradient of light intensity.

For stable trapping, in all three dimensions, the gradient force must exceed that of the scattering force, otherwise the particle will be propelled away from the light source along the optical path.
Many experiments can benefit from the use of two or more optical traps to establish the experimental geometry. Multiple tweezers can be constructed trivially by increasing the number of laser light sources. Two optical beams are usually produced from a beam splitter. This requires that two light paths are controlled by different x-y

deflector systems. Two divergent counter- propagating beams were first used by Ashkin [281] to demonstrate the first actual trap. Constable et al. [282] tried to place two beams in an exactly counter-propagating way and they provided an equation to calculate the scattering force for these two beams. The gradient and scattering forces are shown in Figure 5.8 A.

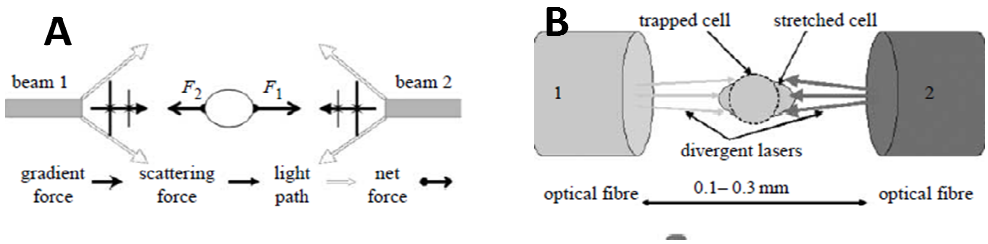

Figure 5.8 A: Schematic of gradient and scattering forces for two beams; **B:** Schematic of optical stretcher.

This technique is attractive for stretching single cells or single polymer molecules and is known as optical stretching (OS) and can be used to measure the elasticity of biological cells [283, 284], as shown in Figure 5.8 B. The advantages include that optical deformation does not require any kind of mechanical contact and covers a stress range previously inaccessible to cell elasticity measurements. Another advantage of using two divergent beams is to reduce photodamage or any two-photon-induced damage caused by a tightly focused light beam [285].

Mechanical characterization of healthy and diseased red blood cells

The deformation capability of RBC is mainly due to the elasticity of its membrane. The inner fluid of the RBC is purely viscous and has no elasticity. The RBC membrane is made of a lipidic bilayer, covering a protein network essentially composed of spectrin tetrameres linked by actin and protein 4.1 to form complex junctions (see Figure 5.9). These are the principal component of the cytoskeleton that underlies the RBC membrane accounting for its biconcave shape and its flexibility.

The mechanical properties of such structure has been largely investigated from both theoretical [286-288] and experimental [289-291] points of view. In the second case, the investigations relied on the measurement of cellular distortion in response to an applied mechanical stress.

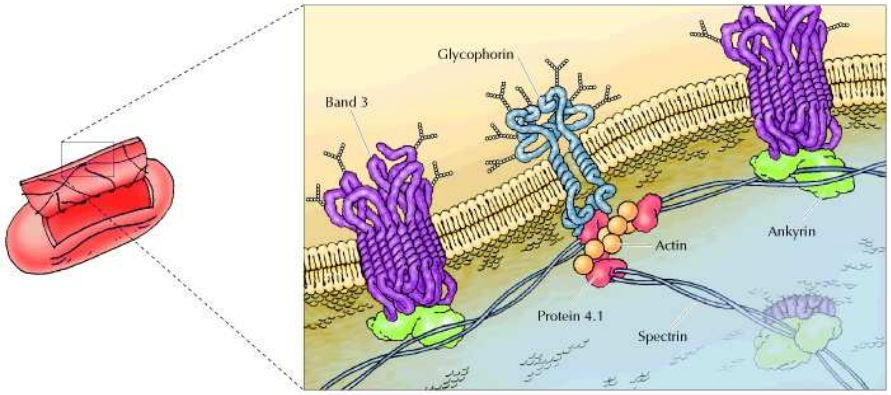

Figure 5.9: Sketch of the RBCs membrane: association of the erythrocyte cortical cytoskeleton with the plasma membrane.

Recently, Hénon et al. [291] have measured this parameter for normal human erythrocytes by using an Optical Tweezers system: in this case, calibrated forces were applied *via* small silica beads bound to the RBC membrane. The necessity to use such beads arises from the need to exert known forces, in order to obtain an absolute measurement of the RBC shear modulus.

Experimental set-up

For the mechanical characterization of RBCs, a double-trap system was created by applying a square voltage signal at a frequency of 1 kHz to a galvomirror (Cambridge Technology Incorporated, mod. 6220), placed on the optical path of the trapping beam. In such a way, the two optical traps shared the beam power and their relative distance was controlled by the voltage signal amplitude.

The Figure 5.10 illustrates the main components of experimental set-up of the *Laser Spectroscopy and Optical Manipulation laboratory* of Prof. A. Sasso, used for these experiments. The system is essentially a homemade micro-Raman system (inverted configuration), equipped with a second laser for the trapping and manipulation of the sample. The trapping laser was given by a Nd:YAG laser (1064 nm; Laser Quantum, Ventus 1064), emitting a maximum power of 3 W. It was tightly focused into the sample by an Olympus oil-immersion infinity corrected objective lens (100X, 1.4 N.A.). Back scattered light from the sample, collected and collimated by the same focusing objective, followed back the same path as the incident Raman probe, reaching finally an holographic notch filter. Finally, the Raman radiation was detected by using a front-illuminated charge-coupled device (Pixis 1024, Princeton Instruments, 1024×1024 pixels), thermoelectrically cooled at -70°C and placed at the spectrometer exit.

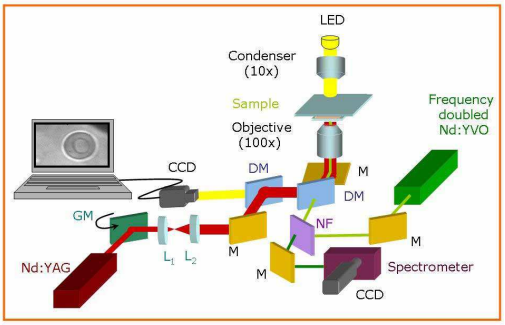

Figure 5.10: Experimental set-up of the combined Optical Tweezers and Raman Spectrometer: L, lens; M, mirror; DM, dichroic mirror; GM, galvomirror; NF, notch filter [240].

To precisely assign a wave number to each individual detector pixel, we used a trapped polystyrene latex beads (SERVA Electrophoresis), whose Raman peaks positions are accurately known [292].
A sketch of stretching mechanism is illustrated in Figure 5.11 A, while in the part B of the same figure some frames of a recorded video are shown. When the voltage applied to the galvomirror is zero, we have a conventional single trap: the RBC reaches a trapped position and floats slightly around it. As the distance between the two traps is increased, the RBC firstly starts orientating along the axis passing through the center of the two traps.

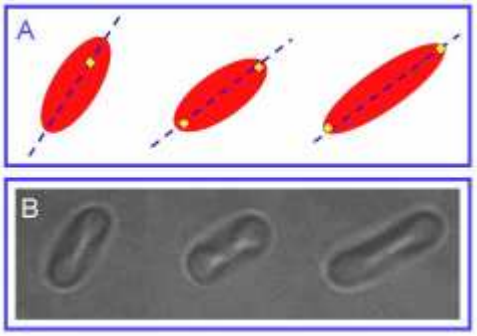

Figure 5.11: ***A****:* Sketch of the stretching procedure used for the present investigation. **B**: Same frames of a video recorded during the stretching of a normal RBC [240].

After the RBC is fully aligned, it begins to be stretched.
For a given trapping laser power, was applied an increased stress to the membrane by slowly incrementing the distance between the two traps. The cell become elongated, and its diameter D increases in the direction of the applied force. RBC elongation (D-

D_0) was extracted by hand, using an image software (NIH ImageJ). In particular, were recorded 10 images for each erythrocyte elongation. From each image was estimated the major axis of the RBC shape and computed the average length over all the 10 frames. The final accuracy of D is » 200 nm. By varying the laser power P, we collect a set of images of the same cells submitted to different forces, as shown, for instance in Figure 5.11 B.
In the small deformation regime of the RBC membrane, which has a constant area in a first approximation, it is possible to demonstrate that [291]:

$$D\text{-}D_0 = F/k$$

where ($D - D_0$) is the diameter elongation, F is the applied force and k is the elastic shear modulus of the membrane. The force exerted on a trapped object depends on its size and shape, and on the refractive indices of the object and the surrounding medium. It is proportional to the incident laser power.

Sample preparation

Fresh blood was obtained by a clinic case in a family (mother, father and daughter, respectively heterozygous for HbS, HbC and Hb C+S). Control samples were drawn from normal adults. The samples were kindly provided by the consenting patients of Dr. Michela Grosso (Department of Biotechnology and Biomedicine of University of Naples "Federico II"). Samples were prepared according to the following procedure: blood (5 µl) anticoagulated by K-EDTA, was diluted in 10 ml of isotonic aqueous NaCl solution and 0.5 ml of human albumin (used as membrane protection). Few microliters of this solution were transferred, within few minutes, in a home-made chamber.

Results

Response to applied stretching for normal and abnormal RBCs

Our investigation was performed by stretching single of healthy and abnormal erythrocytes by using a double OT system. In Figure 5.12 is reported the RBC elongation (ΔL) as a function of the applied force (pN) for healthy and anemic RBCs. Each value results from an average of 15 measurements performed on different cells. The error bars correspond to the standard deviation. The data plotted in Figure 5.12 reveal a small different mechanical response of normal cells with respect to anemic RBCs (for erythrocytes S and C+S were observed the same mechanical properties). From a linear fit of the experimental data, it was possible to estimate the ratio of the shear modulus k for the three kinds of cells. These results were: k_n/k_c=0.77±0.06 and k_n/k_{c+s}=0.95±0.05. If we assume k_n=2.5±0.4 pN/µm, as found by Hénon et al.[291], we obtain k_c=3.2±0.8 pN/µm for yyerythrocytes affected by HbC and k_{c+s} =2.6±0.9 pN/µm for those with HbC+S. Therefore the trend of rigidity is as follows: healhty< S =C+S< C.

These results confirm medical predictions for which the deformability is known to be reduced in patients with sickle cell anemia (SCA and SS genotype) and sickle cell hemoglobin C disease (SCC; SC genotype) [293-295].

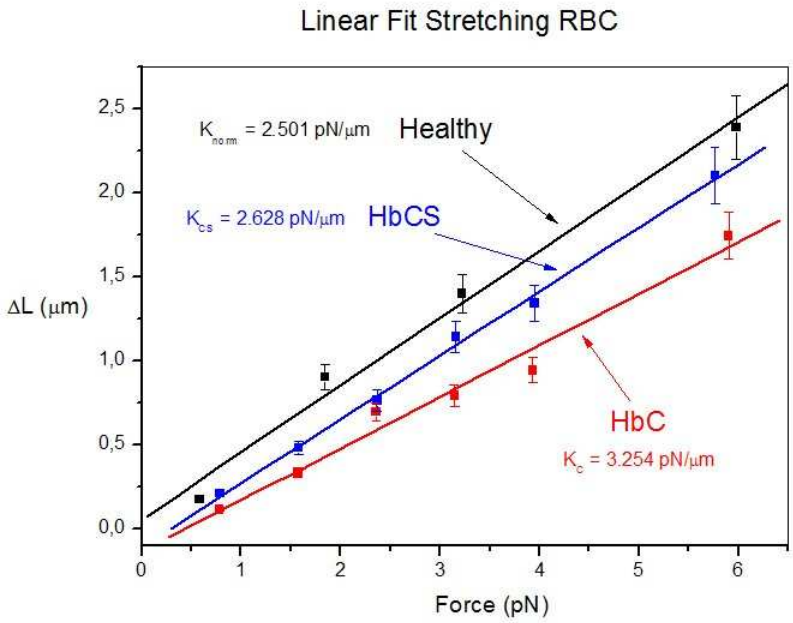

Figure 5.12: Response to applied stretching for healthy and abnormal RBCs.

Conclusion

In this chapter, it has been showed the feasibility of Raman microscopy, in conjunction with optical tweezers, a) to monitor *ex vivo* and non-invasively the biochemical changes and b) to investigate cell elastic properties, inside living single cells. Results of these two methodologies suggest the possibility to individuate different properties between HbA, S and C. Ultimately, the Raman images technology could help to distinguish between C and S anemia, and potentially to evaluate the expression ratio between HbS and HbC in C+S samples.

Moreover these findings demonstrate that these two methodologies are particularly promising for a new molecular diagnostic approach in Hb-related blood diseases and at the same time, they describe the potentiality in using these techniques for a rapid screening of normal and diseased cells.

Chapter 6

Conclusions

The main scope of research work has been the elucidation of the molecular mechanism undergoing un-known physiological functions of tetrameric Hbs, both recombinant and natural, both from human origin and Antarctic fish.
To analyze these systems a twofold methodological approach was adopted:

- **Molecular** one, based on a combined crystallographic (microspectroscopy UV / VIS and Raman spectroscopy, X-ray diffraction), spectroscopic (UV / VIS, and Raman) and computational (MD) study, both on single crystals and solutions;
- **Cellular** one, *ex vivo*, based on Raman imaging and optical tweezers study of human erythrocytes.

In particular, in the context of the **molecular** approach, my Ph.D. work was focused on the elucidation of two still unsolved problems in the chemistry of tetrameric Hbs:
1) the role of the bis-histidyl heme coordination in the Hb function and oxidation process;
2) the role of the tertiary and quaternary structure in the modulation of the Root effect.

1) Role of bis-histidyl adducts in tetrameric hemoglobins

With the aim to characterize both the structural determinants and details on the mechanism of hemichrome formation in tetrameric Hbs, the work strategy was divided into two fields of investigation:
1a) a comparative experimental (spectroscopic and crystallographic) / computational study of the β subunits of human hemoglobin (β-HbA) and of Hb from Antarctic fish *Trematomus bernacchii* (β-HbTb), obtained *via* recombinant production (in collaboration with Prof. M.L. Tutino).
1b) a crystallographic /spectroscopic study of hemichrome formation in AfHb from from the major component of *Trematomus newnesi* (HbITn) and in Hb from sub-Antarctic fish *Eloginops maclovinus*.

1a) Comparative study: HbA vs HbTb

The recombinant form of β-HbTb, produced in recombinant *E. coli*, self assembles, as the β-chain of human hemoglobin [120, 142], to form a β_4 homotetramer (β_4-HbTb). The oxidation pathway of β_4-HbTb solutions, induced by air-exposure of the carbomonoxy form, monitored *via* electronic spectroscopy, ends to a hemichrome state, passing through an aquo-met intermediate. Furthermore, differently from $\alpha_2\beta_2$ heterotetramer [58, 75], the reduction of β_4-HbTb forms a bis-histidyl adduct also in the ferrous state (hemochrome). The comparative Molecular Dynamics (MD) study of

the HbTb and HbA isolated β-chains in the hemichrome state indicates that the two proteins maintain the correct globular folding during the simulation, thus suggesting that the presence of the bis-hystidyl complex does not affect the overall stability of the isolated HbTb β-chain and is also compatible with the sequence of β-HbA. However the analysis of the fluctuations of protein residues during the simulations, shows that in β-HbTb the CD region displays a pronounced mobility, in comparison to β-HbTb. This result is somewhat expected and it is related to cold-adaptation [205]. On the contrary, in the human β-chain the E helix and the FG corner display a larger fluctuation, which could have a role in the decreased relative stability of the bis-His adduct with respect to exogenous ligation

These findings are in perfect agreement with the X-ray crystallographic characterization of β-chain homotetramer of human hemoglobin in the ferric state. X-ray structure of β_4-HbA crystals (solved at 2.1 Å resolution), grown from the solution of protein oxidized by potassium ferricyanide (containing a mixture of hemichrome /aquo-met state) hosts only hexacoordinate high spin (HS) aquo-met coordination, whereas the bis-His adduct does not co-crystallize. Particularly interesting is the presence of two disulfide bridges between Cys112(G14) residues at the $\beta_1\beta_4$ ($\beta_2\beta_3$) interfaces, absent in the structures of deoxygenated and of carbomonoxy forms [139, 140], and that seem not to influence the heme coordination in ferric-β_4-HbA. All these data, seems to indicate the β chain of HbA is intrinsically less prone to form the bis-histidyl adduct. The comparative analysis of β-chain from HbA and from HbTb clearly shows that, differently from human hemoglobin, bis-histidyl coordination is an intrinsic property of the β subunit of HbTb, independently of the aggregation state of the protein (β-HbTb, β_4-HbTb or $\alpha_2\beta_2$-HbTb).The determination of the three-dimensional structure of ferric β_4-HbTb or the hybrid α_2-HbA/β_2-HbTb could expand our understanding of this different behavior and will shed further light on the contribution of α / β assembly in modulating the Fe(III)β coordination.

1b) *Crystallographic / spectroscopic study of hemichrome formation in HbITn and Hb1Em*

Previous studies on the oxidation pathway of the carbomonoxy form of HbITn (PDB code 1T1N [207]) at several times of air exposure: a) three hours air exposure in solution [74], b) seven days exposure in solution [43], c) thirdy days and one year air-exposed in the crystal state (unpublished) offered a clear observation that, in Hbs from Antarctic fish, α and β-chains follow distinct but interdependent oxidation pathway. These X-ray structures are characterized by alternative coordination (penta- and hexa-coordinated species) at the β-hemes. In order to simplify the chemical systems, the fully oxidized by potassium ferricyanide (ox-HbITn) form has been crystallized. During this thesis, diffraction data at 1.65 Å resolution have been analyzed, refining a structure that represents the first reference of a completely ferric HbITn structure.

The inspection of the electron density maps clearly indicates that the iron, at β-heme, forms a complex bis-histidine, showing a well ordered single coordination and

confirming the goodness of the strategy and of the chemical protocol used (addition of ferricyanide). Therefore, ox-HbITn is a model for decoupling the density of bis-His complex from alternative coordination (penta- and hexa-coordinated species) at heme groups, particularly interesting for future investigations of Raman-assisted crystallography.

Eleginops maclovinus (Em) is a member of non-Antarctic notothenioid species, belonging to the family *Eleginopidae* and is the only species of its genus. Hb1Em, a tetrameric Root effect-Hb is the first sub-Antarctic fish Hb (sub-AfHb) to be crystallized. The study of Hb1Em single crystals by micro Resonance Raman (RR) spectroscopy, with 514.5 nm excitation, has shown that the ferric form contains hexa-coordinated low-spin hemichrome [216]. Therefore, we extended this observation, typical of Antarctic fish Hbs, also to sub-Antarctic fish.

2) Role of the tertiary and quaternary structure in the modulation of the Root effect

In order to elucidate the role of the tertiary and quaternary structure in the modulation of the Root effect, the work strategy was divided into two fields of investigation:

2a) Equilibrium and crystallographic studies of oxygen (O_2) and carbon monoxide (CO) binding to the T-state HbTb crystals at pH 6.2 and 8.4.

2b) Combined crystallographic (X-ray diffraction)/ Resonance Raman (RR) microspectroscopic study on the mechanism of nitric oxide (NO) binding and release to the T-state crystals of HbTb at two different pHs.

The choice of these pH values is justified by the known tertiary structural differences of their X-ray structure in deoxygenated forms at different pH values.

2a) Oxygen binding study (in collaboration with Prof. Andrea Mozzarelli at University of Parma) to deoxygenated HbTb crystals at two different pHs (6 and 8.4) performed by VIS microspectroscpy has shown that the low -to- high pH transition induces 2-3 fold increase in oxygen affinity, highlighting that the Root effect is still present in T-state Hb, and that about half of the cooperativity present in solution is retained in crystals grown at basic pH, but not at pH 6. This indicates that the cooperativity can be elegantly switched on by the only changes in tertiary structure, at quaternary structure blocked (by the crystalline matrix). Attempts to obtain a fully CO form in a T-state HbTb structure at pH 8.4 that could completely explain the origin of cooperativity, failed, due to the inability to operate experimentally with CO cylinders, during crystal handling and during the collection of X-ray diffraction data. Indeed the crystal structure obtained (solved at 2.2 Å of resolution) shows a partial CO binding, only at the α-heme, due to oxidative phenomena, that are very fast in HbTb [75]. Some clue on the possible regions that are responsible for such a high modification of the heme upon binding at the T state can be indirectly extracted by another study of this thesis, NO reactivity studies to T-state HbTb crystals.

2b) Combined X-ray crystallographic/RR micro-spectroscopic studies on the NO binding to the T-state HbTb crystals, at pH 6.2 and 8.4., were performed.

Initially, experiments of NO soaking to deoxygenated HbTb crystals, monitored in house *via* Raman microscopy exciting at 514 nm, have been evidenced a hexa-coordinated Hb in the fully ligated form. Despite the reproducibility of the soaking procedure, monitored via RR, X-ray diffraction data collection (in-house at 1.9 Å resolution, for crystals at pH 8.4 and at synchrotron ELETTRA (Trieste) at 1.5 Å resolution, for crystals at pH 6.2) resulted only in a partial NO coordination limited at the α-subunits, due to oxidative denitrosilation. To limit oxidative phenomena a protective environment (a mixture of ascorbate and catalase) was used. But, even under this oxygen-free conditions, again a partial binding was obtained. The simultaneous X-ray data collection, on T-state nitrosyl-HbTb crystals at pH 6, assisted by online Raman acquisition, at SLS synchrotron (Switzerland), clearly indicate an X-ray induced NO-photodissociation. X-ray diffraction collections were performed at several steps of dissociation (at different X-ray dose). In order to collect a fully nitrosylated form, a 2 % of the available X-ray flux were used, corresponding to a 2.5 Å resolution, despite the crystal diffracted better. Electron density maps from these moderate resolution data shows that almost only the β-subunits undergoes photodissociation, whereas α-subunits are still in a nitrosyl state. In agree with RR analysis, the α-heme groups are hexa-coordinated. The comparison between fully ligated and photolized structure provides an elegant evidence of heme-heme communication mediated *via* CDα region. Interestingly, our Raman microscopy evidence of X-ray induced NO-photodissociation for Hb from *Trematomus bernacchii* can have a general impact, and thus explaining the surprisingly low number of crystal structures of nitrosyl Hbs deposited in the PDB.

This combined crystallographic and spectroscopic method has provided 1) an experimental protocol to detect X-ray induced NO-photodissociation on protein crystals, and 2) a quantitative information on the relative Raman cross-section of deoxygenated and nitrosylated Hbs, useful to evaluate the degree of NO-photodissociation for future studies.

Cellular study

Raman imaging techniques and a system of Optical Tweezers (OT) have been used to characterize, *ex vivo*, heterozygous normal and C/S anemic red blood cells (RBCs) (affected from HbS (β6Glu → Val), HbC (β6Glu → Lys) and HbSC), at single cell level. Some significant difference in the functionality of the anemic cells with respect to normal erythrocytes have been highlighted. The four kinds of cells, in oxygenated forms, present a different photo-sensibility. In particular in the Raman spectra of the S cells, there is an instantaneous appearance of a photoproduct with a high bands with a relative intensity inversed with respect to healthy cells. It has been, finally, measured the membrane shear modulus. The results, obtained in this thesis, confirm medical predictions regarding anemia, such as higher rigidity of sickle erythrocytes. Indeed our experiments exhibit this trend of rigidity: healhty< S =C+S< C. In conclusion, the findings of this thesis shown that Raman micro-spectroscopy analysis combined with

the use of Optical Tweezers offers enormous potential in the diagnosis and for a rapid screening of normal and diseased cells.

APPENDIX

In order to reproduce the Raman imaging experiments (performed at the University of Twente), during the last year of my Ph.D. work I have also been involved in the assembly of a Kr^+-ion laser (Coherent, Innova 300C) providing the excitation wavelength of 647.1 nm, in our confocal Raman microscope (Jasco, NRS-3100).
Here we report the comparative Raman microscopy study, with 514 and 647 nm excitation line, of Hg^{2+} binding at bovine insulin crystals a) to test laser line at 647 nm and b) to define a practical protocol to the detection of Hg^{2+} incorporation into a protein crystals *via* Raman microscopy.

Hg^{2+}binding to proteins

Both organic and inorganic mercury compounds, such as Hg^{2+},methyl and ethyl-mercury, are well known as toxic agents in several poisoning mechanisms. Mercury toxicity mechanisms are essentially linked to two major kinds of actions:

- Protein binding (enzymes, receptors, structural proteins etc…)
- Interactions with nucleic acids and/or basis.

Among the multiple possible interactions of mercury compounds, certainly the most common is the interaction with sulfur atoms of cysteine residues, resulting in relatively stable Hg-Cysteine complexes. Inorganic mercury tends to form both free $^+$Hg-S-Cys and Cys-S-Hg-S-Cys complexes depending on proximity of cysteines; organic compounds, instead, because of the presence of the alkane chain, do not form bridges but only H_3C-Hg-Cys- (in case of methyl-Hg) in mammalian Thioredoxin system [296].

Bovine insulin is composed of two polypeptide chains: chain A has 21 amino acids and chain B has 30 amino acids. Two disulfide bridges (residues A7 to B7, and A20 to B19) covalently tether the chains, and chain A contains an internal disulfide bridge (residues A6 to A11).

Crystallization, reduction and $HgCl_2$ soaking

Best crystallization conditions of bovine insulin were 5% Acetone, 50mM Na/Cit pH 6.3, 3 mM $ZnCl_2$ and 5% Tacsimate. As disulfide reducing agent we used 80mM TCEP (Tris2-carboxy-ethylphosphine-chloride) at pH7.0. Reduced crystal were preserved by air oxidation taking them into an oxygen free atmosphere (glove box at less than 1 ppm O_2). $HgCl_2$ 20mM was added (overnight) to obtain soaking into crystals.

Raman spectra analysis excitation at 514 and 647 nm

Raman spectra analysis was performed on native crystals of bovine insulin, on TCEP-reduced and on mercury soaked crystals (to take into account possible background interferences, mother liquor was analyzed too (fig. 1)).The native crystals show a 1659 cm^{-1} peak which refers to the amide I mode in α-helix insulin secondary structure [297] and a 1680 cm^{-1} shoulder related to β-sheet secondary structure [298]; these bands shift upon TCEP-induced reduction and α-helixces are replaced by a single β-sheet marker band at 1673 cm^{-1}. This spectral change is assigned to an alpha-helix to

beta-sheet transition occurring upon reduction of disulfide bridges, similarly to what happens for human insulin [298].

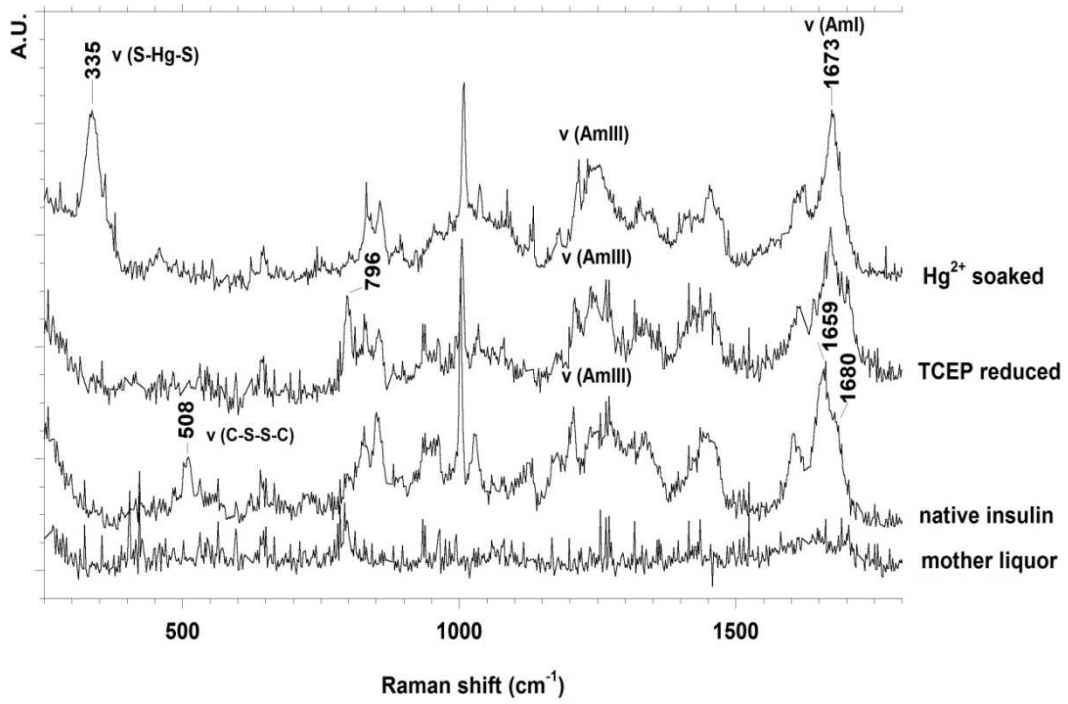

Figure 1 - Raman spectra of bovine insulin crystals: native insulin shows a clear 508 cm^{-1} band referred to S-S stretching and a 1659 cm^{-1} band related to amide I modes in alpha-helix secondary structure; TCEP reduction produces the disappearance of the 508 cm^{-1} band due to S-S reduction to SH groups; this involves an alpha-helix to beta-sheet transition which is noticeable due to presence, in both TCEP and Hg soaked spectra, of a single beta-sheet related band at 1673 cm^{-1}. A band at 796cm^{-1} is visible only in TCEP reduced spectrum and should probably be attributable to TCEP itself.

This amide I feature is still present upon Hg^{2+} soaking, indicating that mercuration does not affect secondary structure. The 508 cm^{-1} band, is in a region (500-550 cm^{-1}) typically assigned to -S-S- stretching [299]. The value of the -S-S- stretching is related to a gauche-gauche-gauche conformation of the three torsional angles in the C-S-S-C groups. Other frequencies would correspond to different conformations (with g for gauche and t for trans; reference value in literature): 510 cm^{-1} for ggg, 525 cm^{-1} for ggt and 540 cm^{-1}tgt. This 508 cm^{-1}band clearly visible in native crystal spectrum, becomes featureless in the reduced form, due to S-S reduction to SH group.

After addition of 20 mM $HgCl_2$, overnight, a huge new band appears at 335 cm^{-1}(fig. 3.1). This band, according to literature on cysteine crystals and solutions [300], is assigned to **-S-Hg-S-** stretching. This is a valuable reference for simultaneous Hg^{2+} binding to two Cys residues. This band has a very high intensity (comparable to the Amide I), though only 3 of these-S-Hg-S- bridges can be formed per insulin molecule,

compared to fifty amide bonds. This high Raman intensity of -S-Hg-S- band is related to the heavy atoms involved (Hg and S) that are very polarizable, thus producing very high Raman cross-sections. Finally, a single band at 796 cm^{-1}, exclusively present in TCEP reduced spectrum, is with high probability referred to TCEP itself. It can be assigned to a P-C stretching, usually expected around 770 cm^{-1}.
To confirm the analysis, and to generalize the Raman results obtaining exciting with a 514 nm line, we used a second laser line at 647 nm to compare the results (Figure 2).
Spectra obtained exciting with 514 and 647nm are extremely similar and both show the same very intense band at *335 cm^{-1}*(Figure 2), confirming, therefore, assembly efficiency .

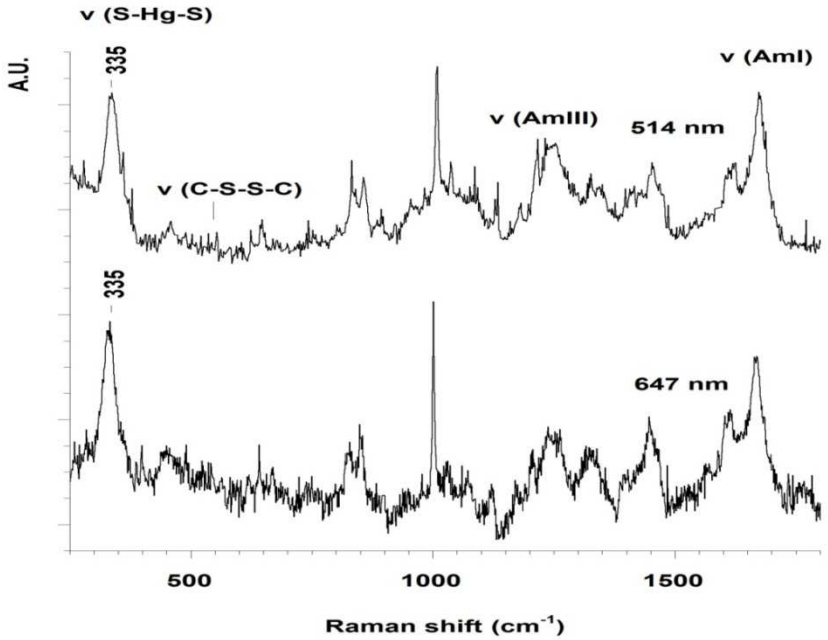

Figure 2 – Comparison of Raman spectra of Hg^{2+} soaked crystals obtained using different laser lines: 514 nm (as also shown in fig. 3.1), compared to 647 nm laser line spectra. No appreciable differences are visible and, sustaining previous results, Hg 335 cm^{-1} band is still present with almost the same very high intensity.

This study provided a reference for the **S-Hg-S** stretching in proteins. Nevertheless, it is worth mentioning that in case of isolated Cys residues we should expect a different stretching frequency related to the **-S-Hg^{+}** groups. Therefore, some further work on native crystals from proteins with free isolated cysteines is required to have this marker, thus obtaining a comprehensive picture of the Raman markers for Hg^{2+} binding.

References

1. Monod, J., Wyman, J. & Changeux, J. P. (1965) On the Nature of Allosteric Transitions: A Plausible Model, *J Mol Biol. 12*, 88-118.

2. Kosmachevskaya, O. V. & Topunov, A. F. (2009) Hemoglobins: Diversity of structures and functions, Applied Biochemistry and Microbiology. *45*, 563-587

3. Wittenberg, J. B., Bolognesi, M., Wittenberg, B. A. & Guertin, M. (2002) Truncated hemoglobins: a new family of hemoglobins widely distributed in bacteria, unicellular eukaryotes, and plants., *J. Biol. Chem. 277*, 871–874

4. Kundu, S., Trent, J. T., 3rd & Hargrove, M. S. (2003) Plants, humans and hemoglobins., *Trends Plant Sci. 8*, 387-393.

5. Hankeln, T., Ebner, B., Fuchs, C., Gerlach, F., Haberkamp, M., Laufs, T. L., Roesner, A., Schmidt, M., Weich, B., Wystub, S., Saaler-Reinhardt, S., Reuss, S., Bolognesi, M., De Sanctis, D., Marden, M. C., Kiger, L., Moens, L., Dewilde, S., Nevo, E., Avivi, A., Weber, R. E., Fago, A. & Burmester, T. (2005) Neuroglobin and cytoglobin in search of their role in the vertebrate globin family., *J. Inorg. Biochem. . 99*, 110–119.

6. Trent, J. T., III, & Hargrove, M. S. (2002) A ubiquitously expressed human hexacoordinate hemoglobin. , *J. Biol. Chem. 277*, 19538–19545.

7. Perutz, M. F. (1987) Molecular anatomy, physiology, and pathology of hemoglobin., *Molecular Basis of Blood diseases*, 127-177.

8. Brittain, T. (2005) Root effect hemoglobins, *J Inorg Biochem. 99*, 120-9.

9. Fermi, G., Perutz, M. F., Shaanan, B. & Fourme, R. (1984) The crystal structure of human deoxyhaemoglobin at 1.74 A resolution, *J Mol Biol. 175*, 159-74.

10. Derewenda, Z., Dodson, G., Emsley, P., Harris, D., Nagai, K., Perutz, M. & Renaud, J. P. (1990) Stereochemistry of carbon monoxide binding to normal human adult and Cowtown haemoglobins, *J Mol Biol. 211*, 515-9.

11. Bohr, C. (1903) Theoretische Behandlung der quantitativen Verhaltnis bei der Sauerstoffaufnahme des Hamoglobin, *Zentr Physiol. 17*, 682–689.

12. Hill, A. V. (1910) The possible effects of the aggregation of the molecules of haemoglobin on its dissociation curves., *J Physiol. 40*, iv–vii.

13. Baldwin, J. & Chothia, C. (1979) Haemoglobin: the structural changes related to ligand binding and its allosteric mechanism, *J Mol Biol. 129*, 175-220.

14. Perutz, M. F. (1970) Stereochemistry of cooperative effects in haemoglobin, *Nature. 228*, 726-39.

15. Imai, K. (1982) Allosteric effects in hemoglobin., *Cambridge University Press, Cambridge.*

16. Root, R. W. (1931) The respiratory function of the blood of marine fishes, *Biol Bull. 61*, 427-456.

17. Perutz, M. F., Fermi, G., Luisi, B., Shaanan, B. & Liddington, R. C. (1987) Stereochemistry of cooperative mechanisms in hemoglobin, *Cold Spring Harb Symp Quant Biol. 52*, 555-65.

18. Minton, A. P. & Imai, K. (1974) The three-state model: a minimal allosteric description of homotropic and heterotropic effects in the binding of ligands to hemoglobin, *Proc Natl Acad Sci U S A. 71*, 1418-21.

19. Sawicki, C. A. & Gibson, Q. H. (1976) Quaternary conformational changes in human hemoglobin studied by laser photolysis of carboxyhemoglobin, *J Biol Chem. 251*, 1533-42.

20. Yonetani, T., Park, S. I., Tsuneshige, A., Imai, K. & Kanaori, K. (2002) Global allostery model of hemoglobin. Modulation of O(2) affinity, cooperativity, and Bohr effect by heterotropic allosteric effectors, *J Biol Chem. 277*, 34508-20.

21. Marden, M. C., Kister, J., Bohn, B. & Poyart, C. (1988) T-state hemoglobin with four ligands bound, *Biochemistry. 27*, 1659-64.

22. Jayaraman, V. & Spiro, T. G. (1995) Structure of a third cooperativity state of hemoglobin: ultraviolet resonance Raman spectroscopy of cyanomethemoglobin ligation microstates, *Biochemistry. 34*, 4511-5.

23. Perrella, M., Benazzi, L., Shea, M. A. & Ackers, G. K. (1990) Subunit hybridization studies of partially ligated cyanomethemoglobins using a cryogenic method. Evidence for three allosteric states, *Biophys Chem. 35*, 97-103.

24. Silva, M. M., Rogers, P. H. & Arnone, A. (1992) A third quaternary structure of human hemoglobin A at 1.7-A resolution, *J Biol Chem. 267*, 17248-56.

25. Smith, F. R., Lattman, E. E. & Carter, C. W., Jr. (1991) The mutation beta 99 Asp-Tyr stabilizes Y--a new, composite quaternary state of human hemoglobin, *Proteins. 10*, 81-91.

26. Mueser, T. C., Rogers, P. H. & Arnone, A. (2000) Interface sliding as illustrated by the multiple quaternary structures of liganded hemoglobin, *Biochemistry. 39*, 15353-64.

27. Safo, M. K. & Abraham, D. J. (2003) X-ray crystallography of hemoglobins, *Methods Mol Med. 82*, 1-19.

28. Safo, M. K. & Abraham, D. J. (2005) The enigma of the liganded hemoglobin end state: a novel quaternary structure of human carbonmonoxy hemoglobin, *Biochemistry. 44*, 8347-59.

29. Verde, C., Lecointre G. & G., D. P. (2007) The phylogeny of polar fishes and the structure, function and molecular evolution of hemoglobin., *Polar Biology. 30* 523-539.

30. Romisch, K. & Matheson, T. (2003) Cell biology in the Antarctic: studying life in the freezer, *Nat Cell Biol. 5*, 3-6.

31. Ruud, J. T. (1954) Vertebrates without erythrocytes and blood pigment, *Nature. 173*, 848-50.

32. Di Prisco, G. & Tamburrini, M. (1992) The hemoglobins of marine and freshwater fish: the search correlations with physiological adaptation. , *Comp Biochem Physiol. 102*, 661-671.

33. di Prisco, G. (1998) Molecular adaptations of Antarctic fish haemoglobins. In Fishes of Antarctica: Biological Overview *(di Prisco G., Pisano E. & Clark A., eds)*, pp. 339–353. Springer, Milan.

34. di Prisco, G., D'Avino, R., Caruso, C., Tamburrini, M., Camardella, L., Rutigliano, B., Carratore, V. & Romano, M. (1991) The biochemistry of oxygen transport in red-blooded Antarctic fish., *In Biology of Antarctic Fish. (di Prisco, G., Maresca, B. & Tota, B., eds)*, pp. 263–281. Springer-Verlag, Milan.

35. DeVries, A. L. & Cheng, C. H. C. (2005) *in The Physiology of Polar Fishes, (Farrell, A.P. and Steffensen, J.F., Eds.) Fish Physiology. 22*, pp. 155-201. Elsevier Academic Press, San Diego.

36. DeVries, A. L. (1988) The role of glycopeptide and peptide antifreeze in the freezing avoidance of Antarctic fishes, *Comp Biochem Physiol. 90B* 611–621.

37. DeVries, A. L. (1971) Glycoproteins as biological antifreeze agents in Antarctic fishes, *Science. 172*, 1152-1155.

38. Eastman, J. T. (1993) Antarctic fish biology: evolution in a unique environment. , *Academic Press, San Diego, CA*, pp: 322.

39. Jensen, F. B., Fago, A. & Weber, R. E. (1998) Hemoglobin structure and function, *In Fish Physiology, vol. 17, Fish Respiration. (ed. S. F. Perry and B. Tufts)* pp. 1–40. San Diego, CA: Academic Press.

40. Weber, R. E. (1990) Functional significance and structural basis of multiple hemoglobins with special reference to ectothermic vertebrates, *In Animal Nutrition and Transport Processes. 2. Transport, Respiration and Excretion: Comparative and Environmental Aspects*, (ed. J.-P. Truchot and B. Lahlou), pp. 58-75. Basel: Karger.

41. Verde, C., Parisi, E. & di Prisco, G. (2006) The evolution of thermal adaptation in polar fish, *Gene. 385*, 137-45.

42. Bonaventura, C., Crumbliss, A. L. & Weber, R. E. (2004) New insights into the proton-dependent oxygen affinity of Root effect haemoglobins, *Acta Physiol Scand. 182*, 245-58.

43. Riccio, A., Vitagliano, L., di Prisco, G., Zagari, A. & Mazzarella, L. (2002) The crystal structure of a tetrameric hemoglobin in a partial hemichrome state, *Proc Natl Acad Sci U S A. 99*, 9801-6.

44. Vitagliano, L., Bonomi, G., Riccio, A., di Prisco, G., Smulevich, G. & Mazzarella, L. (2004) The oxidation process of Antarctic fish hemoglobins, *Eur J Biochem. 271*, 1651-9.

45. Vergara, A., Franzese, M., Merlino, A., Vitagliano, L., Verde, C., di Prisco, G., Lee, H. C., Peisach, J. & Mazzarella, L. (2007) Structural characterization of ferric hemoglobins from three antarctic fish species of the suborder notothenioidei, *Biophys J. 93*, 2822-9.

46. Yokoyama, T., Chong, K. T., Miyazaki, G., Morimoto, H., Shih, D. T., Unzai, S., Tame, J. R. & Park, S. Y. (2004) Novel mechanisms of pH sensitivity in tuna hemoglobin: a structural explanation of the root effect, *J Biol Chem. 279*, 28632-40.

47. Berisio, R., Lamzin, V. S., Sica, F., Wilson, K. S., Zagari, A. & Mazzarella, L. (1999) Protein titration in the crystal state, *J Mol Biol. 292*, 845-54.

48. Yang, F. & Phillips, G. N., Jr. (1996) Crystal structures of CO-, deoxy- and met-myoglobins at various pH values, *J Mol Biol. 256*, 762-74.

49. Nar, H., Messerschmidt, A., Huber, R., van de Kamp, M. & Canters, G. W. (1991) Crystal structure analysis of oxidized Pseudomonas aeruginosa azurin at pH 5.5 and pH 9.0. A pH-induced conformational transition involves a peptide bond flip, *J Mol Biol. 221*, 765-72.

50. Root R.W. & L., I. (1941) The equilibrium between hemoglobin and oxygen in whole and hemolyzed blood of the tautog, with a theory of the Haldane effect, *Biol Bull 81*, 307–323.

51. Wittenberg, J. B. & Haedrich, R. L. (1974) The choroid rete mirabile of the fish eye. II. Distribution and relation to the pseudobranch and to the swimbladder rete mirabile, *Biol Bull. 146*, 137-56.

52. Eastman, J. T. (1988) Ocular morphology in Antarctic notothenioid fishes *J Morphol 196*, 283–306.

53. Camardella, L., Caruso, C., D'Avino, R., di Prisco, G., Rutigliano, B., Tamburrini, M., Fermi, G. & Perutz, M. F. (1992) Haemoglobin of the antarctic fish Pagothenia bernacchii. Amino acid sequence, oxygen equilibria and crystal structure of its carbonmonoxy derivative, *J Mol Biol. 224*, 449-60.

54. Tame, J. R., Wilson, J. C. & Weber, R. E. (1996) The crystal structures of trout Hb I in the deoxy and carbonmonoxy forms, *J Mol Biol. 259*, 749-60.

55. Mazzarella, L., Bonomi, G., Lubrano, M. C., Merlino, A., Riccio, A., Vergara, A., Vitagliano, L., Verde, C. & di Prisco, G. (2006) Minimal structural requirements for root effect: crystal structure of the cathodic hemoglobin isolated from the antarctic fish Trematomus newnesi, *Proteins. 62*, 316-21.

56. Mylvaganam, S. E., Bonaventura, C., Bonaventura, J. & Getzoff, E. D. (1996) Structural basis for the root effect in haemoglobin, *Nat Struct Biol. 3*, 275-83.

57. Mazzarella, L., Vergara, A., Vitagliano, L., Merlino, A., Bonomi, G., Scala, S., Verde, C. & di Prisco, G. (2006) High resolution crystal structure of deoxy hemoglobin from Trematomus bernacchii at different pH values: the role of histidine residues in modulating the strength of the root effect, *Proteins. 65*, 490-8.

58. Vergara, A., Vitagliano, L., Merlino, A., Sica, F., Marino, K., Verde, C., di Prisco, G. & Mazzarella, L. (2010) An order-disorder transition plays a role in switching off the root effect in fish hemoglobins, *J Biol Chem. 285*, 32568-75.

59. Unzai, S., Imai, K., Park, S.-Y., Nagai, K., Brittain, T. & Tame, J. R. H. (2008) Mutagenic Studies on the Origins of the Root Effect in *Dioxygen Binding and Sensing Proteins* (Bolognesi, M., Prisco, G. & Verde, C., eds) pp. 67-78, Springer Milan.

60. Parkhurst, L. J., Goss, D. J. & Perutz, M. F. (1983) Kinetic and equilibrium studies on the role of the .beta.-147 histidine in the Root effect and cooperativity in carp hemoglobin, *Biochemistry. 22*, 5401-5409.

61. Merlino, A., Vergara, A., Sica, F., Aschi, M., Amadei, A., Di Nola, A. & Mazzarella, L. (2010) Free-energy profile for CO binding to separated chains of human and Trematomus newnesi hemoglobin: insights from molecular dynamics simulations and perturbed matrix method, *J Phys Chem B. 114*, 7002-8.

62. Laberge, M. & Yonetani, T. (2008) Molecular dynamics simulations of hemoglobin A in different states and bound to DPG: effector-linked perturbation of tertiary conformations and HbA concerted dynamics, *Biophys J. 94*, 2737-51.

63. Ito, N., Komiyama, N. H. & Fermi, G. (1995) Structure of deoxyhaemoglobin of the antarctic fish Pagothenia bernacchii with an analysis of the structural basis of the root effect by comparison of the liganded and unliganded haemoglobin structures, *J Mol Biol. 250*, 648-58.

64. Baldwin, J. M. (1975) Structure and function of haemoglobin, *Prog Biophys Mol Biol. 29*, 225-320.

65. Verde, C., Vergara, A., Mazzarella, L. & di Prisco, G. (2008) The hemoglobins of fishes living at polar latitudes - current knowledge on structural adaptations in a changing environment, *Curr Protein Pept Sci. 9*, 578-90.

66. Edelstein, S. J. (1971) Extensions of the allosteric model for haemoglobin, *Nature. 230*, 224-7.

67. Vergara, A., Franzese, M., Merlino, A., Bonomi, G., Verde, C., Giordano, D., di Prisco, G., Lee, H. C., Peisach, J. & Mazzarella, L. (2009) Correlation between hemichrome stability and the root effect in tetrameric hemoglobins, *Biophys J. 97*, 866-74.

68. Berenbrink, M., Koldkjaer, P., Kepp, O. & Cossins, A. R. (2005) Evolution of oxygen secretion in fishes and the emergence of a complex physiological system, *Science. 307*, 1752-7.

69. Perutz, M. F. (1996) Cause of the root effect in fish haemoglobins, *Nat Struct Biol. 3*, 211-2.

70. D'Avino, R., Caruso, C., Tamburrini, M., Romano, M., Rutigliano, B., Polverino de Laureto, P., Camardella, L., Carratore, V. & di Prisco, G. (1994) Molecular characterization of the functionally distinct hemoglobins of the Antarctic fish *Trematomus newnesi*, *J. Biol. Chem. 269*, 9675-9681.

71. Camardella, L., Caruso, C., D'Avino, R., di Prisco, G., Rutigliano, B., Tamburrini, M., Fermi, G. & Perutz, M. F. (1992) Hemoglobin of the Antarctic fish *Pagothenia bernacchii*. Amino acid sequence, oxygen equilibria and crystal structure of its carbonmonoxy derivative, *J. Mol. Biol. 224*, 449-460.

72. Paoli, M., Liddington, R., Tame, J., Wilkinson, A. & Dodson, G. (1996) Crystal structure of T state haemoglobin with oxygen bound at all four haems, *J Mol Biol. 256*, 775-92.

73. Gervasio, F. L., Procacci, P., Cardini. G., Guarna, A., Giolitti, A. & Schettino, V. (2000) Interaction between aromatic residues. Molecular dynamics and ab initio exploration of the potential energy surfaceof the tryptophan-histidine pair, *J Phys Chem B. 104*, 1108–1114.

74. Vitagliano, L., Vergara, A., Bonomi, G., Merlino, A., Verde, C., di Prisco, G., Howes, B. D., Smulevich, G. & Mazzarella, L. (2008) Spectroscopic and crystallographic characterization of a tetrameric hemoglobin oxidation reveals structural features of the functional intermediate relaxed/tense state, *J Am Chem Soc. 130*, 10527-35.

75. Merlino, A., Vitagliano, L., Howes, B. D., Verde, C., di Prisco, G., Smulevich, G., Sica, F. & Vergara, A. (2009) Combined crystallographic and spectroscopic analysis of Trematomus bernacchii hemoglobin highlights analogies and differences in the peculiar oxidation pathway of Antarctic fish hemoglobins, *Biopolymers. 91*, 1117-25.

76. Edelstein, S. J. (1996) An Allosteric Theory for Hemoglobin Incorporating Asymmetric States to Test the Putative Molecular Code for Cooperativity, *J. Mol. Biol. 256*, 737-744.

77. Ibrahim, M., Xu, C. & Spiro, T. G. (2006) Differntial sensing of protein influences by NO and CO vibrations in heme adducts, *J Am Chem Soc. 128*, 16834-16845.

78. Antonini, E. & Brunori, M. (1971) Hemoglobin and Myoglobin in Their Reactions with Ligands, *(North Holland, Amsterdam)*

79. Sharma, V. S., Traylor, T. G., Gardiner, R. & Mizukami, H. (1987) Reaction of nitric oxide with heme proteins and model compounds of hemoglobin, *Biochemistry. 26*, 3837-43.

80. Cooper, C. E. (1999) Nitric oxide and iron proteins, *Biochimica et Biophysica Acta. 14111*, 290-309.

81. Springer, B. A., Sligar, S. G., Olson, J. S. & G.N.Jr., P. (1994) Mechanisms of Ligand Recognition in Myoglobin, *Chem. Rev. 94*, 699-714.

82. Sigfridsson, E. & Ryde, U. (2002) Theoretical study of the discrimination between O(2) and CO by myoglobin, *J Inorg Biochem. 91*, 101-15.

83. Jensen K.J. & U., R. (2004) How O_2 binds to heme *J. Biological Chemistry. 279*, 14561-14569.

84. Carver, T. E., Rohlfs, R. J., Olson, J. S., Gibson, Q. H., Blackmore, R. S., Springer, B. A. & Sligar, S. G. (1990) Analysis of the kinetic barriers for ligand binding to sperm whale myoglobin using site-directed mutagenesis and laser photolysis techniques, *J Biol Chem. 265*, 20007-20.

85. Lukin, J. A., Simplaceanu, V., Zou, M., Ho, N. T. & Ho, C. (2000) NMR reveals hydrogen bonds between oxygen and distal histidines in oxyhemoglobin, *Proc Natl Acad Sci U S A. 97*, 10354-8.

86. Moncada, S., Palmer, R. M. & Higgs, E. A. (1991) Nitric oxide: physiology, pathophysiology, and pharmacology, *Pharmacol Rev. 43*, 109-42.

87. Wang, Y. & Marsden, P. A. (1995) Nitric oxide synthases: gene structure and regulation, *Adv Pharmacol. 34*, 71-90.

88. Ignarro, L. J., Buga, G. M., Wood, K. S., Byrns, R. E. & Chaudhuri, G. (1987) Endothelium-derived relaxing factor produced and released from artery and vein is nitric oxide, *Proc Natl Acad Sci U S A. 84*, 9265-9.

89. Bonaventura, C., Fago, A., Henkens, R. & Crumbliss, A. L. (2004) Critical redox and allosteric aspects of nitric oxide interactions with hemoglobin, *Antioxid Redox Signal. 6*, 979-91.

90. Eich, R. F., Li, T., Lemon, D. D., Doherty, D. H., Curry, S. R., Aitken, J. F., Mathews, A. J., Johnson, K. A., Smith, R. D., Phillips, G. N., Jr. & Olson, J. S. (1996) Mechanism of NO-induced oxidation of myoglobin and hemoglobin, *Biochemistry. 35*, 6976-83.

91. Brooks, J. (1937) The action of nitrite on haemoglobin in the absence of oxygen, *Proc. R. Soc. Med. 123* 368–382.

92. Doyle, M. P., Pickering, R. A., DeWeert, T. M., Hoekstra, J. W. & Pater, D. (1981) Kinetics and mechanism of the oxidation of human deoxyhemoglobin by nitrites, *J Biol Chem. 256*, 12393-8.

93. Cosby, K., Partovi, K. S., Crawford, J. H., Patel, R. P., Reiter, C. D., Martyr, S., Yang, B. K., Waclawiw, M. A., Zalos, G., Xu, X., Huang, K. T., Shields, H., Kim-Shapiro, D. B., Schechter, A. N., Cannon, R. O., 3rd & Gladwin, M. T. (2003) Nitrite reduction to nitric oxide by deoxyhemoglobin vasodilates the human circulation, *Nat Med. 9*, 1498-505.

94. Nagababu, E., Ramasamy, S., Abernethy, D. R. & Rifkind, J. M. (2003) Active nitric oxide produced in the red cell under hypoxic conditions by deoxyhemoglobin-mediated nitrite reduction, *J Biol Chem. 278*, 46349-56.

95. Jensen, F. B. (2009) The dual roles of red blood cells in tissue oxygen delivery: oxygen carriers and regulators of local blood flow, *J Exp Biol. 212*, 3387-93.

96. McMahon, T. J., Exton Stone, A., Bonaventura, J., Singel, D. J. & Solomon Stamler, J. (2000) Functional coupling of oxygen binding and vasoactivity in S-nitrosohemoglobin, *J Biol Chem. 275*, 16738-45.

97. Jia, L., Bonaventura, C., Bonaventura, J. & Stamler, J. S. (1996) S-nitrosohaemoglobin: a dynamic activity of blood involved in vascular control, *Nature. 380*, 221-6.

98. Jensen, F. B. (2008) Nitric oxide formation from the reaction of nitrite with carp and rabbit hemoglobin at intermediate oxygen saturations, *Febs J. 275*, 3375-87.

99. Chan, N. L., Rogers, P. H. & Arnone, A. (1998) Crystal structure of the S-nitroso form of liganded human hemoglobin, *Biochemistry. 37*, 16459-64.

100. Chan, N. L., Kavanaugh, J. S., Rogers, P. H. & Arnone, A. (2004) Crystallographic analysis of the interaction of nitric oxide with quaternary-T human hemoglobin, *Biochemistry. 43*, 118-32.

101. Szabo, A. & Perutz, M. F. (1976) Equilibrium between six- and five-coordinated hemes in nitrosylhemoglobin: interpretation of electron spin resonance spectra, *Biochemistry. 15*, 4427-8.

102. Perutz, M. F., Kilmartin, J. V., Nagai, K., Szabo, A. & Simon, S. R. (1976) Influence of globin structures on the state of the heme. Ferrous low spin derivatives, *Biochemistry. 15*, 378-87.

103. Maxwell, J. C. & Caughey, W. S. (1976) An infrared study of NO bonding to heme B and hemoglobin A. Evidence for inositol hexaphosphate induced cleavage of proximal histidine to iron bonds, *Biochemistry. 15*, 388-96.

104. Scholler, D. M., Wang, M. Y. & Hoffman, B. M. (1979) Resonance Raman and EPR of nitrosyl human hemoglobin and chains, carp hemoglobin, and model compounds. Implications for the nitrosyl heme coordination state, *J Biol Chem. 254*, 4072-8.

105. Paoli, M., Dodson, G., Liddington, R. C. & Wilkinson, A. J. (1997) Tension in haemoglobin revealed by Fe-His(F8) bond rupture in the fully liganded T-state, *J Mol Biol. 271*, 161-7.

106. Shikama, K. (1998) The Molecular Mechanism of Autoxidation for Myoglobin and Hemoglobin: A Venerable Puzzle, *Chem Rev. 98*, 1357-1374.

107. Faivre, B., Menu, P., Labrude, P. & Vigneron, C. (1998) Hemoglobin autooxidation/oxidation mechanisms and methemoglobin prevention or reduction processes in the bloodstream. Literature review and outline of autooxidation reaction, *Artif Cells Blood Substit Immobil Biotechnol. 26*, 17-26.

108. Merlino, A., Howes, B. D., Prisco, G., Verde, C., Smulevich, G., Mazzarella, L. & Vergara, A. (2011) Occurrence and formation of endogenous histidine hexa-coordination in cold-adapted hemoglobins, *IUBMB Life. 63*, 295-303.

109. Quillin, M. L., Arduini, R. M., Olson, J. S. & Phillips, G. N., Jr. (1993) High-resolution crystal structures of distal histidine mutants of sperm whale myoglobin, *J Mol Biol. 234*, 140-55.

110. Ikeda-Saito, M., Hori, H., Andersson, L. A., Prince, R. C., Pickering, I. J., George, G. N., Sanders, C. R., 2nd, Lutz, R. S., McKelvey, E. J. & Mattera, R. (1992) Coordination structure of the ferric heme iron in engineered distal histidine myoglobin mutants, *J Biol Chem. 267*, 22843-52.

111. Ilari, A., Bonamore, A., Farina, A., Johnson, K. A. & Boffi, A. (2002) The X-ray structure of ferric Escherichia coli flavohemoglobin reveals an unexpected geometry of the distal heme pocket, *J Biol Chem. 277*, 23725-32.

112. Boffi, A., Takahashi, S., Spagnuolo, C., Rousseau, D. L. & Chiancone, E. (1994) Structural characterization of oxidized dimeric Scapharca inaequivalvis hemoglobin by resonance Raman spectroscopy, *J Biol Chem. 269*, 20437-40.

113. Giordano, D., Vergara, A., Lee, H. C., Peisach, J., Balestrieri, M., Mazzarella, L., Parisi, E., di Prisco, G. & Verde, C. (2007) Hemoglobin structure/function and globin-gene evolution in the Arctic fish Liparis tunicatus, *Gene. 406*, 58-68.

114. Marmo Moreira, L., Lima Poli, A., Costa-Filho, A. J. & Imasato, H. (2006) Pentacoordinate and hexacoordinate ferric hemes in acid medium: EPR, UV-Vis and CD studies of the giant extracellular hemoglobin of Glossoscolex paulistus, *Biophys Chem. 124*, 62-72.

115. Das, T. K., Couture, M., Lee, H. C., Peisach, J., Rousseau, D. L., Wittenberg, B. A., Wittenberg, J. B. & Guertin, M. (1999) Identification of the ligands to the ferric heme of Chlamydomonas chloroplast hemoglobin: evidence for ligation of tyrosine-63 (B10) to the heme, *Biochemistry. 38*, 15360-8.

116. Kakar, S., Hoffman, F. G., Storz, J. F., Fabian, M. & Hargrove, M. S. (2010) Structure and reactivity of hexacoordinate hemoglobins, *Biophys Chem. 152*, 1-14.

117. Milani, M., Pesce, A., Nardini, M., Ouellet, H., Ouellet, Y., Dewilde, S., Bocedi, A., Ascenzi, P., Guertin, M., Moens, L., Friedman, J. M., Wittenberg, J. B. & Bolognesi, M. (2005) Structural bases for heme binding and diatomic ligand recognition in truncated hemoglobins, *J Inorg Biochem. 99*, 97-109.

118. Howes, B. D., Giordano, D., Boechi, L., Russo, R., Mucciacciaro, S., Ciaccio, C., Sinibaldi, F., Fittipaldi, M., Marti, M. A., Estrin, D. A., di Prisco, G., Coletta, M., Verde, C. & Smulevich, G. (2011) The peculiar heme pocket of the 2/2 hemoglobin of cold-adapted Pseudoalteromonas haloplanktis TAC125, *J Biol Inorg Chem. 16*, 299-311.

119. Nagai, M., Aki, M., Li, R., Jin, Y., Sakai, H., Nagatomo, S. & Kitagawa, T. (2000) Heme structure of hemoglobin M Iwate [alpha 87(F8)His-->Tyr]: a UV and visible resonance Raman study, *Biochemistry. 39*, 13093-105.

120. Rachmilewitz, E. A., Peisach, J. & Blumberg, W. E. (1971) Studies on the stability of oxyhemoglobin A and its constituent chains and their derivatives, *J Biol Chem. 246*, 3356-66.

121. Rifkind, J. M., Abugo, O., Levy, A. & Heim, J. (1994) Detection, formation and relevance of hemichromes and hemochromes, *Methods. Enzymol. 231*, 449-480.

122. Levy, A. & Rifkind, J. M. (1985) Low-temperature formation of a distal histidine complex in hemoglobin: a probe for heme pocket flexibility, *Biochemistry. 24*, 6050-4.

123. Vergara, A., Vitagliano, L., Verde, C., di Prisco, G. & Mazzarella, L. (2008) Spectroscopic and crystallographic characterization of bis-histidyl adducts in tetrameric hemoglobins, *Methods Enzymol. 436*, 425-44.

124. Pesce, A., De Sanctis, D., Nardini, M., Dewilde, S., Moens, L., Hankeln, T., Burmester, T., Ascenzi, P. & Bolognesi, M. (2004) Reversible hexa- to penta-coordination of the heme Fe atom modulates ligand binding properties of neuroglobin and cytoglobin, *IUBMB Life. 56*, 657-64.

125. de Sanctis, D., Dewilde, S., Pesce, A., Moens, L., Ascenzi, P., Hankeln, T., Burmester, T. & Bolognesi, M. (2004) Crystal structure of cytoglobin: the fourth globin type discovered in man displays heme hexa-coordination, *J Mol Biol. 336*, 917-27.

126. Weiland, T. R., Kundu, S., Trent, J. T., 3rd, Hoy, J. A. & Hargrove, M. S. (2004) Bis-histidyl hexacoordination in hemoglobins facilitates heme reduction kinetics, *J Am Chem Soc. 126*, 11930-5.

127. Wittenberg, J. B., Wittenberg, B. A., Gibson, Q. H., Trinick, M. J. & Appleby, C. A. (1986) The kinetics of the reactions of Parasponia andersonii hemoglobin with oxygen, carbon monoxide, and nitric oxide, *J Biol Chem. 261*, 13624-31.

128. Croci, S., Pedrazzi, G., Passeri, G., Piccolo, P. & Ortalli, I. (2001) Acetylphenylhydrazine induced haemoglobin oxidation in erythrocytes studied by Mossbauer spectroscopy, *Biochim Biophys Acta. 1568*, 99-104.

129. Tokumasu, F., Nardone, G. A., Ostera, G. R., Fairhurst, R. M., Beaudry, S. D., Hayakawa, E. & Dvorak, J. A. (2009) Altered membrane structure and surface potential in homozygous hemoglobin C erythrocytes, *PLoS One. 4*, e5828.

130. Feng, L., Zhou, S., Gu, L., Gell, D. A., Mackay, J. P., Weiss, M. J., Gow, A. J. & Shi, Y. (2005) Structure of oxidized alpha-haemoglobin bound to AHSP reveals a protective mechanism for haem, *Nature. 435*, 697-701.

131. Gabbianelli, R., Zolese, G., Bertoli, E. & Falcioni, G. (2004) Correlation between functional and structural changes of reduced and oxidized trout hemoglobins I and IV at different pHs. A circular dichroism study, *Eur J Biochem. 271*, 1971-9.

132. Robinson, V. L., Smith, B. B. & Arnone, A. (2003) A pH-dependent aquomet-to-hemichrome transition in crystalline horse methemoglobin, *Biochemistry. 42*, 10113-25.

133. Hargrove, M. S., Brucker, E. A., Stec, B., Sarath, G., Arredondo-Peter, R., Klucas, R. V., Olson, J. S. & Phillips, G. N., Jr. (2000) Crystal structure of a nonsymbiotic plant hemoglobin, *Structure. 8*, 1005-14.

134. Pesce, A., Dewilde, S., Nardini, M., Moens, L., Ascenzi, P., Hankeln, T., Burmester, T. & Bolognesi, M. (2004) The human brain hexacoordinated neuroglobin three-dimensional structure, *Micron. 35*, 63-5.

135. Hoy, J. A., Kundu, S., Trent, J. T., 3rd, Ramaswamy, S. & Hargrove, M. S. (2004) The crystal structure of Synechocystis hemoglobin with a covalent heme linkage, *J Biol Chem. 279*, 16535-42.

136. Mitchell, D. T., Kitto, G. B. & Hackert, M. L. (1995) Structural analysis of monomeric hemichrome and dimeric cyanomet hemoglobins from Caudina arenicola, *J Mol Biol. 251*, 421-31.

137. Vallone, B., Nienhaus, K., Brunori, M. & Nienhaus, G. U. (2004) The structure of murine neuroglobin: Novel pathways for ligand migration and binding, *Proteins. 56*, 85-92.

138. de Sanctis, D., Dewilde, S., Vonrhein, C., Pesce, A., Moens, L., Ascenzi, P., Hankeln, T., Burmester, T., Ponassi, M., Nardini, M. & Bolognesi, M. (2005) Bishistidyl heme hexacoordination, a key structural property in Drosophila melanogaster hemoglobin, *J Biol Chem. 280*, 27222-9.

139. Borgstahl, G. E., Rogers, P. H. & Arnone, A. (1994) The 1.8 A structure of carbonmonoxy-beta 4 hemoglobin. Analysis of a homotetramer with the R quaternary structure of liganded alpha 2 beta 2 hemoglobin, *J Mol Biol. 236*, 817-30.

140. Borgstahl, G. E., Rogers, P. H. & Arnone, A. (1994) The 1.9 A structure of deoxy beta 4 hemoglobin. Analysis of the partitioning of quaternary-associated and ligand-induced changes in tertiary structure, *J Mol Biol. 236*, 831-43.

141. Geraci, G., Parkhurst, L. J. & Gibson, Q. H. (1969) Preparation and properties of alpha- and beta-chains from human hemoglobin, *J Biol Chem. 244*, 4664-7.

142. Tsuruga, M., Matsuoka, A., Hachimori, A., Sugawara, Y. & Shikama, K. (1998) The molecular mechanism of autoxidation for human oxyhemoglobin. Tilting of the distal histidine causes nonequivalent oxidation in the beta chain, *J Biol Chem. 273*, 8607-15.

143. Perutz, M. F. (1968) Preparation of haemoglobin crystals. , *J Cryst Growth. 2*, 54–56.

144. Coppola, D., Giordano, D., Vergara, A., Mazzarella, L., di Prisco, G., Verde, C. & Russo, R. (2010) The hemoglobins of sub-Antarctic fishes of the suborder Notothenioidei, *Polar Sci. 4,*, 295-308.

145. Otwinowsky, Z. & Minor, W. (1997) Processing of X-ray diffraction data collected in oscillation mode, *Methods Enzymol.* , 307-326.

146. Sheldrick, G. M. & Schneider, T. R. (1997) SHELXL: high-resolution refinement, *Methods Enzymol. 277*, 319-43.

147. Jones, T. A., Zou, J. Y., Cowan, S. W. & Kjeldgaard, M. (1991) Improved methods for building protein models in electron density maps and the location of errors in these models, *Acta Crystallogr A. 47 (Pt 2)*, 110-9.

148. Laskowski, R. A., MacArthur, M. W., Moss, M. D. & Thorton, J. M. (1993) PROCHECK: A program to check the stereochemical quality of protein structure, *J Appl Crystallogr. 26* 283-291.

149. Hooft, R. W., Vriend, G., Sander, C. & Abola, E. E. (1996) Errors in protein structures, *Nature. 381*, 272.

150. Matthews, B. W. (1968) Solvent content of protein crystals, *J. Mol. Biology. 33*, 491-497.

151. Gouterman, M. (1979) The Porphyrins., *D. Dolphin Ed. Academic Press.*

152. Eaton, W. A. & Hofrichter, J. (1981) Polarized absorption and linear dichroism spectroscopy of hemoglobin, *Methods Enzymol. 76*, 175-261.

153. Dvorak, J. A. & Stotler, W. F. (1971) A controlled-environment culture system for high resolution light microscopy, *Exp Cell Res. 68*, 144-8.

154. Rivetti, C., Mozzarelli, A., Rossi, G. L., Henry, E. R. & Eaton, W. A. (1993) Oxygen binding by single crystals of hemoglobin, *Biochemistry. 32*, 2888-906.

155. Asher, S. A. (1988) UV resonace Raman studies of molecular structures and dynamics, *Ann. Rev. Phys. Chem. 39*, 537–588.

156. Asher, S. (1981) Resonance Raman spectroscopy of hemoglobin, *Methods Enzymol. 76*, 371-413.

157. Torres Filho, I. P., Terner, J., Pittman, R. N., Somera, L. G., 3rd & Ward, K. R. (2005) Hemoglobin oxygen saturation measurements using resonance Raman intravital microscopy, *Am J Physiol Heart Circ Physiol. 289*, H488-95.

158. Greenfield, N. J. (2007) Using circular dichroism spectra to estimate protein secondary structure, *Nat. Protocols. 1*, 2876-2890.

159. Greenfield, N. J. (2007) Using circular dichroism collected as a function of temperature to determine the thermodynamics of protein unfolding and binding interactions. , *Nat. Protocols. . 1* 2527-2535.

160. Greenfield, N. J. (2007) Determination of the folding of proteins as a function of denaturants, osmolytes or ligands using circular dichroism. , *Nat. Protocols. 1*, 2733-2741

161. Greenfield, N. J. (2007) Analysis of the kinetics of folding of proteins and peptides using circular dichroism. , *Nat. Protocols 1*, 2891-2899.

162. Sørensen, H. P. & Kim, K. M. (2005) Advanced genetic strategies for recombinant protein expression in Escherichia coli, *J. Biotech. 115*, 113-128.

163. Vitagliano, L., Bonomi, G., Riccio, A., di Prisco, G., Smulevich, G. & Mazzarella, L. (2004) The oxidation process of Antarctic fish hemoglobins, *Eur. J. Biochem. 271*, 1651-1659.

164. Sippl, M. J. (1993) Recognition of errors in three-dimensional structures of proteins, *Proteins. 17*, 355-62.

165. Sippl, M. J. (1995) Knowledge-based potentials for proteins, *Curr Opin Struct Biol. 5*, 229-35.

166. Van Der Spoel, D., Lindahl, E., Hess, B., Groenhof, G., Mark, A. E. & Berendsen, H. J. (2005) GROMACS: fast, flexible, and free, *J Comput Chem. 26*, 1701-18.

167. Lee, C. Y., W.; & Parr, R. G. (1988) Development of the Colle-Salvetti correlation-energy formula into a functional of the electron density, *Phys. Rev. B*, 785-789.

168. Hay, P. J. & Wadt, W. R. (1985) Abinitio Effective Core Potentials for Molecular Calculations - Potentials for the Transition-Metal Atoms Sc to Hg, *Journal of Chemical Physics. 82*, 270-283.

169. M. J. Frisch, G. W. T., H. B. Schlegel, G. E. Scuseria, M. A. Robb, J. R. Cheeseman, V. G. Zakrzewski, J. A. Montgomery, Jr., R. E. S., J. C. Burant, S. Dapprich, J. M. Millam, A. D. Daniels, K. N. Kudin, M. C. Strain, O. Farkas, J. Tomasi, V. Barone, M. Cossi, R. Cammi, B. Mennucci, C. Pomelli, C. Adamo, S. Clifford, J. Ochterski, G. A. Petersson, P. Y. Ayala, Q. Cui, K. M., P. Salvador, J. J. Dannenberg, D. K. Malick, A. D. Rabuck, K. Raghavachari, J. B. Foresman, J. Cioslowski, J. V. Ortiz, A. G. Baboul, B. B. Stefanov, G. Liu, A. Liashenko, P. Piskorz, I. Komaromi, R. Gomperts, R. L. Martin, D. J. Fox, T. Keith, M. A. Al-Laham, C. Y. Peng, A. Nanayakkara, M. Challacombe, P. M. W. Gill, B. Johnson, W. Chen, M. W. Wong, J. L. Andres, C. Gonzalez, M. Head-Gordon, E. S. Replogle & Pople., J. A. (2001) Gaussian 98 (Revision A.11), *Gaussian, Inc., Pittsburgh PA.*

170. Schmidt, M. W., Baldridge, K. K., Boatz, J. A., Elbert, S. T., Gordon, M. S., Jensen, J. H., Koseki, S., Matsunaga, N., Nguyen, K. A., Su, S. J., Windus, T. L., Dupuis, M. & Montgomery, J. A. (1993) General Atomic and Molecular Electronic-Structure System, *Journal of Computational Chemistry. 14*, 1347-1363.

171. Smith, D. M. A., Dupuis, M., Vorpagel, E. R. & Straatsma, T. P. (2003) Characterization of electronic structure and properties of a bis(histidine) heme model complex, *Journal of the American Chemical Society. 125*, 2711-2717.

172. Merlino, A., Vitagliano, L., Ceruso, M. A., Di Nola, A. & Mazzarella, L. (2002) Global and local motions in ribonuclease A: a molecular dynamics study, *Biopolymers. 65*, 274-83.

173. Merlino, A., Vitagliano, L., Ceruso, M. A. & Mazzarella, L. (2004) Dynamic properties of the N-terminal swapped dimer of ribonuclease A, *Biophys J. 86*, 2383-91.

174. Merlino, A., Ceruso, M. A., Vitagliano, L. & Mazzarella, L. (2005) Open interface and large quaternary structure movements in 3D domain swapped proteins: insights from molecular dynamics simulations of the C-terminal swapped dimer of ribonuclease A, *Biophys J. 88*, 2003-12.

175. Berendsen, H. J. C., Postma, J. P. M., van Gusteren, W. F. & Hermans, J. (1981) Interaction models for water in relation to protein hydration., *Dordrecht: Reidel*, 331–342.

176. Kerwin, B. A., Looker, D. G., Hess, E., Revilla-Sharp, P. & Akers, M. J. (1997) Development of a storage stable liquid formulation for a recombinant hemoglobin, *Book of Abstracts, 213th ACS National Meeting, San Francisco, April 13-17*, I&EC-077.

177. Darden, T., York, D. & Pedersen, L. (1993) Part Mesh Ewald: an log (N) method for Ewald sums in large systems., *J Chem Phys*, 10089-10092.

178. Berendsen, H. J. C., Postma, J. P. M., van Gusteren, W. F., Di Nola, A. & Haak, J. R. (1984) Molecular dynamics with coupling to an external bath, *J Chem Phys. 81*, 3684-3691.

179. Ascenzi, P., Bocedi, A., de Sanctis, D., Pesce, A., Bolognesi, M., Marden, M. C., Dewilde, S., Moens, L., Hankeln, T. & Burmester, T. (2004) Neuroglobin and cytoglobin: Two new entries in the hemoglobin superfamily*, *Biochem Mol Biol Educ. 32*, 305-13.

180. Bucci, E. & Fronticelli, C. (1965) A New Method for the Preparation of Alpha and Beta Subunits of Human Hemoglobin, *J Biol Chem. 240*, PC551-2.

181. Navaza, J. & Saludjian, P. (1997) AMoRe: an automated molecular replacement program package, *Methods Enzymol. 276*, 581-594.

182. Richardson, J. (1981) The Amatomy and Taxonomy of protein structure., *Advances in Protein Chemistry. 34*, Academic Press.

183. Yamaguchi, T., Pang, J., Reddy, K. S., Witkowska, H. E., Surrey, S. & Adachi, K. (1996) Expression of soluble human beta-globin chains in bacteria and assembly in vitro with alpha-globin chains, *J Biol Chem. 271*, 26677-83.

184. Yamaguchi, T., Pang, J., Reddy, K. S., Surrey, S. & Adachi, K. (1998) Role of beta112 Cys (G14) in homo- (beta4) and hetero- (alpha2 beta2) tetramer hemoglobin formation, *J Biol Chem. 273*, 14179-85.

185. Adachi, K., Yamaguchi, T., Pang, J. & Surrey, S. (1998) Effects of increased anionic charge in the beta-globin chain on assembly of hemoglobin in vitro, *Blood. 91*, 1438-45.

186. Schneider, T. R. (2000) Objective comparison of protein structures: error-scaled difference distance matrices, *Acta Crystallogr D Biol Crystallogr. 56*, 714-21.

187. Hernan, R. A., Hui, H. L., Andracki, M. E., Noble, R. W., Sligar, S. G., Walder, J. A. & Walder, R. Y. (1992) Human hemoglobin expression in Escherichia coli: importance of optimal codon usage, *Biochemistry. 31*, 8619-28.

188. Ventura, S. & Villaverde, A. (2006) Protein quality in bacterial inclusion bodies, *Trends Biotechnol. 24*, 179-85.

189. Doglia, S. M., Ami, D., Natalello, A., Gatti-Lafranconi, P. & Lotti, M. (2008) Fourier transform infrared spectroscopy analysis of the conformational quality of recombinant proteins within inclusion bodies, *Biotechnol J. 3*, 193-201.

190. Gonzalez-Montalban, N., Garcia-Fruitos, E. & Villaverde, A. (2007) Recombinant protein solubility - does more mean better?, *Nat Biotechnol. 25*, 718-20.

191. Martinez-Alonso, M., Gonzalez-Montalban, N., Garcia-Fruitos, E. & Villaverde, A. (2009) Learning about protein solubility from bacterial inclusion bodies, *Microb Cell Fact. 8*, 4.

192. Jevsevar, S., Gaberc-Porekar, V., Fonda, I., Podobnik, B., Grdadolnik, J. & Menart, V. (2005) Production of nonclassical inclusion bodies from which correctly folded protein can be extracted, *Biotechnol Prog. 21*, 632-9.

193. Brooks, C. L., 3rd. (1992) Characterization of "native" apomyoglobin by molecular dynamics simulation, *J Mol Biol. 227*, 375-80.

194. Merlino, A., Esposito, L. & Vitagliano, L. (2006) Polyglutamine repeats and beta-helix structure: molecular dynamics study, *Proteins. 63*, 918-27.

195. Sham, Y. Y., Ma, B., Tsai, C. J. & Nussinov, R. (2001) Molecular dynamics simulation of Escherichia coli dihydrofolate reductase and its protein fragments: relative stabilities in experiment and simulations, *Protein Sci. 10*, 135-48.

196. Guallar, V., Jarzecki, A. A., Friesner, R. A. & Spiro, T. G. (2006) Modeling of ligation-induced helix/loop displacements in myoglobin: toward an understanding of hemoglobin allostery, *J Am Chem Soc. 128*, 5427-35.

197. Boechi, L., Marti, M. A., Milani, M., Bolognesi, M., Luque, F. J. & Estrin, D. A. (2008) Structural determinants of ligand migration in Mycobacterium tuberculosis truncated hemoglobin O, *Proteins. 73*, 372-9.

198. Capece, L., Estrin, D. A. & Marti, M. A. (2008) Dynamical characterization of the heme NO oxygen binding (HNOX) domain. Insight into soluble guanylate cyclase allosteric transition, *Biochemistry. 47*, 9416-27.

199. Boechi, L., Marti, M. A., Vergara, A., Sica, F., Mazzarella, L., Estrin, D. A. & Merlino, A. (2011) Protonation of histidine 55 affects the oxygen access to heme in the alpha chain of the hemoglobin from the Antarctic fish Trematomus bernacchii, *IUBMB Life. 63*, 175-82.

200. Capece, L., Marti, M. A., Bidon-Chanal, A., Nadra, A., Luque, F. J. & Estrin, D. A. (2009) High pressure reveals structural determinants for globin hexacoordination: neuroglobin and myoglobin cases, *Proteins. 75*, 885-94.

201. Feng, L., Zhou, S., Gu, L., Gell, D., Mackay, J., Weiss, M., Gow, A. & Shi, Y. (2005) Structure of oxidized α-haemoglobin bound to AHSP reveals a protective mechanism for haem, *Nature. 435*, 697-701.

202. Fedeli, D., Tiano, L., Gabbianelli, R., Caulini, G. C., Wozniak, M. & Falcioni, G. (2001) Hemoglobin components from trout (Salmo irideus): determination of their peroxidative activity, *Comp Biochem Physiol B Biochem Mol Biol. 130*, 559-64.

203. Verde, C., Howes, B. D., De Rosa, M. C., Raiola, L., Smulevich, G., Williams, R., Giardina, B., Parisi, E. & Di Prisco, G. (2004) Structure and function of the Gondwanian hemoglobin of Pseudaphritis urvillii, a primitive notothenioid fish of temperate latitudes, *Protein Sci. 13*, 2766-81.

204. Giordano, D., Boechi, L., Vergara, A., Marti, M. A., Samuni, U., Dantsker, D., Grassi, L., Estrin, D. A., Friedman, J. M., Mazzarella, L., di Prisco, G. & Verde, C. (2009) The hemoglobins of the sub-Antarctic fish Cottoperca gobio, a phyletically basal species--oxygen-binding equilibria, kinetics and molecular dynamics, *FEBS J. 276*, 2266-77.

205. Merlino, A., Russo Krauss, I., Castellano, I., De Vendittis, E., Rossi, B., Conte, M., Vergara, A. & Sica, F. (2010) Structure and flexibility in cold-adapted iron superoxide dismutases: the case of the enzyme isolated from Pseudoalteromonas haloplanktis, *J Struct Biol. 172*, 343-52.

206. Johnston, I. A. (2003) Muscle metabolism and growth in Antarctic fishes (suborder Notothenioidei): evolution in a cold environment, *Comp Biochem Physiol B Biochem Mol Biol. 136*, 701-13.

207. Mazzarella, L., D'Avino, R., di Prisco, G., Savino, C., Vitagliano, L., Moody, P. C. & Zagari, A. (1999) Crystal structure of Trematomus newnesi haemoglobin re-opens the root effect question, *J Mol Biol. 287*, 897-906.

208. Brickle, P., Arkhipkin, A. I. & Shcherbich, Z. N. (2005) Age and growth in a temperate euryhaline notothenioid, Eleginops maclovinus from the Falkland Islands, *J. Mar. Biol. Assoc. U. K. 85*

209. Torres Filho, I. P., Terner, J., Pittman, R. N., Somera, L. G. & Ward, K. R. (2004) Hemoglobin oxygen saturation measurements using resonance Raman intravital microscopy, *Am. J. Physiol. Heart Circ. Physiol. 289*, 488-495.

210. Choi, S., Spiro, T. G., Langry, K. G., Smith, K. M., Budd, D. L. & La Mar, G. N. (1982) Structural correlations and vinyl influences in the Resonance Raman spectra of protoheme complexes and proteins. , *J. Am. Chem. Soc. 104* 4345-4351.

211. Spiro, T. G. & Strekas, T. C. (1974) Resonance Raman spectra of heme proteins. Effects of oxidation and spin state, *J Am Chem Soc. 96*, 338-45.

212. Choi, S., Spiro, T. G., Langry, K. C. & Smith, K. M. (1982) Vinyl influences on protoheme resonance Raman spectra: nickel(II) protoporphyrin IX with deuterated vinyl groups, *Journal of the American Chemical Society. 104* 4337-4344.

213. Kitagawa, T., Abe, M. & Ogoshi, H. (1978) Resonance Raman spectra of octaethylporphyrinato-Ni(II) and meso-deuterated and [sup 15]N substituted derivatives.I. Observation and assignments of nonfundamental Raman lines, *The Journal of Chemical Physics. 69*, 4516-4525.

214. Abe, M., Kitagawa, T. & Kyogoku, Y. (1978) Resonance Raman spectra of octaethylporphyrinato-Ni(II) and meso-deuterated and [sup 15]N substituted derivatives.II. A normal coordinate analysis,, *The Journal of Chemical Physics 69*, 4526-4534.

215. Merlino, A., Vitagliano, L., Balsamo, A., Nicoletti, F. P., Howes, B. D., Giordano, D., Coppola, D., di Prisco, G., Verde, C., Smulevich, G., Mazzarella, L. & Vergara, A. (2010) Crystallization, preliminary X-ray diffraction studies and Raman microscopy of the major haemoglobin from the sub-Antarctic fish Eleginops maclovinus in the carbomonoxy form, *Acta Crystallogr Sect F Struct Biol Cryst Commun. 66*, 1536-40.

216. Merlino, A., Verde, C., di Prisco, G., Mazzarella, L. & Vergara, A. (2008) Reduction of ferric hemoglobin from Trematomus bernacchii in a partial bis-histidyl state produces a deoxy coordination even when encapsulated into the crystal phase *Spectroscopy 22*, 143-152.

217. Merlino, A., Sica, F., Mazzarella, L., Zagari, A. & Vergara, A. (2008) Correlation between Raman and X-ray crystallography data of (Pro-Pro-Gly)10, *Biophys Chem. 137*, 24-7.

218. Henry, E. R., Bettati, S., Hofrichter, J. & Eaton, W. A. (2002) A tertiary two-state allosteric model for hemoglobin, *Biophys Chem. 98*, 149-64.

219. Viappiani, C., Bettati, S., Bruno, S., Ronda, L., Abbruzzetti, S., Mozzarelli, A. & Eaton, W. A. (2004) New insights into allosteric mechanisms from trapping unstable protein conformations in silica gels, *Proc Natl Acad Sci U S A. 101*, 14414-9.

220. Liddington, R. (1994) X-ray crystallography of partially liganded structures, *Methods Enzymol. 232*, 15-26.

221. Mozzarelli, A., Rivetti, C., Rossi, G. L., Eaton, W. A. & Henry, E. R. (1997) Allosteric effectors do not alter the oxygen affinity of hemoglobin crystals, *Protein Sci. 6*, 484-9.

222. Srinivasan, R. & Rose, G. D. (1994) The T-to-R transformation in hemoglobin: a reevaluation, *Proc Natl Acad Sci U S A. 91*, 11113-7.

223. Wilson, J., Phillips, K. & Luisi, B. (1996) The crystal structure of horse deoxyhaemoglobin trapped in the high-affinity (R) state, *J Mol Biol. 264*, 743-56.

224. Carey, P. R., Chen, Y., Gong, B. & Kalp, M. (2010) Kinetic crystallography by Raman microscopy, *Biochim Biophys Acta. 1814*, 742-9.

225. Carpentier, P., Royant, A., Ohana, J. & Bourgeois, D. (2007) Advances in spectroscopic methods for biological crystals. 2. Raman spectroscopy, *Journal of Applied Crystallography. 40,*, 1113-1122.

226. Gladwin, M. T., Ognibene, F. P., Pannell, L. K., Nichols, J. S., Pease-Fye, M. E., Shelhamer, J. H. & Schechter, A. N. (2000) Relative role of heme nitrosylation and beta-cysteine 93 nitrosation in the transport and metabolism of nitric oxide by hemoglobin in the human circulation, *Proc Natl Acad Sci U S A. 97*, 9943-8.

227. Gladwin, M. T., Wang, X., Reiter, C. D., Yang, B. K., Vivas, E. X., Bonaventura, C. & Schechter, A. N. (2002) S-Nitrosohemoglobin is unstable in the reductive erythrocyte environment and lacks O2/NO-linked allosteric function, *J Biol Chem. 277*, 27818-28.

228. Herold, S. & Boccini, F. (2006) NO* release from MbFe(II)NO and HbFe(II)NO after oxidation by peroxynitrite, *Inorg Chem. 45*, 6933-43.

229. Choi, S. & Spiro, T. G. (1983) Out-of-plane deformation modes in the resonance Raman spectra of metalloporphyrins and heme proteins *Journal of the American Chemical Society 105* 3683-3692.

230. Stong, J. D., Burke, J. M., Daly, P., Wright, P. & Spiro, T. G. (1980) Resonance Raman spectra of nitrosyl heme proteins and of porphyrin analogues., *J. Am. Chem. Soc. 102*, 5815–5819.

231. Szabo, A. & Barron, L. D. (1975) Letter: Resonance Raman studies of nitric oxide hemoglobin, *J Am Chem Soc. 97*, 660-2.

232. Scheidt, W. R. & Piciulo, P. L. (1976) Nitrosylmetalloporphyrins. III. Synthesis and molecular stereochemistry of nitrosyl-alpha, beta, gamma, delta-tetraphenylporphinato(1-methylimidazole)iron(II), *J Am Chem Soc. 98*, 1913-9.

233. Arcovito, A. & Della Longa, S. (2011) Ligand binding intermediates of nitrosylated human hemoglobin induced at low temperature by X-ray irradiation, *Inorg Chem. 50*, 9423-9.

234. Garman, E. F. (2010) Radiation damage in macromolecular crystallography: what is it and why should we care?, *Acta Crystallogr D Biol Crystallogr. 66*, 339-51.

235. McGeehan, J. E., Carpentier, P., Royant, A., Bourgeois, D. & Ravelli, R. B. (2007) X-ray radiation-induced damage in DNA monitored by online Raman, *J Synchrotron Radiat. 14*, 99-108.

236. Carpentier, P., Royant, A., Weik, M. & Bourgeois, D. (2010) Raman-assisted crystallography suggests a mechanism of X-ray-induced disulfide radical formation and reparation, *Structure. 18*, 1410-9.

237. Paithankar, K. S., Owen, R. L. & Garman, E. F. (2009) Absorbed dose calculations for macromolecular crystals: improvements to RADDOSE, *J Synchrotron Radiat. 16*, 152-62.

238. Forouhar, F., Anderson, J. L., Mowat, C. G., Vorobiev, S. M., Hussain, A., Abashidze, M., Bruckmann, C., Thackray, S. J., Seetharaman, J., Tucker, T., Xiao, R., Ma, L. C., Zhao, L., Acton, T. B., Montelione, G. T., Chapman, S. K. & Tong, L. (2007) Molecular insights into substrate recognition and catalysis by tryptophan 2,3-dioxygenase, *Proc Natl Acad Sci U S A. 104*, 473-8.

239. van Manen, H. J., M. Kraan Y., Roos D. & Otto, C. (2005) Single-cell Raman and fluorescence microscopy reveal the association of lipid bodies with phagosomes in leukocytes, *Proc Natl Acad Sci USA. 102* 10159–10164.

240. De Luca, A. C., Rusciano, G., Ciancia, R., Martinelli, V., Pesce, G., Rotoli, B., Selvaggi, L. & Sasso, A. (2008) Spectroscopical and mechanical characterization of normal and thalassemic red blood cells by Raman Tweezers., *Opt. Express. 16*, 7943–7957.

241. Rusciano, G., De Luca, A. C., Pesce, G. & Sasso, A. (2008) Raman Tweezers as diagnostic tool of hemoglobin-related blood disorders, *Sensors. 8*, 7818-7832.

242. Chan, J., Fore, S., Wachsmann-Hogiu, S. & Huser, T. (2008) Raman spectroscopy and microscopy of individual cells and cellular components. , *Laser Photonics Review. 2*, 325-349.

243. Tu, A. T. (1982) Raman Spectroscopy in Biology: Principles and Application, *Wiley, New York.*

244. Carey, P. R. (1982) Biochemical applications of Raman and resonance Raman spectroscopies., *New York: Academic Press.*

245. Parker, F. S. (1983) Application of infrared, Raman and resonance Raman spectroscopy in biochemistry, *New York: Plenum Press.*

246. Spiro, T. G. (1987) Biological applications of Raman spectroscopy, *New York: Wiley & Sons.*

247. Minsky, M. (1988) Memoir on inventing the confocal microscope, *Scanning. 10*, 128-138.

248. Barry, B. & Mathies, R. (1982) Resonance Raman microscopy of rod and cone photoreceptors, *J Cell Biol. 94*, 479-82.

249. Dalterio, R. A., Nelson, W. H., Britt, D., Sperry, J. F., Tanguay, J. F. & Suib, S. L. (1987) The steady-state and decay characteristics of primary fluorescence from live bacteria, *Appl. Spectrosc. 41*, 234-241.

250. Uzunbajakava, N. & Otto, C. (2003) Combined Raman and continuous-wave-excited two-photon fluorescence cell imaging, *Opt Lett. 28*, 2073-5.

251. Uzunbajakava, N., Lenferink, A., Kraan, Y., Volokhina, E., Vrensen, G., Greve, J. & Otto, C. (2003) Nonresonant confocal Raman imaging of DNA and protein distribution in apoptotic cells, *Biophys J. 84*, 3968-81.

252. Draux, F., Gobinet, C., Sule-Suso, J., Manfait, M., Jeannesson, P. & Sockalingum, G. D. Raman imaging of single living cells: probing effects of non-cytotoxic doses of an anti-cancer drug, *Analyst. 136*, 2718-25.

253. Draux, F., Gobinet, C., Sule-Suso, J., Trussardi, A., Manfait, M., Jeannesson, P. & Sockalingum, G. D. Raman spectral imaging of single cancer cells: probing the impact of sample fixation methods, *Anal Bioanal Chem. 397*, 2727-37.

254. Puppels, G. J., Garritsen, H. S., Kummer, J. A. & Greve, J. (1993) Carotenoids located in human lymphocyte subpopulations and natural killer cells by Raman microspectroscopy, *Cytometry. 14*, 251-6.

255. van Manen, H. J., Uzunbajakava, N., van Bruggen, R., Roos, D. & Otto, C. (2003) Resonance Raman imaging of the NADPH oxidase subunit cytochrome b558 in single neutrophilic granulocytes, *J Am Chem Soc. 125*, 12112-3.

256. Wood, B. R., Tait, B. & McNaughton, D. (2001) Micro-Raman characterization of the R to T state transition of haemoglobin within a single living erythrocyte, *Biochim. Biophys. Acta. 1539*.

257. Maquelin, K., Choo-Smith, L. P., Endtz, H. P., Bruining, H. A. & Puppels, G. J. (2002) Rapid identification of Candida species by confocal Raman microspectroscopy, *J Clin Microbiol. 40*, 594-600.

258. Maquelin, K., Dijkshoorn, L., van der Reijden, T. J. & Puppels, G. J. (2006) Rapid epidemiological analysis of Acinetobacter strains by Raman spectroscopy, *J Microbiol Methods. 64*, 126-31.

259. Maquelin, K., Kirschner, C., Choo-Smith, L. P., van den Braak, N., Endtz, H. P., Naumann, D. & Puppels, G. J. (2002) Identification of medically relevant microorganisms by vibrational spectroscopy, *J Microbiol Methods. 51*, 255-71.

260. Taleb, A., Diamond, J., McGarvey, J. J., Beattie, J. R., Toland, C. & Hamilton, P. W. (2006) Raman microscopy for the chemometric analysis of tumor cells, *J Phys Chem B. 110*, 19625-31.

261. Chen, K., Qin, Y., Zheng, F., Sun, M. & Shi, D. (2006) Diagnosis of colorectal cancer using Raman spectroscopy of laser-trapped single living epithelial cells, *Opt Lett. 31*, 2015-7.

262. Buschman, H. P., Motz, J. T., Deinum, G., Romer, T. J., Fitzmaurice, M., Kramer, J. R., van der Laarse, A., Bruschke, A. V. & Feld, M. S. (2001) Diagnosis of human coronary atherosclerosis by morphology-based Raman spectroscopy, *Cardiovasc Pathol. 10*, 59-68.

263. Silveira, L., Jr., Sathaiah, S., Zangaro, R. A., Pacheco, M. T., Chavantes, M. C. & Pasqualucci, C. A. (2003) Near-infrared Raman spectroscopy of human coronary arteries: histopathological classification based on Mahalanobis distance, *J Clin Laser Med Surg. 21*, 203-8.

264. Uzunbajakava, N., Lenferink, A., Kraan, Y., Willekens, B., Vrensen, G., Greve, J. & Otto, C. (2001) Nonresonant Raman imaging of protein distribution in single human cells, *Biopolymers. 72*, 1-9.

265. Ramser, K., Logg, K., Goksor, M., Enger, J., Kall, M. & Hanstorp, D. (2004) Resonance Raman spectroscopy of optically trapped functional erythrocytes, *J Biomed Opt. 9*, 593-600.

266. Wood, B. R., Caspers, P., Puppels, G. J., Pandiancherri, S. & McNaughton, D. (2007) Resonance Raman spectroscopy of red blood cells using near-infrared laser excitation, *Anal Bioanal Chem. 387*, 1691-703.

267. Brunner, H., Mayer, A. & Sussner, H. (1972) Resonance raman scattering on the haem group of oxy- and deoxyhaemoglobin, *J Mol Biol. 70*, 153-6.

268. Ramser, K., Enger, J., Goksor, M., Hanstorp, D., Logg, K. & Kall, M. (2005) A microfluidic system enabling Raman measurements of the oxygenation cycle in single optically trapped red blood cells, *Lab Chip. 5*, 431-6.

269. Kohne, E. (2011) Hemoglobinopathies. Clinical Manifestations, Diagnosis, and Treatment, *Deutsches Ärzteblatt International | Dtsch Arztebl Int. 108*, 532-40.

270. Padlan, E. A. & Love, W. E. (1985) Refined crystal structure of deoxyhemoglobin S. I. Restrained least-squares refinement at 3.0-A resolution, *J Biol Chem. 260*, 8272-9.

271. Hirsch, R. E., Raventos-Suarez, C., Olson, J. A. & Nagel, R. L. (1985) Ligand state of intraerythrocytic circulating HbC crystals in homozygote CC patients, *Blood. 66*, 775-7.

272. Nagel, R. L. & Steinberg, M. H. (2001) Hemoglobin SC Disease and HbC Disorders. In Disorders of Hemoglobin: Genetics, Pathophysiology, and Clinical Management, *M. H. Steinberg,*

B. G. Forget, D. R. Higgs, and R. L. Nagel, editors. Cambridge University Press, Cambridge, UK. , 711–785.

273. Wood, B. R. & McNaughton, D. (2002) Raman excitation wavelength investigation of single red blood cell in vivo, *J. Raman Spectrosc. 33*, 517-523.

274. Sijtsema, N. M., Wouters, S. D., de Grauw, C. J., Otto, C. & Greve, J. (1998) Confocal direct imaging Raman microscope: design and applications in biology, *Appl. Spectrosc. 52* 348–355.

275. Golub, G. & Van Loan, C. (1983) Matrix Computations., *The Johns Hopkins University Press, Baltimore.*

276. Ashkin, A., Dziedzic, J. M., Bjorkholm, J. E. & Chu, S. (1986) Observation of a single-beam gradient force optical trap for dielectric particles, *Opt Lett. 11*, 288.

277. Yin, H., Wang, M. D., Svoboda, K., Landick, R., Block, S. M. & Gelles, J. (1995) Transcription against an applied force, *Science. 270*, 1653-7.

278. Arai, Y., Yasuda, R., Akashi, K., Harada, Y., Miyata, H., Kinosita, K., Jr. & Itoh, H. (1999) Tying a molecular knot with optical tweezers, *Nature. 399*, 446-8.

279. Mammen, M., Helmerson, K., Kishore, R., Choi, S. K., Phillips, W. D. & Whitesides, G. M. (1996) Optically controlled collisions of biological objects to evaluate potent polyvalent inhibitors of virus-cell adhesion, *Chem Biol. 3*, 757-63.

280. Stout, A. L. (2001) Detection and characterization of individual intermolecular bonds using optical tweezers, *Biophys J. 80*, 2976-86.

281. Ashkin, A. (1970) Acceleration and trapping of particles by radiation pressure, *Phys. Rev. Lett. 24*, 156–159.

282. Constable, A., Kim, J., Mervis, J., Zarinetchi, F. & Prentiss, M. (1993) Demonstration of a fiber-optical light-force trap, *Opt Lett. 18*, 1867-9.

283. Guck, J., Ananthakrishnan, R., Mahmood, H., Moon, T. J., Cunningham, C. C. & Kas, J. (2001) The optical stretcher: a novel laser tool to micromanipulate cells, *Biophys J. 81*, 767-84.

284. Guck, J., Ananthakrishnan, R., Moon, T. J., Cunningham, C. C. & Kas, J. (2000) Optical deformability of soft biological dielectrics, *Phys Rev Lett. 84*, 5451-4.

285. Jess, P. R. T., Garces-Chavez, V., Smith, D., Mazilu, M., Paterson, L., Riches, A., Herrington, C. S., Sibbett, W. & Dholakia, K. (2006) Dual beam fibre trap for Raman microspectroscopy of single cells., *Opt. Express. 14* 5779-5791.

286. Shinar, E., Rachmilewitz, E. A. & Lux, S. E. (1989) Differing erythrocyte membrane skeletal protein defects in alpha and beta thalassemia, *J Clin Invest. 83*, 404-10.

287. Boey, S. K., Boal, D. H. & Discher, D. E. (1998) Simulations of the erythrocyte cytoskeleton at large deformation. I. Microscopic models, *Biophys J. 75*, 1573-83.

288. Discher, D. E., Boal, D. H. & Boey, S. K. (1998) Simulations of the erythrocyte cytoskeleton at large deformation. II. Micropipette aspiration, *Biophys J. 75*, 1584-97.

289. Li, J., Dao, M., Lim, C. T. & Suresh, S. (2005) Spectrin-level modeling of the cytoskeleton and optical tweezers stretching of the erythrocyte, *Biophys J. 88*, 3707-19.

290. Lenormand, G., Henon, S., Richert, A., Simeon, J. & Gallet, F. (2001) Direct measurement of the area expansion and shear moduli of the human red blood cell membrane skeleton, *Biophys J. 81*, 43-56.

291. Henon, S., Lenormand, G., Richert, A. & Gallet, F. (1999) A new determination of the shear modulus of the human erythrocyte membrane using optical tweezers, *Biophys J. 76*, 1145-51.

292. Barton, J. P., Alexander, D. R. & Schaub, S. A. (1988) Internal and near-surphace electromagnetic fields for a spherical particle irradiated by a focused laser beam, *J. Appl. Phys. 64*, 1632–1639.

293. Ballas, S. K., Larner, J., Smith, E. D., Surrey, S., Schwartz, E. & Rappaport, E. F. (1987) The xerocytosis of Hb SC disease, *Blood. 69*, 124-30.

294. Chien, S., Usami, S. & Bertles, J. F. (1970) Abnormal rheology of oxygenated blood in sickle cell anemia, *J Clin Invest. 49*, 623-34.

295. Nash, G. B., Johnson, C. S. & Meiselman, H. J. (1988) Rheologic impairment of sickle RBCs induced by repetitive cycles of deoxygenation-reoxygenation, *Blood. 72*, 539-45.

296. Carvalho C., Chew E., Hashemy S., Lu J. & A., H. (2008) Inhibition of the Human Thioredoxin System *J. Biological Chemistry. 283*, 11913-11923.

297. Dong J., Wan Z.L., Chu Y.C., Nakagawa S.N., Katsoyannis P.G., Weiss M.A. & P.R., C. (2001) Isotope-edited Raman spectroscopy of proteins: a general strategy to probe individual peptide bonds with application to insulin, *J. Am. Chem. Soc. 123*.

298. Zheng R., Zheng X., J., D. & P., C. (2004) Proteins can convert to beta-sheet in single crystals, *Protein Science 13*, 1288-1294.

299. Zhu G., Zhu X., Fan Q. & X., W. (2011) Raman spectra of amino acids and their aqueous solutions, *ActabSpectrochimica part A. 78*, 1187-1195.

300. Jalilehvand, F., Leung, B. O., Izadifard, M. & Damian, E. (2006) Mercury(II) cysteine complexes in alkaline aqueous solution, *Inorg Chem. 45*, 66-73.

List of Publications

- Merlino, L. Vitagliano, **A. Balsamo**, F. P. Nicoletti, B. D. Howes, D. Giordano, D. Coppola, G. di Prisco, C. Verde, G. Smulevich, L. Mazzarella, A. Vergara

Crystallization, preliminary X-ray diffraction studies and Raman microscopy of the major haemoglobin from the sub-Antarctic fish *Eleginops maclovinus* in the carbomonoxy form
Acta Cryst. (2010). F66, 1536-1540.

Abstract

The blood of the sub-Antarctic fish Eleginops maclovinus (Em) contains three haemoglobins. The major haemoglobin (HbEm1) displays the Root effect, a drastic decrease in the oxygen affinity and a loss of cooperativity at acidic pH. The carbomonoxy form of HbEm1 has been crystallized in two different crystal forms, orthorhombic (Ortho) and hexagonal (Hexa), and high-resolution diffraction data have been collected for both forms (1.45 and 1.49 Å resolution, respectively). The high-frequency resonance Raman spectra collected from the two crystal forms using excitation at 514 nm were almost indistinguishable. Hb1Em is the first sub-Antarctic fish Hb to be crystallized and its structural characterization will shed light on the molecular mechanisms of cold adaptation and the role of the Root effect in fish haemoglobins.

- **A. Balsamo**, F. Sannino, A. Merlino, E. Parrilli, M. L. Tutino, L. Mazzarella, A. Vergara

Role of the tertiary and quaternary structure in the formation of bis-histidyl adducts in cold-adapted hemoglobins
Biochimie, Under review

Abstract

All tetrameric hemoglobins from Antarctic fish, included that of Trematomus bernacchii, HbTb, in its ferric state promptly, and distinctively from all the other tetrameric hemoglobins, form a mixture of aquo-met at the α subunits and bis-histidyl adduct (hemichrome) at the β subunits. The role of the tertiary and quaternary structure in the hemichrome formation in HbTb is unknown. Here we report the cloning, expression, purification, spectroscopic and computational characterization of the β-chain of HbTb (Tbβ). As the β-chain of human Hb (β_4-HbA), Tbβ self-assembles to form a β_4 homotetramer, but Tbβ forms quantitatively, and not partially as β_4-HbA, a reversible bis-histidyl adduct, both in the ferric and ferrous form. A molecular dynamics study on the isolated β-subunit of HbTb indicates that the ability to form hemichrome is an intrinsic feature of Tbβ chain, probably linked to the high intrinsic flexibility of the CD loop region. On the bases of these experimental and computational results, a discussion on the effect of quaternary structure on the stability of endogenous ferrous and ferric hexa-coordination is also presented.

- A. Merlino, M. Fuchs, **A. Balsamo**, A. Pica, G. Pompidor, C. Verde, F. Dworkowsky, L. Mazzarella, A. Vergara.

Raman evidence of a selective X-ray induced NO-photodissociation in tetrameric hemoglobin crystals
In preparation

Abstract

Despite the high physiological relevance, haemoglobin crystal structure with NO-bound is less than 1 % of the total liganded haemoglobins deposited in Protein Data Bank. The high reactivity with O_2 *via* oxidative denitrosilation is a major impediment. Here we report a second source of difficulty in

collecting crystallographic data of NO-bound hemoglobins. Indeed, X-ray induced photodissociation can be a significant phenomenon, even with conventional X-ray sources. Online Raman microscopy reveals why structures of the haemoglobin from *Trematomus bernacchii* determined *via* X-ray crystallography were always partially ligated (only at the α subunit, and never at the β subunit). Resonance Raman microscopy performed at the Swiss Light Source (PXII beamline) assisted in defining the lower X-ray dose feasible to collect a fully nitrosylated haemoglobin. These data give a physical explanation of the low content of nitrosyl haemoglobin structure available in literature.

- L. Mazzarella, **A. Balsamo**, A. Merlino, A. Vergara

Crystal structure of β_4 human hemoglobin in the ferric state
In preparation

- A.Merlino, **A. Balsamo**, F. Sica, C. Verde, L. Ronda, A. Mozzarelli, L. Mazzarella, A. Vergara

Experimental evidence of the role of tertiary structure in hemoglobin cooperativity
In preparation

Comunications at National and International Conferences
ùJuly 2009: XXIII Congresso Nazionale SCI - Divisione di Chimica Fisica– Sorrento (Italy), (poster).
Raman Imaging and Tweezers of ed blood cells from patients affected by anemia S, C and C+S
A. Balsamo, V. Pully, G. Rusciano, F. Sica, A. Merlino, M. Grosso, A. Sasso, L. Mazzarella, C. Otto, A. Vergara.

October 2010 : 8th RNase meeting – Napoli (Italy), (poster).
The swapping process in bovine pancreatic ribonuclease: substitution of Pro114A. **A. Balsamo**, A. Merlino, C. Ercole, D. Picone, L. Mazzarella, Filomena Sica.

November 2010: XV Giornate Scientifiche del Polo delle Scienze e delle Tecnologie per la vita. – Napoli, (Italy), (poster).
Combining X-ray crystallography / Raman spectroscopy: the NO binding to human and fish hemoglobins
A. Balsamo, A. Merlino, A. Pica, L. Mazzarella, A. Vergara.

November 2010: XV Giornate Scientifiche del Polo delle Scienze e delle Tecnologie per la vita. – Napoli, (Italy), (oral presentation).
Produzione e caratterizzazione di mutanti dell'emoglobina umana finalizzati allo studio dell'effetto Root.
A. Balsamo, F. Sannino, E. Parrilli, A. Vergara, L. Mazzarella, e M.L. Tutino.

September 2011 : XXIV-Congresso Nazionale SCI - Divisione di Chimica Fisica – Lecce, (Italy), (poster).
Bis-Histidyl coordination in tetrameric hemoglobins: Cold-adapted fish hemoglobins *versus* human hemoglobin
A. Balsamo, A. Merlino, M. L. Tutino, E. Parrilli, L. Mazzarella, A. Vergara.

September 2009 : XIII European Conference on the Spectroscopy of Biological Molecules – Palermo, (poster).
Raman-based diagnostic tools to distinguish anemia and to evaluate the expression ratio of S and C hemoglobins

A. Vergara, V. Pully, G. Rusciano, **A. Balsamo** F. Sica, A. Merlino, M. Grosso, A. Sasso, L. Mazzarella, C. Otto.

September 2009: 38° Congresso Nazionale dell'Associazione Italiana di Cristallografia – Salerno, (Italy) (poster).
Cross-talking of the chain termini in the swapping process of pancreatic ribonuclease
F. Sica, A. Merlino, **A. Balsamo**, C. Ercole, D. Picone, L. Mazzarella.

November 2009 : Bioinformatica e Biologia Computazionale in Campania BBC2009 –Avellino (Italy) (poster).
Relazione tra pH, struttura ed affinità per l'ossigeno nell'emoglobina con effetto Root da *Trematomus bernacchii*: un approccio combinato teorico-sperimentale
A.Merlino, A. Vergara, F. Sica, **A. Balsamo**, C. Verde, L. Boechi, M. A. Martì, D. Estrin, L. Ronda, A. Mozzarelli, L. Mazzarella.

Dicembre 2009 : Workshop "Thermodynamicaly Unstable Proteins: Chance or Necessity?" –Trieste, (Italy) (poster).
Partial unfolding, aggregation and swapping in pancreatic-like ribonucleases.
F. Sica, **A. Balsamo,** C. Ercole, D. Picone, E. Pizzo, G. D'Alessio, L. Mazzarella.

August 2010: XXII International Conference on Raman Spectrosopy - Boston, Massachusetts (poster).
Raman-assisted X-ray-Biocrystallography.
A. Vergara, A. Merlino, **A. Balsamo**, F. Sica, L. Mazzarella.

August 2010 : XVIth International Conference on Oxygen Binding and Sensing Protein – Anversa, (Belgium), (poster).
Root effect in crystals of *Trematomus bernacchii* hemoglobin (HbTb): a microspectrophotometric study.
L. Ronda, **A. Balsamo**, A. Vergara, A. Merlino, L. Mazzarella, A. Mozzarelli.

August 2010 : XVIth International Conference on Oxygen Binding and Sensing Protein – Anversa, (Belgium), (poster).
pH-induced tertiary conformational changes affect the oxygen affinity of the T state hemoglobin from the Antarctic fish *Trematomus bernacchii*
A.Merlino, A.Vergara, F. Sica, **A. Balsamo**, C. Verde, L. Boechi, M.A. Marti', D.A. Estrin, L. Ronda, A. Mozzarelli, L. Mazzarella.

August 2010: Gordon Research Conferences-Vibrational Spectroscopy – Boston, Massachusetts (poster).
Raman-assisted X-ray crystallography to study metal protein dynamics and reactivity"
A.Vergara, A. Merlino, **A. Balsamo**, F. Sica, L. Mazzarella.

August 2011: XXII Congress and general assembly, International Union of Crystallography (IUCr) – Madrid, (Spain) (poster)
Raman assisted X-ray crystallographic study of nitric oxide binding to deoxygenated hemoglobins
A. Pica, A. Merlino, **A. Balsamo**, L. Mazzarella, A. Vergara.

Awards
November 2009-Travel grants to Elettra synchrotron, Trieste (Italy).